Aero-Optical Assessments of Hypersonic Flowfields

by

Lauren E. H. Mackey

A dissertation submitted in partial fulfillment
of the requirements for the degree of
Doctor of Philosophy
(Aerospace Engineering)
in The University of Michigan
2019

Doctoral Committee:

Professor Iain D. Boyd, Chair
Professor Carlos E. S. Cesnik
Associate Professor Karthik Duraisamy
Associate Professor Eric Johnsen

"When I meet God, I am going to ask him two questions: Why relativity? And why turbulence? I really believe he will have an answer for the first."

-Werner Heisenburg

Lauren E. H. Mackey

lemackey@umich.edu

ORCID iD: 0000-0003-2643-2779

For Mom and Dad

ACKNOWLEDGEMENTS

This dissertation represents the work of many besides myself over the last several years. Without their constant support, encouragement, and guidance my graduate career would not have begun, let alone progressed to where it is today. If I were to simply list all who helped shape my career thus far, that list would certainly be longer than the rest of this dissertation.

I would first like to extend a thanks to my advisor Professor Iain Boyd, without whose constant guidance and support this work would not have been possible. Thank you for always providing the assistance needed, especially when things went very wrong or took decidedly longer than either of us would have imagined. I would also like to thank the members of my dissertation committee: Professor Carlos Cesnik, Professor Karthik Duraisamy, and Professor Eric Johnsen. I want to thank you for the time and energy you put into serving on my committee.

I would also like to extend a huge thank you to all the engineers and scientists I worked with at the Air Force Research Labs: Eswar Josyule, Nick Bisek, Ryan Gosse, Timothy Leger, and Konstantinos Vogiatzis. I am truly thankful to all of you for your diligent guidance. I would like to especially express my gratitude to Eswar Josyula for shaping my thesis through diligent mentorship.

To all the member of NGPDL, I am indebted to you, and thank you. Especially to Astrid Raisanen for letting me bounce so many ideas off of you over the last few years. Also, thanks for letting me complain when everything seemed to be going wrong, both with research and in life. I would also like to extend thanks to Peter

Cross for answering all (and there have been many) of the questions I have had over the years. And lastly, thank you to all my office mates for making the FXB feel a bit more like home.

Finally, I would to say how grateful I am to my family, especially, Mom and Dad. It looks like I will finally be graduating! Without your constant support and love I would not be here today. To my brother and his family, thanks for all of the support and minimal jokes about how I am approaching 30 and still in school. Last (and of course not least) I want to thank my husband, Luke. Thanks for keeping me sane when it seemed like going crazy was inevitable. Thanks, also, for proof-reading the rough draft of this work. That was not an easy task.

TABLE OF CONTENTS

LIST OF FIGURES

Figure

LIST OF TABLES

Table

LIST OF ABBREVIATIONS

$\mathbf{D_{sk}}$ Multicomponent Diffusion Coefficient
e Energy [J/kg]
h Enthalpy [J/kg]
k Thermal Conductivity [W/(m· k)]
$\mathbf{k_b}$ Backward Rate Coefficient
$\mathbf{K_{EQ}}$ Equilibrium Rate Coefficient
$\mathbf{k_f}$ Forward Rate Coefficient
$\mathbf{K_{GD}}$ Gladstone-Dale Constant [m^3/kg]
l Coordinate along Line of Sight [m]
Le Lewis Number
M Mach Number
n Index of Refraction
OPD Optical Path Difference [m]
OPL Optical Path Length [m]
P Pressure [Pa]
$\dot{\mathbf{q}}$ Flux Vector [W/m^2]
ρ Density [kg/m^3]
T Temperature [K]
t Time [s]
θ Characteristic Temperature [K]
τ Relaxation Time [s]
$\tilde{\tau}$ Shear Stress [Pa]
$\overline{\mathbf{u}}$ Diffusion Velocity [m/s]
u Velocity [m/s]
$\dot{\omega}$ Source Terms
X Molar Fraction
Y Mass Fraction
tke Turbulent Kinetic Energy
Sc Schmidt Number
Rs Strehl Ratio
λ Wavelength [m]
f Frequency [Hz]
κ Attenuation per unit length [dB/m]

Sub/Superscripts

c	Controlling
d	Dissociation
$*$	Equilibrium
∞	Freestream
$\langle\rangle$	Spatial Average
s	Species
$'$	Fluctuating
trans	Translational
t	Turbuelent
v	Vibrational
radio	radio
chem	Chemical
r	Rotational
critical	Pertaining to Critical Plasma Density

ABSTRACT

A potential future use of hypersonic platforms is for responsive Intelligence, Surveillance, and Reconnaissance (ISR). It is common for these types of missions to employ Electro-Optical/Infrared (EO/IR) sensors and Radio Frequency (RF) sensors to collect information. If an optical signal were to travel through a hypersonic flowfield, the type of high-speed flow analysis required to perform reliable assessments of sensor performance is unclear. In order to provide this information, the hypersonic flow phenomena of thermochemistry, high speed turbulence, and high enthalpy turbulence are studied.

In a hypersonic environment, the high kinetic energy of the oncoming flow causes the molecules in the flow to be thermally excited, leading to dissociation. In such a flowfield, an aero-optical analysis that considers thermochemical nonequilibrium is necessary to assist in sensor design. In the present thesis, we assess the optical properties of a nonequilibrium flowfield. The optical distortions are quantified using optical path length (OPL) and optical path difference (OPD). Optical distortion is also assessed based on flowfield modeling performed using a perfect gas assumption, and these distortions are provided for comparison. The primary contributions of nonequilibrium flow properties on optical distortion are identified. For all Mach numbers, OPLs are higher when the effects of dissociation and vibrational relaxation are included. Oxygen dissociation is the dominant nonequilibrium flow phenomenon affecting the optical distortion. As Mach number increases, atomic nitrogen begins

to have an additional influence on optical aberrations.

Additional distortion can arise in the hypersonic regime from high speed turbulence within the boundary layer. An initial study is conducted on a Mach 6 flow over a flat plate. This simulation is performed using air as a calorically perfect gas with varying levels of turbulence modeling and resolution. The cases are run using a laminar flow assumption (no turbulence), the Menter SST closure model for the Reynolds Averaged Navier-Stokes equations (RANS), and Implicit Large Eddy Simulation (ILES). It was found that the OPDs produced by the highest fidelity ILES approach can be as much as two orders of magnitude larger than solutions produced by the Menter SST model and laminar flow. While RANS was able to predict the mean flow quantities, it is unable to correctly predict the optical distortion.

The effects of thermochemical nonequilibrium on turbulent flow, and consequently optical distortion, are also presented in this dissertation. In the present study, numerical simulations are utilized to perform implicit large eddy simulations of flows over an adiabatic flat plate. The simulations are run with and without thermochemistry models to determine the effects of thermochemical nonequilibrium on optical distortion. Accounting for thermochemical nonequilibrium predicts less variation in OPD across the sensor aperture. The RMS average of OPD is significantly smaller for the real gas simulation when compared to a perfect gas. These differences in OPD occur because nonequilibrium energy exchanges act to damp out turbulent fluctuations, as illustrated with the Taylor-Green Vortex problem in this thesis. It is therefore necessary to include these physical flow effects in optical assessments to obtain an accurate description of the aero-optic distortions.

CHAPTER I

Introduction

1.1 Motivation

Throughout history, man has desired to fly further in less time. As such, much time and effort has been devoted to the pursuit of technological advances in the field of aeronautics. As technology advances, flight in the hypersonic regime is becoming more feasible. Missions for vehicles engaged in intelligence, surveillance, and reconnaissance (ISR) are well suited for hypersonic flight. Hypersonic ISR vehicles will be able to collect accurate and time relevant information to support missions globally. Figure 1.1 presents an image of a proposed hypersonic vehicle that is designed for ISR missions by the Boeing Corporation [11]. Sensors placed on vehicles like those in Fig. 1.1 are particularly susceptible to distortion, as the flow around such a body often reduces

Figure 1.1: Representation of typical hypersonic ISR vehicle [11]

the effective range of the sensor [58].

Numerous aspects of any flowfield can be a potential cause of signal distortion and aberration. This is especially true when examining hypersonic flow phenomena. One such type of distortion is radio frequency (RF) sensor degradation, often referred to as radio blackout. This phenomenon occurs when enough energy is imparted onto the air molecules that they not only dissociate, they begin to ionize. Radio waves can be reflected or diminished by the plasma layer [31]. Any signal with frequencies that fall below the characteristic plasma frequency will be attenuated [31]; as such, low frequency RF signals are the most vulnerable.

Radio blackout is a problem that has and continues to plague vehicles engaged in space travel. The Apollo missions experienced lost communications, for example [31]. Figure 1.2 presents a depiction of the Apollo re-entry trajectory. The altitudes at which the capsule experienced loss of communications are denoted in the figure. The altitude traversal where radio blackout was experienced corresponds to a time

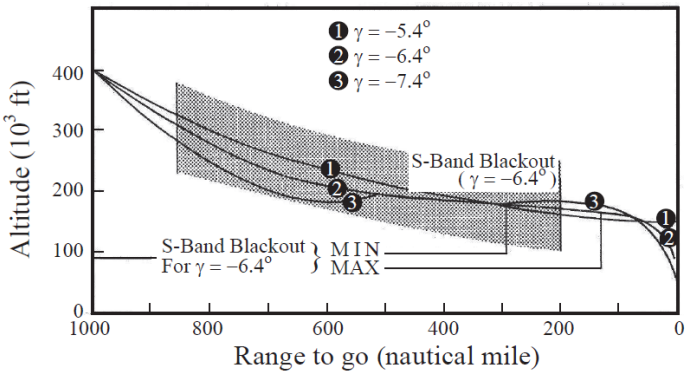

Figure 1.2: Apollo re-entry trajectory [31]

period of several minutes. Even modern re-entry vehicles can expect anywhere from 4 to 16 minutes of radio blackout [31]. While the ISR platforms are intended to fly intra-atmospheric missions, blackout may still be an issue since these vehicles will experience strong shock waves with elevated temperatures.

Another type of signal distortion that requires in-depth analysis is the distortion of an electo-optical or infrared (EO/IR) signal collected or sent from a hypersonic vehicle. Optical distortion caused by a flowfield is seen frequently in phenomena such as the twinkling of stars and is leveraged in the collections of Schlieren and shadowgraph images [57]. Distortion of an EO/IR beam arises as the beam travels through a field consisting of varying indices of refraction (which can be found from the density and mass fraction profiles using the Gladstone-Dale relation) [20]. Portions of an initially coherent wave front travel at different local speeds throughout such a field. A sensor used to detect through this field, therefore, will receive a signal that has various portions which have experienced phase shifts. An initially coherent structure will no longer be so. These aberration effects can be even larger in the presence of turbulent flow, as this type of flow is highly chaotic. Figure 1.3 presents a schematic of the optical distortion experienced from a sensor placed on a turret-like structure which is immersed in a turbulent flow.

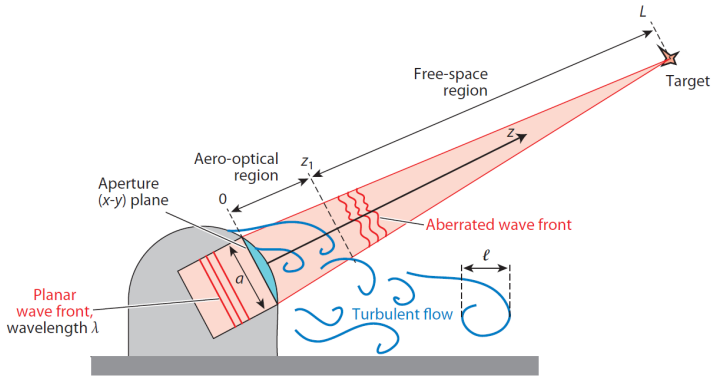

Figure 1.3: Schematic of Aero-optical distortion [57]

It should be noted that the EO/IR signal sent or received by a sensor located on the surface of a body will experience many effects apart from those imposed directly by the vehicle's interaction with the fluid around it. Figure 1.4 presents a description of various sources of possible signal distortion. Possible sources of distortion arise from the gas within the sensor, the sensor window which is often exposed to high

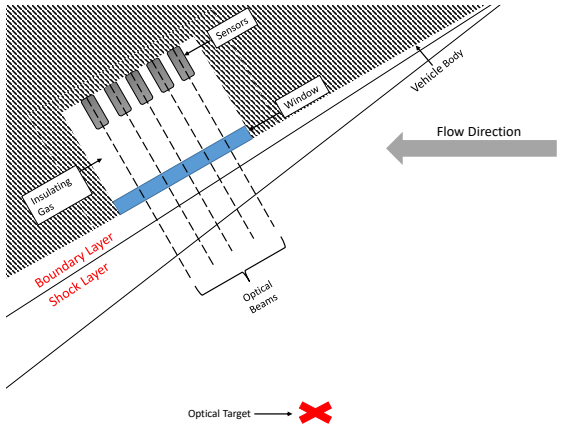

Figure 1.4: Schematic of possible sources of EO/IR signal distortion

temperatures, the boundary layer, the shock layer, and the atmosphere. The majority of the study presented in this dissertation focuses on the aero-optical effects, or the effects imposed on the signal from the boundary layer and the shock layer. The effects from the window and the atmosphere are neglected.

1.2 Review of Relevant Work

Many approaches have been taken to quantify sensor distortion, some of which are mentioned in Chapter III through Chapter VI. The study of aero-optics within the United States has gone through two stages of evolution, each of which coincided with developments in the field of laser technology [29]. The first period began in the 1970's and lasted until the 1980's. The second period began in the early 1990's and represents the era we are currently in [29]. The first era of study was primarily concerned with turrets and beam detectors as well as with atmospheric effects. As such, much study was dedicated to predicting the optical distortion produced in free shear flows. Many of the methods used to quantify optical distortion that are still used today were developed during this period. The Strehl ratio, or the ratio of the intensity of a distorted beam to an undistorted one, first made its appearance during the first period of aero-optical discovery [29].

The second period in which we are now in is marked by the advancement technology. For example, wave sensor technology has improved to a point at which taking detailed measurements in experimental settings is possible. Another important advancement in the second era can be found in the computational sciences. Solving higher fidelity flow models is now possible. The existing work still often details the optical distortion caused by turrets in sub- or supersonic flow [29]. Due to the flow scales in these test cases, the flow is treated as turbulent. Another set of current computational work focuses on relatively low speed, low enthalpy turbulent boundary layers created over flat or near-flat surfaces [57], [22], [23]. Only recently, as technology has advanced, has optical distortion analysis included resolved turbulence analysis. It is common in these studies to present the total distortion in terms of optical path difference, an approach which is adopted in the current study [57].

Much of the prevailing hypersonic work in the field of aero-optics is computational in nature, as it is expensive and very hard to replicate flight enthalpies. Often, the media surrounding a hypersonic vehicle is at a high temperature and cannot be accurately represented by a perfect gas. In fact in Ref. 1, it is illustrated that for any temperature exceeding 5000 K a single Gladstone-Dale constant, a proportionality constant used to find index of refraction, cannot describe the entire flow field. Atomic species will increase the Gladstone-Dale constant more than their molecular counterparts, as they have higher individual Gladstone-Dale constants [1]. While Ref. [30], does use density averaged Gladstone-Dale constants, the assessment is restricted to shock tunnel simulations. Algebraic relations to obtain OPDrms have been developed for this regime of flow, however, they are limited in application [63], [23]. For example, Ref. 58 is derived for an adiabatic wall assuming turbulence and small pressure fluctuations. Similar to these, many studies are concerned largely with turbulent fluctuations in the supersonic regime [22], [57]. The published data also does not provide any information regarding the sensitivity of optical quantities to

nonequilibrium flow phenomena. From the published data, the effects of including nonequilibrium in optical calculations is not immediately apparent.

Studies that investigate the interaction between turbulence and chemical reactions are scarce. The few studies that do exist have shown that turbulence may exert a significant effect on detailed chemical composition [36]. Furthermore, these studies show that exothermic reactions increase turbulent fluctuations and endothermic reactions dampen turbulent fluctuations. In the boundary layer, both types of reactions are possible, as species may dissociate and recombine. It should be noted that these past studies neglected thermal nonequilibrium. Even fewer studies have investigated a turbulent flow in thermochemical nonequilibrium to calculate optical properties. Most studies focus on low enthalpy perfect gas flows. The flow media surrounding a hypersonic vehicle cannot be accurately represented by a perfect gas. None of these simulations investigate the manner in which thermochemical nonequilibrium effects optical distortion in turbulent flows. Wyckham and Smits did present optical distortion over a flat plate for a turbulent flow with a high Mach number [63]. However, detailed descriptions of the role of thermochemical nonequilibrium in optical distortion is lacking in the published data and is a focus of the present thesis.

1.3 Background

Section 1.2 is presented in two subsections, each providing background information regarding flow phenomena that may have a significant effect on signal distortion.

1.3.1 Hypersonic Flight Conditions

The very definition of hypersonic flow is under much contention. Unlike sub- and supersonic flows, which are clearly delineated on the basis of Mach number, there are no clear Mach number divisions at which all flow above is hypersonic. As Professor P.L. Roe stated with regards to the definition of hypersonics, "it would be

quite possible for someone to advocate, and defend, numbers as small as three, or as high as 12. [2]" Instead, the definition of the hypersonic regime relies on the appearance of certain physical flow phenomena. These phenomena become progressively important as Mach number increases [3]. The flow phenomena that are of special importance in hypersonic flows are thin shock layers caused from increased density post-shock and the conservation of mass, strong entropy gradients within the boundary layer caused from the strong shock surrounding the vehicle body, and the strong viscous interactions (within the shock) that result in thick boundary layers with very high translational temperatures. These elevated temperatures can excite the internal modes of the molecules. Above 800 K, the vibrational mode of molecules becomes excited; beginning at 2000 K molecules in air begin to dissociate; starting at 9000 K the atoms in air can begin to ionize (Chemical dissociation and ionization are presented at equilibrium conditions) [4]. The excitation of the internal modes has ramifications on the bulk flow properties and, consequently, the optical distortion produced by the field.

Figure 1.5 presents the shock layer temperature for various re-entry velocities [2]. In the figure, the calorically perfect predicted shock temperature is also provided. The chemically reacting boundary layer has lower post-shock translational temperatures. This lowering of temperature is a consequence of energy leaving the translational mode and entering the excited internal modes. While Fig. 1.5 presents the effects of an equilibrium chemically reacting boundary layer, reaching equilibrium requires some amount of time. When the flow passes through high gradient regions, it takes a finite amount of collisions for the internal energies to adjust to a new thermodynamic state, often resulting in regions of nonequilibrium and relaxation [55]. Vibrational and chemical energy exchange processes are often relatively slow (compared to translational and rotational energy exchange processes), as seen in Eqn. (1.1) , to adjust

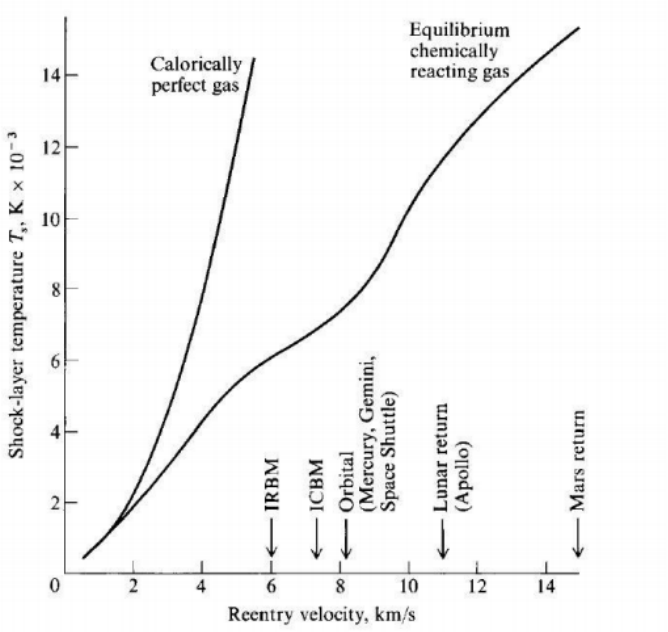

Figure 1.5: Comparison of temperature ratios between a calorically perfect gas and reacting flows [2]

to the rapidly changing flowfield, and thus nonequilibrium in these modes prevail.

$$\tau_{chem}, \tau_v >> \tau_{trans}, \tau_r \tag{1.1}$$

where τ is the characteristic time scales of the various flow phenomena.

In nonequilibrium regions, chemical dissociation often begins when the freestream Mach number of the vehicle exceeds 6. Dissociation occurs when the internal energy exceeds the dissociation energy of the molecule. Therefore, dissociation depends on the state of the internal energy modes and consequently the relaxation processes [26]. Through the gas transport processes, species can also diffuse, further altering the gas flow properties.

To accurately assess signal propagation through a hypersonic flowfield, high enthalpy flow physics need to be appropriately accounted for in optical distortion prediction. Specifically, high enthalpy effects in high gradient regions, such as strong shocks and boundary layers, need to be addressed in the optical assessments.

1.3.2 Turbulence

Because we are interested in examining the effect of hypersonic flow on optical distortion, it is pertinent to study turbulence in addition to high enthalpy thermodynamics. In particular, it is important to understand the manner in which energy is distributed and stored in turbulent flows, and how this can be affected by hypersonic flow phenomena. The turbulent energy can have an effect on optical analysis because turbulence is a chaotic flow phenomenon; it consists of vortical structures which promote fluctuations in flow parameters both spatially and temporally. These flows are often non-homogenous and anisotropic.

As an example of the complexity associated with turbulent flows, the precise definition of the turbulent structures, commonly referred to as eddies, has remained elusive to scientists [46]. Instead, eddies have come to be largely recognized as regions of turbulent motion which are relatively organized and have a consistent structure [46]. The eddies can range in size from the large scale eddies which have sizes dictated by the characteristic length associated with the general flow under consideration down to the smallest scales which can be dissipated by viscous effects. The larger eddies can occupy regions that are also populated by eddies of smaller sizes.

In 1920 Richardson proposed that the large eddies are inherently unstable [24]. As a consequence of this, the eddies break down into multiple smaller eddies (consistent with the stretching and conservation of angular momentum present in turbulent flows). This process will continue until the eddies become small enough for the viscous forces to have any influence over them. When the eddies reach the smallest "stable" scales, the viscous forces begin to dissipate the organized turbulent motions. Richardson hypothesized that the largest eddies are responsible for the energy production in turbulence, these eddies then break down and transfer energy through invisicid processes, due to the instability of their structures, to the smallest eddies which are dissipated by the viscosity.

Kolmogorov expanded upon (and quantified) these ideas; he developed what has come to be known as K-41 theory [46]. This theory is based on physical logic and has proven to be helpful in describing the general structure of turbulent flows [46]. Kolmogorov presented the idea that all geometric information of the large eddies is lost as the eddies break down in size, and, consequently, the smaller scales are statistically independent of the larger eddies. Therefore, the smaller scales are independent of the mean flow and the boundary conditions. He argued that the motions of these small scale eddies are universal to all turbulent flows. He further presented the idea that turbulent structures are dependent on only viscosity and dissipation rate (ν and ε, respectively) since they represent the two dominant processes that dictate energy transfer in turbulent flows. Kolmogorov further built upon this idea by supposing the intermediate scales have sufficiently high Reynolds numbers that the viscous effects are negligible on their energy transfer. This means that at sufficiently high Reynolds numbers, the intermediate scale are dependent on only ε. This correlates well with the hypothesis posed by Richardson, that energy is injected into turbulence at the large scales and cascades through intermediate structures until the structure is small enough for the viscous force to have a significant influence on them. Using dimensional analysis, energy in this range can be represented only by Eqn. (1.2).

$$E(k) = C_k \varepsilon^{\frac{2}{3}} k^{\frac{-5}{3}} \tag{1.2}$$

where C_k is referred to as the Kolomogorov constant and k is the wavenumber. The implications of K-41 theory are of importance. K-41 theory suggests that in all turbulent flows there is a universal range where energy decays at a rate of $k^{\frac{-5}{3}}$. Figure 1.6 presents the scaled energy spectrum for turbulent flows.

The purpose of discussing the turbulent energy cascade are two-fold. One reason to understand this cascade is to gain insight into turbulence modeling; see Chapter II

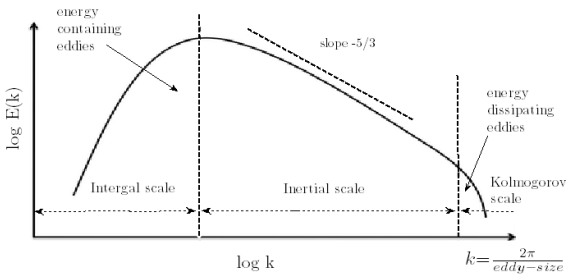

Figure 1.6: Turbulent energy spectrum [50]

for information regarding the specific models used in this study. Methods for performing turbulent calculations range from Reynolds-Averaged Navier-Stokes (RANS), in which all turbulent dynamics are modeled, to direct numerical simulations (DNS), in which all scales shown in Fig. 1.6 are resolved. Large eddy simulation (LES) lies in between these two methods in terms of resolution. Large eddy simulation resolves all large energy-containing eddies and all eddies in the universal inertial range; see Fig. 1.6. All small, dissipative scales are either modeled or numerically dissipated.

The other reason to study the turbulent cascade is to better understand energy exchanging mechanisms in turbulent flow and how they may be affected by thermochemical nonequilibrium. While studies that investigate turbulence and thermochemical nonequilibrium are not numerous, it is largely supposed that any mechanism which extracts energy out of the translational mode will dampen turbulent structures and turbulence in the inertial range may no longer be universal. Studying the turbulent energy transfer produced from simulations which utilize thermochemical nonequilibrium models can, therefore, provide insight into how these features affect turbulent flow and consequently optical distortion.

1.4 Scope of Present Work

The present work is divided into seven chapters. Chapter II presents the numerical analysis, both of the flowfield and of the optical distortion, employed in this study.

Chapter III presents a preliminary assessment of possible causes of signal distortion. Chapter IV illustrates the effects of modeling thermochemical nonequilbrium on signal distortion. Chapter V illustrates the effects of high velocity turbulence on signal aberration. Due to the importance of turbulence on optical distortion, it is pertinent to discuss the manner in which turbulent flow can be affected by thermochemical nonequilbrium. Chapter VI presents the effects of thermochemical nonequilibrium on turbulent flow. Chapter VII presents a summary discussing the ways in which hypersonic flow phenomena affect signal distortion.

CHAPTER II

Numerical Methods

2.1 Introduction

This chapter details the methods utilized in this study to simulate both the mean flow and optical solutions. This numerical analysis is presented in two sections, (1) nonequilibrium computational analysis of the flow field around the body of interest (including the nonequilibrium models used in this study), and (2) optical assessments using both real and perfect gas Gladstone-Dale proportionality constants.

2.2 Flowfield

The flowfield calculations are discussed in terms of (a) The Navier-Stokes equations with nonequilbrium models and (b) the modeling and resolution of turbulent structures.

2.2.1 Nonequilibrium Flow Field Calculation

The numerical calculations are conducted using computational fluid dynamic codes developed for high speed applications in which the Navier-Stokes equations are coupled with thermodynamic and transport property models. Unless otherwise noted, the information presented in this work pertains to all codes that are used.

The majority of this study is conducted using the research codes LeMANS (see Ref. [59] for validation and verification), US3D (see Refs. [40], [41] for validation and verification studies), and ANDEE (see Refs. [28], [27] for validation and verification studies). The computations are performed with the aid of finite rate chemistry and the Landau-Teller vibrational energy relaxation model. The mass-averaged velocity form of the governing equations for nonequilibrium flow are given in Eqns.(2.1) - (2.4) [27]. Unless otherwise noted, variables are as described in the list of abbreviations.

$$\frac{\partial}{\partial t}\rho_s + \nabla \cdot \rho_s(\mathbf{u} + \overline{\mathbf{u}}_\mathbf{s}) = \dot{\omega_s} \tag{2.1}$$

$$\frac{\partial}{\partial t}\rho\mathbf{u} + \nabla \cdot (\rho\mathbf{u}\mathbf{u} + \tilde{\tau}) = 0 \tag{2.2}$$

$$\frac{\partial}{\partial t}\rho_s e_{v,s} + \nabla \cdot (\rho_s e_{v,s} + \rho_s(\mathbf{u} + \overline{\mathbf{u}}_\mathbf{s}) + \dot{q}_{v,s}) = \dot{\omega}_{v,s}\rho_s + e_{v,s}\dot{\omega_s} \tag{2.3}$$

$$\frac{\partial}{\partial t}\rho e + \nabla \cdot (\rho(e + \frac{P}{\rho}\mathbf{u})) - \dot{q}_{trans} - \sum \dot{q}_{v,s} + \sum(\rho_s h_s \overline{\mathbf{u}}_\mathbf{s}) = \nabla \cdot (\mathbf{u}\tilde{\tau}) \tag{2.4}$$

Eqn. (2.1) is the species' mass conservation equation. In Eqn. (2.1), ρ_s is each species' density, and $\overline{\mathbf{u}}_\mathbf{s}$ is the diffusion velocity. The diffusion velocity is assumed to be generated by the species' concentration gradients according to Fick's first law of diffusion [6]:

$$\rho_s \overline{\mathbf{u}}_\mathbf{s} = -\rho D_{sk} \nabla \frac{\rho_s}{\rho} \tag{2.5}$$

where D_{sk} is the multicomponent diffusion coefficient and assumes a constant Lewis number of 1.4.

$$Le = \frac{\rho D_{sk} C_p}{k} \tag{2.6}$$

In Eqn.(2.1), the creation and destruction of each species, s, is represented by the source term $\dot{\omega}_s$. This source term used to describe chemical nonequilibrium (neglecting ionization) is found for each species utilizing the 17 reactions (see Eqns.(2.7)) that occur with the 5 primary species in dissociating air (N_2, O_2, NO, N, and O). In Eqns.(2.7), M represents all 5 collisional partners.

$$N_2 + M \leftrightarrow 2N + M \tag{2.7a}$$

$$O_2 + M \leftrightarrow 2O + M \tag{2.7b}$$

$$NO + M \leftrightarrow N + O + M \tag{2.7c}$$

$$NO + O \leftrightarrow O_2 + N \tag{2.7d}$$

$$N_2 + O \leftrightarrow NO + N \tag{2.7e}$$

The first three reactions $(a - c)$ in Eqns.(2.7) represent the dissociation and recombination of N_2, O_2, and NO, respectively. The last two reactions in Eqns.(2.7) are exchange reactions involving NO. In equilibrium, oxygen begins to dissociate at about 2000 K, followed by nitrogen at 4000 K. NO forms at approximately 2000 K through dissociated O colliding with the abundant N_2 molecules (via Eqn.(2.7e)) [2]. NO will begin to dissociate at higher energies than O_2 due to the strength of the bond that is formed between the nitrogen and oxygen atom[9]. The forward reaction rate and backward reaction rates are given in Eqns.(2.8) and (2.9), respectively. The

equilibrium constants and reaction rate coefficients are taken from Park [45].

$$k_f(T_c) = C_f T_c^{\eta} \exp(\frac{\theta_d}{T_c}) \tag{2.8}$$

$$k_b(T_c) = \frac{k_f}{K_{eq}} \tag{2.9}$$

where K_{eq} is derived from statistical mechanics and is referred to as the equilibrium rate coefficient and T_c is the rate controlling temperature; see Eqn.(2.10) [43].

$$T_c = \sqrt{(}TT_v) \tag{2.10}$$

where T is the translational temperature and T_v is the vibrational temperature. This model is referred to as Park‘s two temperature model [43]. It should be noted that in this study it is assumed that the flow is in rotational equilibrium. Equation (2.2) is the total momentum conservation equation. Equation (2.3) is the vibrational energy conservation equation which incorporates terms to describe vibrational energy conduction and diffusion. The source term for the conservation of vibrational energy equation is found using the Landau-Teller Relaxation model which describes vibrational translational energy coupling; see below [32].

$$\dot{\omega}_{v,s} = \rho_s \frac{e^*_{v,s} - e_{v,s}}{\tau_s} \tag{2.11}$$

where $\dot{\omega}_{v,s}$ is the energy exchange rate for the vibrational mode, $e^*_{v,s}$ is the equilibrium vibrational energy of species s at the local translational temperature, and $e_{v,s}$ is the vibrational energy of each molecular species. The relaxation time can be found using

Eqn.(2.12).

$$\tau_s = \frac{\sum_s X_s}{\sum_s X_s/\tau_{rs}} \tag{2.12}$$

where X_s is the mole fraction of the species s. The inter-species relaxation time,τ_{rs} , is found using the Millikan and White approximation; see Eqn.(2.13) [38].

$$p\tau_{rs} = (-18.42) + (1.16x10^{-3})\mu^{\frac{1}{2}}\theta_{v,s}^{\frac{4}{3}}(T^{-\frac{1}{3}} - 0.015\mu^{\frac{1}{4}}) \quad atm \cdot s \tag{2.13}$$

LeMANS, which is used for Chapter III, utilizes an additional correction factor in the Millikan and White approximation suggested by Park [43]. The vibrational temperature for each species is determined with a known vibrational energy and Eqn.(2.14) [55].

$$e_{v,s} = \frac{R\theta_{v,s}}{\exp(\theta_{v,s}/T_{v,s}) - 1} \tag{2.14}$$

where R is the species gas constant and $\theta_{v,s}$ is the characteristic temperature of vibration for each species, s. Equation (2.4) is the total energy conservation equation which includes additional terms that describe the species diffusion and translational heat conduction. Equations (2.1) - (2.4) are solved using the finite volume formulation. The viscosity for each species is found using Blottner curve fits [7], and the thermal conductivity for each species is found using Euckens relations [55]. Wilkie‘s semi-empirical mixing rule is used for the conductivity and the viscosity of a mixture [60].

It should be noted that Park‘s two temperature model was developed based on experimental investigations and may not accurately describe flow with rotational nonequilibrium and significant radiation that induces ionization [44]. The Landau-Teller model assumes only weak deviations from equilibrium. It also assumes the

molecules behave as a simple harmonic oscillator, and it only allows for single quantum jumps [55]. Millikan and White relaxation times were derived from empirical curve fits that do not accurately represent high temperature nonequilibrium physics [9]. The data for these curve fits are collected from shock tube experiments performed at temperatures ranging from 300 K to 8000 K [38]. Because of the narrow temperature range used to derive the fit, the curve fit only reports relaxation at certain vibrational levels. Still, these models are adequate for assessing a number of nonequilibrium phenomena and are widely used to describe nonequilibrium physics, thereby allowing a preliminary assessment of the effects of nonequilibrium on optical calculations.

2.2.2 Turbulence

Two classes of turbulent simulations are employed in this thesis. The Reynolds Averaged Navier Stokes equations are solved, and large eddy simulations are performed.

2.2.2.1 Reynolds Averaged Navier Stokes Equations

One of the most prevalently used methods utilized to assess turbulent flows involves decomposing the velocity into a mean and a fluctuating component. This sum of the two components is then inserted into the Navier-Stokes equations and the averages of the equations are taken. The resulting set of equations is called the Reynolds Averaged Navier Stokes equations (RANS); see appendix A for full description of these equations [21].

In the RANS equations there are more unknowns than there are equations, as such these equations cannot be directly solved. The inability of RANS to be solved by themselves is commonly referred to as the *closure problem* and arises from the existence of an additional stress referred to as the Reynolds stress. One method that is used to "close" these equations finds its basis in the Boussinesq equation; see

Eqn.(2.15) [24].

$$-\rho(\overline{u_i' u_j'}) = \mu_t(\frac{\partial u_i}{\partial x_j} + \frac{\partial u_j}{\partial x_i} - \frac{2}{3}\frac{\partial u_k}{\partial x_k}\delta_{ij}) - \frac{2}{3}\rho k \delta_{ij} \tag{2.15}$$

This model assumes that the Reynolds stress can be modeled in an analogous manner to the laminar stress. It should be noted that in Eqn.(2.15), $\delta_{ij}$is the kronecker delta function and k is the turbulent kinetic energy.

With the aid of Eqn.(2.15) the RANS equations largely take the form of the laminar Navier-Stokes equations with the conserved variables describing the mean flow field. Notable differences in the equation sets (RANS and Navier-Stokes) can be found in the modification of the stress term in the conservation of momentum equation [21].

$$\frac{\partial}{\partial x_j}(t_{ij} + \tau_{ij}) \tag{2.16}$$

where τ_{ij} is the turbulent stress and is of the form suggested by Boussinesq; see Eqn.(2.15).

The energy equation is modified by the addition of the term shown in Eqn.(2.17) which represents the effect of turbulent shear stress on the system's energy.

$$\frac{\partial}{\partial x_j}(u_i(t_{ij} + \tau_{ij})) \tag{2.17}$$

It should be further noted that the diffusion coefficient and thermal conductivity are also modified to include the effects of turbulence in the flow. The total diffusion coefficient and thermal conductivity are now composed of the sum of their respective laminar and turbulent components. The turbulent translational and vibrational

thermal conductivities are presented in Eqns.(2.18) and (2.19) [21].

$$k_{turb} = \frac{k_{lam}}{k_{lam} + k_{v,lam}} \frac{\mu_t}{c_p Pr_t} \tag{2.18}$$

$$k_{v,turb} = \frac{k_v}{k + k_v} \frac{\mu_t}{c_p Pr_t} \tag{2.19}$$

where Pr_t is the turbulent Prandtl number and is taken to be 0.9, as suggested by Allmaras [52]. The turbulent contribution to diffusion is shown in Eqn.(2.20).

$$D_t = \frac{\mu_t}{\rho Sc_t} \tag{2.20}$$

where Sc_t is the turbulent Schmidt number and is assumed to be constant and μ_t is the eddy viscosity. The eddy viscosity is as of yet unknown. A further model must be used to find this effective turbulent viscosity. One such model, based largely on empiricism and dimensional arguments, is the Spalart-Allmaras model (S-A model) [52].

The S-A model consists of one equation that describes the transport of a modified turbulent (eddy) viscosity. At its inception, it was assumed that an incompressible eddy viscosity model would be sufficient in the compressible regime. This was proved to be incorrect. The S-A model was thus improved as shown in Eqn.(2.21) [13].

$$\begin{aligned} \frac{\partial \rho\widetilde{\nu}}{\partial t} + u_j \frac{\partial \rho\widetilde{\nu}}{\partial x_j} = c_{b1}(1 - f_{t2})\widetilde{S}\rho\widetilde{\nu} - \left[c_{w1} f_w - \frac{c_{b1}}{\kappa^2} f_{t2}\right] \rho \left(\frac{\widetilde{\nu}}{d}\right)^2 + \\ \frac{1}{\sigma}\left[\frac{\partial}{\partial x_j}((\mu + \rho\widetilde{\nu})\frac{\partial \widetilde{\nu}}{\partial x_j}) + c_{b2}\rho \frac{\partial \widetilde{\nu}}{\partial x_i}\frac{\partial \widetilde{\nu}}{\partial x_i}\right] \end{aligned} \tag{2.21}$$

In Eqn.(2.21), $\widetilde{S}$ is the modified vorticity; see Eqn.(2.22).

$$\widetilde{S} \equiv S + \frac{\widetilde{\nu}}{\kappa^2 d^2} f_{v2} \tag{2.22}$$

where d is the distance to the closest wall, S is the magnitude of vorticity, and f_{v2} is found using Eqn.(2.23).

$$f_{v2} = 1 - \frac{\chi}{1 + \chi f_{v1}} \tag{2.23}$$

In the S-A model, f_w is found using Eqn.(2.24).

$$f_w = g\left[\frac{1 + c_{w3}^6}{g^6 + c_{w3}^6}\right]^{\frac{1}{6}} \tag{2.24}$$

where g is found using Eqn.(2.25) and Eqn.(2.26).

$$g = r + c_{w2}(r^6 - r) \tag{2.25}$$

$$r = min(\frac{\tilde{\nu}}{\widetilde{S}\kappa^2 d^2}, 10) \tag{2.26}$$

The term f_{t2} is described in Eqn.(2.27).

$$f_{t2} = c_{t3} exp(-c_{t4}\chi^2) \tag{2.27}$$

All remaining constants are described in Table 2.1 [52].

Table 2.1: S-A Constants

Constants	Value
c_{b1}	0.1355
σ	2/3
c_{b2}	0.622
κ	0.41
c_{w1}	$c_{b1}/\kappa^2 + (1 + c_{b2})/\sigma$
c_{w2}	0.3
c_{w3}	2
c_{v1}	7.1
c_{t3}	1.2
c_{t4}	0.5

The S-A model, as shown in Eqn.(2.21), can allow negative eddy viscosity which presents a non-physical solution. This anomaly is caused from grids that do not properly resolve the flow and non-physical variations in time that can arise from discretization schemes. In order to avoid negative eddy viscosity, the modified vorticity as described in Eqn.(2.22), is altered. The improved vorticity model is shown in Eqn.(2.28).

$$\widetilde{S} = \begin{cases} S + \bar{S} & \bar{S} \geq -c_{v2}S \\ S + \frac{S(c_{v2}^2 S + c_{v3}\bar{S})}{(c_{v3}-2c_{v2})S - \bar{S}} & \bar{S} < -c_{v2}S \end{cases} \tag{2.28}$$

where

$$\bar{S} = \frac{\widetilde{\nu}}{\kappa^2 d^2} f_{v2} \tag{2.29}$$

and S is the magnitude of vorticity. The variables found in Eqns.(2.29) and (2.28) are as described above with the addition of c_{v2} which equals 0.7 and c_{v3} which equals 0.9.

Another modification is implemented to avoid further undershooting. This modification consists of utilizing a different conservation equation if the eddy viscosity is less than zero. The negative model takes the form of Eqn.(2.30) [52].

$$\frac{\partial \rho\widetilde{\nu}}{\partial t} + u_j \frac{\partial \rho\widetilde{\nu}}{\partial x_j} = c_{b1}(1 - c_{t3})\widetilde{S}\rho\widetilde{\nu} - c_{w1}\rho\left(\frac{\widetilde{\nu}}{d}\right)^2 + \frac{1}{\sigma}\left[\frac{\partial}{\partial x_j}((\mu + f_n\rho\widetilde{\nu})\frac{\partial \widetilde{\nu}}{\partial x_j}) + c_{b2}\rho\frac{\partial \widetilde{\nu}}{\partial x_i}\frac{\partial \widetilde{\nu}}{\partial x_i}\right] \tag{2.30}$$

When compared with Eqn.(2.21), Eqn.(2.30) is found to be similar with changes to few terms. The function f_n is introduced and found using Eqn.(2.31).

$$f_n = \frac{c_{n1} + \chi^3}{c_{n1} - \chi^3} \tag{2.31}$$

where c_{n1}=16 and χ is as described above.

Using Eqns.(2.30) and (2.21), the eddy viscosity can be found directly using Eqn.(2.32).

$$\mu_t = \rho\widetilde{\nu} f_{v1} \tag{2.32}$$

where f_{v1} is found using Eqn.(2.33).

$$f_{v1} = \frac{\chi^3}{\chi^3 + c_{v1}^3} \tag{2.33}$$

and c_{v1} is equal to 7.1. χ is described in Eqn.(2.34).

$$\chi = \frac{\widetilde{\nu}}{\nu} \tag{2.34}$$

In order to be numerically evaluated, the S-A convective fluxes (see Eqn.(2.35)) are discretized and shown in Eqns.(2.36). The fluxes are discretized using integration over a surface and an upstream method in which the variables from the direction upstream in the flow are used and those downstream are neglected.

$$\nabla \cdot (\rho\vec{u}\widetilde{\nu}) \tag{2.35}$$

$$\sum 0.5 * (u_{left} + u_{right})\rho\widetilde{\nu}_{upstream} ds \tag{2.36}$$

where u_{left} and u_{right} denote the values of u in each respective cell and ds denotes the area of the face.

The diffusive fluxes (see Eqn.(2.37)) are also discretized utilizing integration over

a surface as shown in Eqn.(2.38).

$$\frac{1}{\sigma}((\mu + \rho\widetilde{\nu})\nabla\widetilde{\nu}) \tag{2.37}$$

$$\frac{1}{\sigma}\sum(\mu + \bar{\rho}\widetilde{\nu})(\nabla\widetilde{\nu} \cdot n)ds \tag{2.38}$$

The final term in the S-A model that is discretized is the cross diffusion term; see Eqn.(2.39).

$$\frac{c_{b2}}{\sigma}\rho\nabla^2\widetilde{\nu} \tag{2.39}$$

The cross diffusion term was discretized using the divergence theorem and values of eddy viscosity from the right and left cells of each face. The fullly discretized term is illustrated in Eqn.(2.40).

$$\frac{c_{b2}}{\sigma}\sum(\widetilde{\nu}_{left} + \widetilde{\nu}_{right})^2\rho * V \tag{2.40}$$

The dependence on volume in the previously shown term evolves from integrating over a control volume.

The source terms are algebraic in nature and require no extra treatment from their original form (in Eqn.(2.21)) except for integration over a control volume.

Once the terms are discretized in space, an implicit time-marching scheme is constructed for the model. For demonstration of this application the S-A model is presented in a compact form; see Eqn.(2.41).

$$V\frac{\partial\rho\widetilde{\nu}}{\partial t} = -R \tag{2.41}$$

where R is all terms in Eqn.(2.21) with the exception of the time derivative. R is

commonly referred to as the residual. V, which denotes cell volume, appears through the discretization process when terms are integrated over a control volume. The implicit time marching method is applied as in Eqn.(2.42).

$$\frac{V}{\triangle t}\rho(\widetilde{\nu}_{n+1} - \widetilde{\nu}_n) = -R(\tilde{\nu}_{n+1}) \tag{2.42}$$

The right side of Eqn.(2.42) is then expanded using a Taylor series. Higher order terms are neglected, and Eqn.(2.43) is obtained.

$$R(\widetilde{\nu}_{n+1}) = R(\widetilde{\nu}_n) + \frac{\partial R}{\partial \widetilde{\nu}}\triangle\widetilde{\nu} \tag{2.43}$$

Equation 2.42 can then further be simplified to Eqn.(2.44).

$$(\frac{V}{\triangle t}\rho + \frac{\partial R}{\partial \widetilde{\nu}})\triangle\widetilde{\nu} = -R(\widetilde{\nu}_n) \tag{2.44}$$

Equation (2.44) provides a method to find the updated viscosity (from $\triangle\widetilde{\nu}$) with the described spatial discretization. A previously undiscussed term appears in Eqn.(2.44), $\frac{\partial R}{\partial \widetilde{\nu}}$, which is called the Jacobian.

The Jacobians for the source terms depend on taking the derivative of each function with respect to the conserved variable. In practical applications, the cross diffusion contribution to the Jacobian are neglected due to stability issues that can occur. The Jacobians for the convective and diffusive fluxes are differential in nature and found as in Refs. [14].

2.2.2.2 Large Eddy Simulation

While RANS is able to capture mean flow behavior with some reliability, it uses simplistic approximations to assess flow features and is unable to provide resolved turbulent information. Due to the lack of detail provided by RANS simulations, it is

necessary to utilize the more computationally expensive large eddy simulation (LES). LES utilizes the Navier-Stokes equations applied to a filtered flowfield to solve for a system on a mesh with enough resolution to resolve the large-scale turbulent structures. The small scale turbulence is either modeled or dissipated by the grid spacing. Due to the computational expense related to this method of solution, relatively simplistic flows are evaluated.

The flat plate large eddy simulations in this thesis are conducted using the finite volume US3D code, a computational fluid dynamics code for high speed flows that was developed at the University of Minnesota. In US3D, the viscous terms are calculated using a 2nd-order central scheme. The inviscid terms are calculated using a 6th-order central scheme. The time integration is performed using a 2nd-order implicit method. The high order terms are used to help reduce the number of grid points required in the computational domain to resolve the turbulence [53].

The Taylor-Green vortex problem in this study is run with Hypercode. It is a finite volume code intended for use on high speed flow applications. Hypercode uses a 2nd-order central scheme for the viscous fluxes and 5th-order weighted essentially non-oscillatory (WENO) stencil (with AUSM flux splitting) for the inviscid fluxes. Hypercode uses a second order explicit time-marching scheme.

The large eddy simulations are conducted using an implicit filter. An implicit LES method does not resolve all turbulent flow features. Instead, the grid behaves as a filter. All features that are not resolved by the grid will be numerically dissipated [19]. This level of resolution is acceptable for an optical study because the most optically important features are approximately the size of the boundary layer [58].

2.3 Optical Analysis

The optical analysis is performed on a steady-state flow field. To conduct optical assessments of an initially planar wave front, the index of refraction of the fluid

mixture surrounding the vehicle is needed. The index of refraction can be found from simplifying Lorentz radiation interaction theory with the model of an induced harmonic oscillator [51]. The resulting simplification for transparent media is the Gladstone-Dale relation; see Eqn.(2.45) [61]:

$$n = K_{GD}\rho + 1 \tag{2.45}$$

where n is the index of refraction, ρ is the gas mixture density and K_{GD} is the Gladstone-Dale constant. The Gladstone-Dale relation is built upon Lorentz radiation interaction theory. The Gladstone-Dale constant in Eqn. (2.45) can be assumed to be a constant for the entire flowfield as for (perfect gas) air. However, this study also uses a Gladstone-Dale constant that is variable over the flowfield and accounts for real gas effects, Eqn.(2.46) [37].

$$K_{GD} = \sum K_s \frac{\rho_s}{\rho} \tag{2.46}$$

where K_s is the Gladstone-Dale constant for each species, ρ_s is the density of each species, and ρ is the total mixture density. The experimentally obtained Gladstone-Dale constants for each species are listed in Table 2.2 [1, 4, 30]. These constants

Table 2.2: Species' Gladstone-Dale Constants

Species	Gladstone-Dale Constant, m^3/kg
N_2	$2.40x10^{-4}$
O_2	$1.93x10^{-4}$
NO	$2.21x10^{-4}$
N	$3.10x10^{-4}$
O	$3.04x10^{-4}$

are applicable for sensor sources at wavelengths equivalent to approximately $0.5\mu m$ [1, 4, 30].

From Ref. [1], it was determined that in the majority of the temperature regimes

in which the experiments (where temperatures do not exceed 9000 K) were performed the Gladstone-Dale constants were independent of temperature. It has been further suggested that since the Gladstone-Dale constant is a function of polarizability for particles, that for non-polar molecules (N_2, O_2) whose polarizability is independent of temperature, the applicability of the calculated Gladstone-Dale constant extends beyond the range of experimentation [4]. NO, however, is a polar molecule and therefore its polarizability does depend on its thermal state. However, it was experimentally determined that the Gladstone-Dale constant for NO remained approximately constant up to a Mach number of 22 [1]. Existing computations have used the Gladstone-Dale constant in Table 2.2 for NO for temperatures exceeding 9000 K [30].

Many of the trends observed in Table 2.2 may be explained by polarizability. The polarizability of an atom or molecule describes how it reacts to an outside force; specifically, how the electron cloud is supplanted due to the outside force. The Gladstone-Dale constant is proportional to the product of the polarizability and the inverse of the molecular weight [4]. Generally, polarizability increases with atomic radius, as electrons are less tightly held by the nucleus. Atomic nitrogen has a larger radius and lower molecular weight than atomic oxygen resulting in a higher Gladstone-Dale constant. The same polarizability trends with regards to size generally apply to molecules and explain the differences in Gladstone-Dale constants between molecular nitrogen and oxygen. While the molecular species may be more polarizable (due to their larger size), the increase in polarizability does not offset their increase in molecular weight. This results in molecular Gladstone-Dale constants that are lower than their atomic counterparts.

While some characteristic trends are general and apply to almost all molecules or atoms, some characteristics are specific to a molecule or atom. For example, there is a larger difference in Gladstone-Dale constant between N_2 and N than O_2 and O. To explain the larger difference between the N_2 and N constants, the way O_2 forms

needs to be examined. According to the Heitler-London rule, a description of chemical bonding based on quantum mechanics, it can be expected that O atoms would bond with 10 bonding electrons and only 2 anti-bonding pairs. However, this is not what is seen in real systems. O_2 forms with 8 bonding pairs and 4 anti-bonding pairs. The extra non-bonding pairs make O_2 more polarizable, and thus it has a Gladstone-Dale constant closer to O (than N_2 will have relative to N) since N_2 does not have an extra pair non-bonding electrons [1].

Once the Gladstone-Dale constant is calculated (Eqn.(2.46)) and the index of refraction is known (Eqn.(2.45)), it is possible to find the optical path length (OPL). Optical path length is the distance light would travel in a vacuum to arrive in phase with light traveling through the actual medium. For a non-varying field, this reduces to the product of the index of refraction and the geometric distance the light travels; however, the indices of refraction in this study are varying and therefore must be integrated along each ray of an optical beam; see Eqn. (2.47) [56]:

$$OPL = \int ndl \tag{2.47}$$

where n is the index of refraction and dl is the geometric length over which the integration is performed. Each ray of the beam is assumed to be a straight line. In this study, refraction is neglected. It should be noted that for this study n-1 is the quantity that is integrated. Often of more interest in considering optical aberrations, is the difference between optical path length of a ray and a reference value, usually taken to be the spatially averaged OPL (of all rays) across the sensor aperture; it is a measure of each ray's phase shift from the mean. This difference is referred to as optical path difference (OPD) and is found using Eqn.(2.48) [57].

$$OPD = OPL - \langle OPL \rangle \tag{2.48}$$

In the derivation of the Gladstone-Dale relation, it was assumed that the medium through which the light travels is transparent and that absorption can be neglected [51]. The beam's absorption of radiation emitted by a high energy gas, however, may be important. The current analysis also neglects the molecules in high vibrational states that could potentially have differing polarizabilities [1] and thus different Gladstone-Dale constants. Another feature that is not considered in this study is chemistry involving the vehicle's surface or sensor window.

CHAPTER III

Preliminary Analysis Of Optical Beam Propagation

3.1 Introduction

While the majority of the work presented in this dissertation focuses on detailed, high fidelity studies of optical distortion, Chapter III presents a preliminary analysis of signal propagation using simple correlations and models. This is done to identify the areas of signal distortion analysis that are lacking. This study will also provide information to help determine which causes of signal distortion are likely to be present in hypersonic flows of interest for ISR missions. In this study, numerical simulations are utilized to examine the effects of hypersonic flow on sensor signal degradation. The simulations are performed on a flow at Mach 7 and an altitude of 30 km over an axisymmetric cone. The simulated flows are assumed to be fully turbulent and are run with multi-equation closures to the RANS equations.

Chapter III first presents a preliminary analysis of optical and infrared distortions (EO/IR). These may be the most difficult to quantify computationally. EO/IR signals can become aberrated as the waves traverse a field that has changing density. As the wave fronts travel through the changing density field, portions can travel at different speeds, thus distorting the signal. Turbulent fluctuations can create even greater

density variations, leading to increased distortion of the signal.

Chapter III not only presents simple models for EO/IR distortion, it also presents the potential signal attenuation caused from plasma formation. The strong shock waves that surround hypersonic vehicles can promote the formation of plasma sheathes. The high incoming kinetic energy of the freestream fluid is partially transferred into the internal modes of the molecules as the fluid passes through the shock wave. This energy transfer promotes dissociation and, if enough energy is imparted into the internal modes of the fluid, ionization. These plasma sheathes can absorb and scatter radio frequency (RF) signals, potentially making them unusable for information exchange. Including the real gas effects is integral to calculating radio frequency sensor degradation; radio blackout can only be accounted for when ionization is considered. Radio blackout occurs when sufficient energy is imparted onto the molecules surrounding the vehicle that they ionize. Radio waves can be reflected or diminished as they travel through this plasma field [31]. In fact, any signal will be attenuated for frequencies that fall below the plasma frequency [31]. Low frequency RF waves are the most vulnerable. Radio blackout is a problem that has plagued many vehicles associated with space travel. The Apollo missions experienced many minutes of lost communications, for example [31]. Radio blackout has continued to be an issue even for the more modern Space Shuttle missions [31]. While the ISR platforms are intended to fly intra-atmospheric missions, blackout may still be an issue, as these vehicles will experience strong shocks.

A significant effect on sensors can also come from the surface temperature of the vehicle. If the temperature exceeds material specific thresholds, the portion of the sensor exposed to flow could suffer damage and/or performance loss. At hypersonic Mach numbers, vehicle surface temperatures become elevated. The elevated temperatures arise from the viscous interaction of the fluid with the vehicle. High Mach flow also carries large amounts of kinetic energy. The flow must be slowed to zero

velocity at the wall which creates a large transfer of energy. This transfer of energy often manifests as an increase in the temperature of the fluid surrounding the vehicle and, consequently, as an increase in surface temperature of the vehicle. The flow considered in this study is also turbulent. Turbulent mixing promotes the transfer of both momentum and energy which can further increase surface temperature.

Chapter III first presents the methods used only in this portion of the dissertation. It should be noted that the remainder of the dissertation uses the methods outlined in Chapter II; however, due to the preliminary nature of this study, a differing set of methods is applied. Chapter III will then present the conditions of the numerical simulations. Next, the results will be discussed. Chapter III concludes with a summary of the pertinent knowledge gained from this analysis.

3.2 Methods of Analysis

This study employs the University of Michigan's hypersonic computational fluid dynamics (CFD) code LeMANS. LeMANS is a CFD solver that simulates continuum flows that are in thermochemical nonequilibrium [35]. These types of flows, often experienced during hypersonic flight, have air molecules (O_2 and N_2) that are excited due to the presence of extreme physical conditions. LeMANS couples the Navier-Stokes equations with thermodynamic and transport property models [35]. The code utilizes finite rate chemistry and energy relaxation models to describe the nonequilibrium aspects of the flow [35]. LeMANS uses a finite volume formulation and is second order accurate [35].

In order to examine the turbulent boundary layers critical to the present study, three turbulence models are added to LeMANS: Menter BSL [18], Menter SST [18], and Spalart-Allmaras [52]. The original code is modified to solve the RANS equations; see Chapter II. For the cases that are of interest in this study, the flow is assumed to be completely turbulent. Once the flow data is calculated, various parameters along

linear paths (representing lines-of-sight) and along the vehicle surface are evaluated to assess how a sensor's performance could be affected.

3.2.1 EO/IR Interference

Two different methods are applied to discern the effects of a hypersonic flowfield on electro-optical signal aberration. Method I is discussed in section 3.2.1.1 and is adapted from free shear flow theory. Method II is discussed in section 3.2.1.2 and is derived to correspond with experiments conducted on a turbulent flow over a flat plate.

3.2.1.1 Method I

Many ISR vehicles use EO/IR sensors that collect electro-magnetic signals. EO/IR signals can experience degradation due to the boundary layer surrounding the vehicle [8]. This degradation can be characterized by the Strehl ratio which describes the ratio of the focused intensity of the disturbed beam to the focused intensity of a "perfect," undisturbed beam. An undistorted beam would have a Strehl ratio equal to one. The Strehl (Rs) ratio is calculated using Eqn. (3.1).

$$Rs = \exp -\langle \Psi^2 \rangle \tag{3.1}$$

where Ψ is the phase error. The phase error can be calculated using Eqn. (3.2) [5]. It should be noted that this model was developed to analyze turbulent disruptions to the signal in free shear flows. However, it is assumed here that it can provide general trends when care is taken to ensure that the physics of the boundary layer are retained.

$$\langle \Psi^2 \rangle = 2k^2 \frac{b^3}{a} L^3 \int \frac{dn}{dy}^2 dy \tag{3.2}$$

In Eqn. (3.2), k is the wave number, b^3/a is an experimentally determined value of 0.0057, n is the index of refraction, and L is the lateral distance between the 5% and 95% value of the time-averaged index of refraction profiles [33]. Because this model is designed to work for free shear flows and not for features such as shocks, only the profile of n near the wall is used.

In order to obtain Rs, one needs to know the spatial profile of the index of refraction. The index of refraction can be found using Eqn. (3.3).

$$n = 1 + K_{GD}\frac{\rho(y)}{\rho_{ref}} \tag{3.3}$$

where K_{GD} is a mass averaged Gladstone-Dale constant, ρ is the mass density, and ρ_{ref} is the reference mass density at 1 Atm and 273 K. It should be noted that for the cases used in this study, the chemistry did not play an important part in the overall flow; the mass fraction of the reactants never exceeds 10^{-6}. Because of the relatively low effect of chemical reactions in this flow, the index of refraction of perfect air, as provided by Ref. [33], is used. The index of refraction is provided for a temperature of 15°C and a pressure of 1 Atm. Figure 3.1 presents the index of refraction for air over the wavelengths of interest. A correction derived from experimentation is provided for perfect gas air in Ref. [33] to account for variations in temperature and pressure; see Eqn. (3.4).

$$\sigma_c = p\frac{[1 + p(60.1 - 0.972T)10^{-10}]}{96095.43(1 + 0.0003661T)} \tag{3.4}$$

where σ_c is the correction multiplier, p is the pressure in Pascals and T is the temperature in degrees Celsius. The temperature and pressure profiles are provided by LeMANS. The correction profile is multiplied by the index of refraction to obtain an index of refraction profile. The gradient of the index of refraction is then integrated to find the Strehl ratio; again, see Eqn. (3.2).

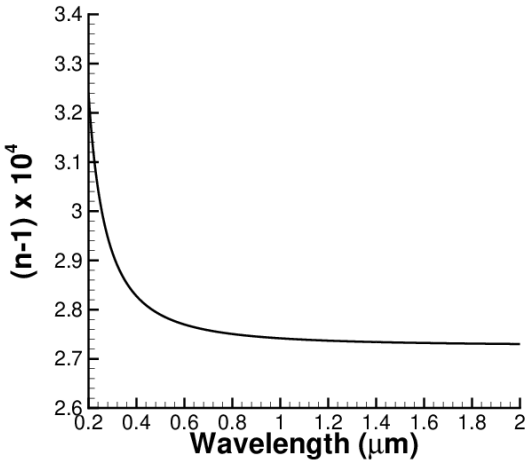

Figure 3.1: Index of Refraction for perfect gas air as a function of signal wavelength

3.2.1.2 Method II

The method described above does not take turbulent fluctuations directly into consideration. In order to better assess flows with turbulent fluctuations, an equation derived by Wyckham and Smits [63] is adapted to capture physical turbulent effects on EO/IR aberration. Specifically, the method was developed to capture the effects of the large eddies which are present outside of the near-wall region in turbulent flow. In deriving this model, it was assumed that the optical aperture is larger than the boundary layer thickness, as this conjecture compared well to experimental measurements at Strehl ratios greater than 0.3 [63]. The derivation of Method II begins with defining the root mean squared optical path difference (OPD) using Eqn. (3.5).

$$OPD_{RMS} = \int_0^L n' \, dy \; = \; \int_0^L K_{GD} \rho' dy \tag{3.5}$$

where n' is the fluctuating index of refraction, ρ' is the fluctuating density, and K_{GD} is the Gladstone-Dale constant. The OPD is the difference between the optical path length and the spatially averaged optical path length. The integral in Eqn. (3.5) is further simplified using the strong Reynolds' analogy and the ideal gas law; see Eqn.

(3.6).

$$OPD_{rms} = K_{GD}\rho_\infty \int_0^L (\gamma - 1) M_\infty^2 \sqrt{\frac{C_f}{2}} \left(\frac{T_\infty U_\infty}{TU} \sqrt{\frac{\rho_\infty}{\rho}}\right) \sqrt{\left(\frac{\overline{\rho u'}}{\tau_w}\right)} dy \tag{3.6}$$

where C_f is the skin friction coefficient, τ_w is the shear stress at the wall, γ is the specific heat ratio, and M_∞ is the freestream Mach number. It is assumed that this integral can be solved by averaging the variables over the path of interest. The averaging process is accomplished by relating the variables to their corresponding freestream values. For example, the average velocity was set to be 80% of the freestream velocity since this is the speed at which the large scale turbulent eddies convect. It should be noted that later, Gordeyev proved this approximation to be incorrect and that the convective velocity of the large scale motions can vary with Mach number [23]. However, it is shown that the velocity multiplier did not vary significantly for the flow parameters considered in the present study, therefore, the original value of Wyckham and Smits is used in the calculations [63]. With the aid of these scaling arguments, Eqn. (3.6) was reduced to Eqn. (3.7).

$$OPD_{rms} = C_w r_2^{\frac{-2}{3}} M_\infty^2 K_{GD} \sqrt{C_f} \rho_\infty \delta \tag{3.7}$$

where C_w is experimentally determined to be approximately 0.7 and is applied to correlate the simulations to experiments, δ is the boundary layer thickness, C_f is the skin friction coefficient, and r_2 is calculated for a non-adiabatic wall using:

$$r_2 = \frac{1}{2}\left(\frac{T_w}{T_\infty} + 1\right) \tag{3.8}$$

where T_w is the wall temperature and T_∞ is the freestream temperature. Equation (3.7) has been shown to compare well to experimental data [63]. Equation (3.7) is derived for a line of sight that is normal to the wall. Adjustments to the line of sight length will be made to estimate the distortion along non-perpendicular paths. The

estimate will not include the anisotropic features of the turbulent flow. In order to include these features, detailed information about the turbulent density fluctuations would need to be known. The final step in deriving Method II is to find the Strehl ratio; see Eqn. (3.9).

$$Rs = \exp\left(-\left(\frac{2\pi OPD_{rms}}{\Lambda}\right)^2\right) \tag{3.9}$$

where Λ is the wavelength of the signal.

The experimental value of C_w is modified to make simulations performed by LeMANS correlate with the published experimentations. To accomplish this, the case utilized in Ref. [63] is simulated using LeMANS. The experiment in [63] consists of a flat plate in Mach 7.7 air. The reported wall temperature is half of the adiabatic wall temperature [63]. The stagnation temperature and pressure are 700 K and 9.2 MPa, respectively [63]. It is assumed that the isentropic relations can be used to find the static temperature in the core of the flow. The static pressure altitude is provided and is 30 km [63].

The flat plate case is run using the Menter-SST turbulence model. The computation is run on a mesh with approximately 20,000 cells. The wall $y+$, a non-dimensionalized wall distance as defined in Eqn. (3.10), is below 0.5 for the entire length of the wall.

$$y+ = \sqrt{\frac{\tilde{\tau_w}}{\rho}}\frac{y}{\nu} \tag{3.10}$$

where τ_w is the shear stress at the wall and ν is the kinematic viscosity. The simulation ran for total time of 100 CPU hours.

Contours of density and Mach number are shown in Fig. 3.2 and illustrate the key aspects of this flowfield. The flow is typical of a hypersonic, high Reynolds number, flat plate case. It consists of a weak oblique shock at the leading edge of the plate and a thin boundary layer. Density decreases near the relatively hot wall, as the particles

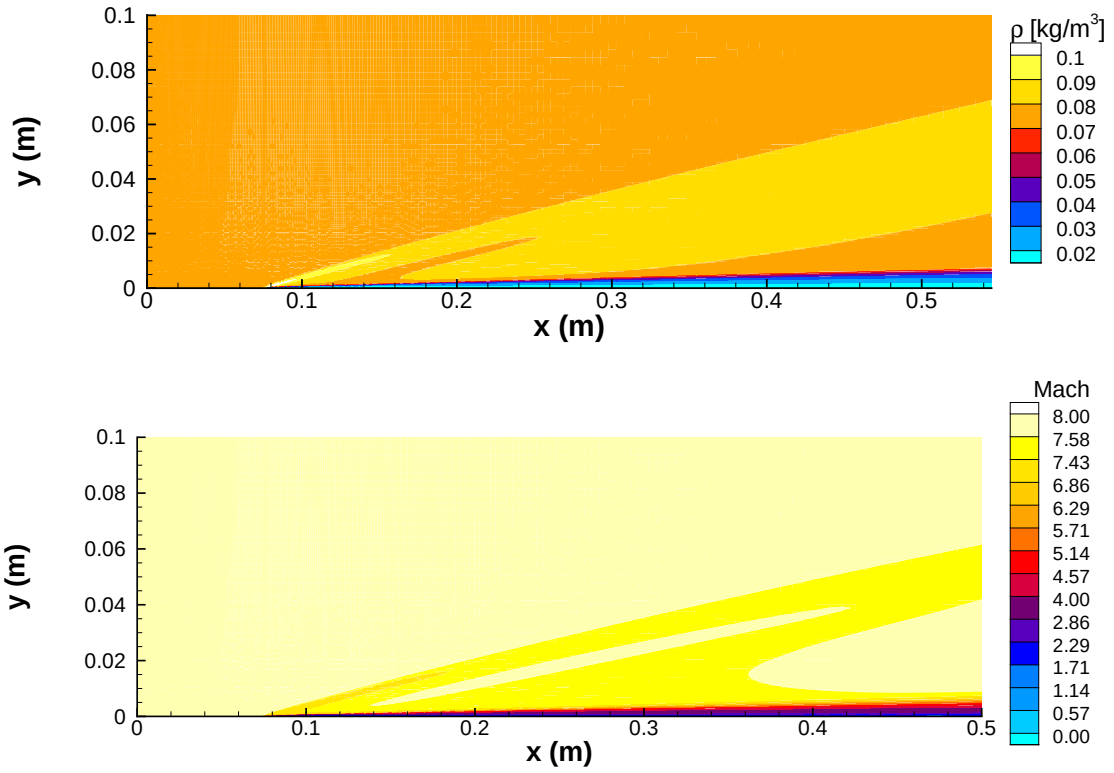

Figure 3.2: Density and Mach contours for the Mach 7.7 re-scaling

diffuse to the cooler portions of the flow. The conditions of the flow do not promote thermochemical nonequilibrium, as energy is insufficient to excite the molecules in the vibrational or chemical modes.

The formula derived by Wyckham and Smits is re-scaled for use with LeMANS by rearranging Eqn. (3.7); see Eqn. (3.11):

$$C_w = \frac{OPD_{rms}}{r_2^{\frac{-2}{3}} M_\infty^2 K_{GD} \sqrt{C_f} \rho_\infty \delta} \tag{3.11}$$

All values required, expect for the experimentally obtained OPD, in Eqn. (3.11) are provided by the LeMANS simulation. All of the quantities in Eqn. (3.11) are extracted at an x location of 0.356 m to be consistent with the experiments. The calculated value of C_w for use with LeMANS is 0.93. It should be noted that for visible

wavelengths, the Gladstone-Dale constant takes the value of $2.27 \times 10^{-4}\ m^3/kg$ for perfect air. The value of the Gladstone-Dale constant for infrared signals is derived by dividing the corrected n-1 profile from Ref. [33] by the density profile according to Eqn. (3.3) [33]. These calculations provide a Gladstone-Dale value of 2.23×10^{-4} m^3/kg for infrared wavelengths.

Method II is derived for a flow with no pressure gradient in the direction normal to the wall. For the vehicle considered in this study, the surface possesses a slight radius of curvature, and a pressure gradient in the normal direction is present. After completing an order of magnitude analysis and integrating over the boundary layer, it is found that this pressure gradient is proportional to the ratio of the boundary layer thickness to the radius of curvature of the surface. The proportionality suggests that the pressure gradient is negligible if the boundary layer thickness is much smaller than the radius of curvature of the vehicle. The geometry in this study fulfills the proportionality requirement at distances sufficiently far from the nose.

3.2.2 RF Analysis

A vehicle traveling at hypersonic speeds will experience strong shocks creating high flow temperatures. A plasma sheath can then form around the vehicle, resulting in radio blackout. A plasma sheath can cause signals sent or collected by the vehicle to degrade. Finding the critical plasma density above which the signal will become distorted is integral to analyzing radio blackout, see Eqn. (3.12) [48].

$$n_{critical} = \left(\frac{f_{radio}}{8.985} \right)^2 \tag{3.12}$$

where f_{radio} is the frequency of the RF signal of interest. Figure 3.3 presents the critical plasma density over a common range of operational radio frequencies. When a signal experiences degradation, the attenuation per unit length can be calculated

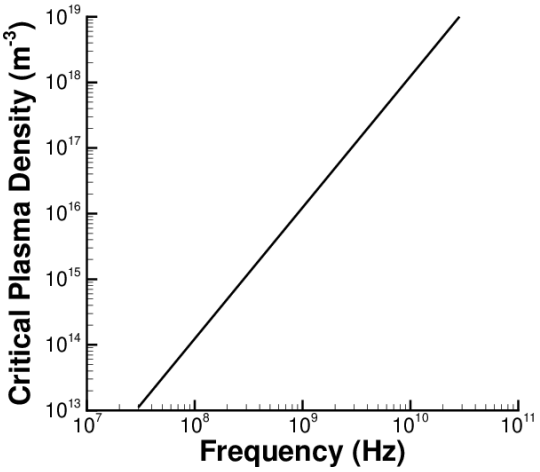

Figure 3.3: Critical plasma density for various RF frequencies

using Eqn. (3.13) [48].

$$\kappa = 1.821 \times 10^{-7} \sqrt{80.255 n_p - f_{radio}} \tag{3.13}$$

where n_p denotes the plasma number density.

Common frequencies used in sensing applications can range anywhere from 0.03 to 40 GHz. Table 2.1 summarizes several common sensor frequency ranges.

Table 3.1: Common Radio Frequencies used for Communication

Frequency Range	Use
0.03-0.3 GHz	Voice Communications
0.3-3.0 GHz	Data Telemetry and Voice Communications
1.0-2.0 GHz	GPS
2.0-4.0 GHz	Data Telemetry
8.0-12 GHz	Data and Satellite Communication
27-40 GHz	Radar and experimental communication

3.2.3 Surface Temperature

The CFD analysis provides the surface temperature profile. It is common for the air-breathing vehicles engaged in sensor specific missions to employ silica and sapphire

windows on the sensors. These materials can withstand temperatures of 1270 K and 2270 K, respectively [33]. The RF sensors may also contain ceramic elements made of silicon nitride that are exposed to surface temperatures. Silicon nitride can withstand temperatures up to 2173 K.

3.3 Simulation Conditions

The numerical setup is divided into two sections. Section 3.3.1 presents the freestream flow parameters. Section 3.3.2 presents the geometry and computational mesh.

3.3.1 Flow Parameters

To investigate the effects of hypersonic flow on signal degradation, a test case is run in air at Mach 7 and an altitude of 30 km. The flow conditions are as described in Table 3.2. These simulations employ a radiative equilibrium wall boundary condition

Table 3.2: Study Flow Parameters

Parameter	Value
M_∞	7.00
ρ_∞	0.018 kg/m^3
T_∞	227 K
P_∞	11.7 kPa

and utilize thermochemical nonequilibrium modeling in the flowfield. For this simulation, it is assumed that the wall emissivity is 1.0. The Menter SST closure model is used. Cases are run with 5 species and 11 species chemistry. For the 5 species (N_2, O_2, NO, N, and O) and the 11 species chemistry (N_2, O_2, NO, O, N, N_{2+}, O_{2+}, NO_+, N_+, O_+, and e_-) mechanisms, a finite-rate chemistry model is used with Park's two-temperature model [43]. To determine viscosity, Wilkes's mixing rule is used in conjunction with Blottner's curve fits [60], [7]. Eucken's relations are used to find thermal conductivities.

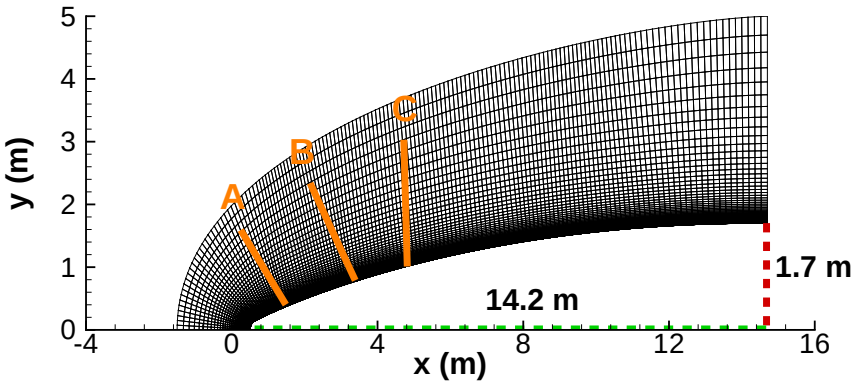

Figure 3.4: Depiction of simulation geometry

3.3.2 Geometry

The geometry for this case is intended to be representative of a typical hypersonic ISR platform. It consists of an axisymmetric cone that is approximately 14 meters long and has a 1.7 meters radius. The geometry is depicted in Fig. 3.4. A structured mesh is created with the commercial software Pointwise. The mesh contains approximately 29,000 cells. The simulations are performed on 16 processors and each take 325 CPU hours, total time. All test cases are run on the same mesh to facilitate detailed comparison. The computational mesh has y+ values of less than one for all cells adjacent to the wall. The mesh is shown in Fig. 3.4.

3.4 Results

The results are presented in three sections. The first section discusses the results of the preliminary EO/IR signal distortion analysis. The second section presents the results pertaining to radio blackout. The final section presents the results regarding surface temperature considerations.

3.4.1 Optical Analysis

The optical calculations are carried out along the three paths shown in Fig. 3.4. The three paths are evenly spaced and placed sufficiently far away from the stagnation region to avoid pressure gradient effects. Furthermore, these locations are chosen to be towards the fore-body and away from the potential location of a propulsion system where flow conditions are likely to be highly disruptive to signal propagation.

Figure 3.5 presents the density and Mach number contours over the Mach 7 flow-field. The high kinetic energy of the oncoming flow causes the density near the wall to increase which pushes the shock closer to the body to maintain the conservation of mass. In the area near the nose, the flow is shocked to subsonic velocities, as indicated in Fig. 3.5b. Regions away from the stagnation region experience a weaker, oblique shock, as the flow is still supersonic post-shock. In Fig. 3.5, we also see relatively high density within and near the shock. This elevated density increases nearer to the stagnation region where the shock is of higher strength. The density decreases near the wall as species diffuse from the relatively hot wall (heated by viscous interactions between the wall and the fluid).

The varying strength of the shock is further illustrated in Figs. 3.6, 3.7, and 3.8. These figures show profiles of the properties with direct optical ramifications (those terms which affect the index of refraction via Eqn. (3.4)) along Paths A, B, and C, respectively. Path A experiences rapid changes in temperature and pressure, while the other profiles experience more gradual changes.

3.4.1.1 Analysis Using Method I

The temperature and pressure profiles are extracted and presented in Figs. 3.6-3.8a. The index of refraction is corrected for the temperature and pressure values for each profile using Eqn. (3.4). The index of refraction profiles are then presented in Figs. 3.6-3.8b. The variance in index of refraction dictates the level of electro-

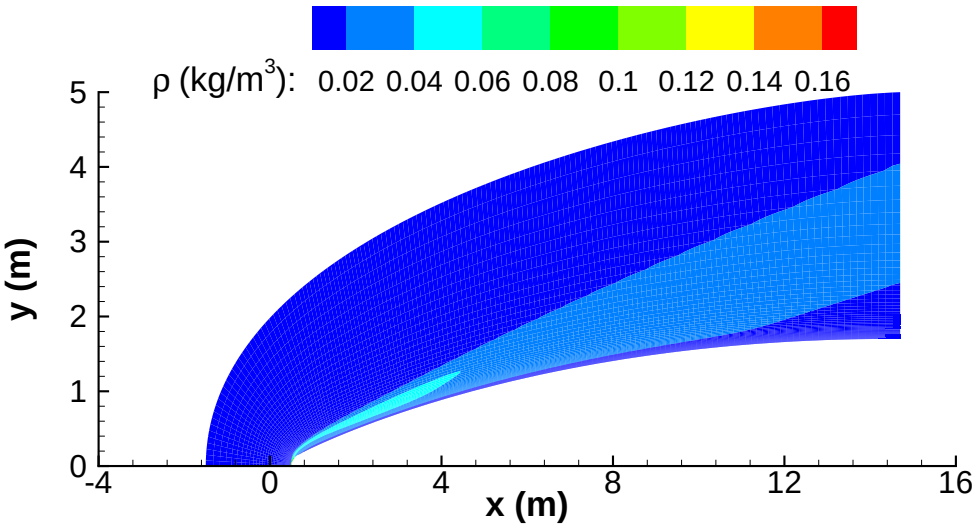

(a)

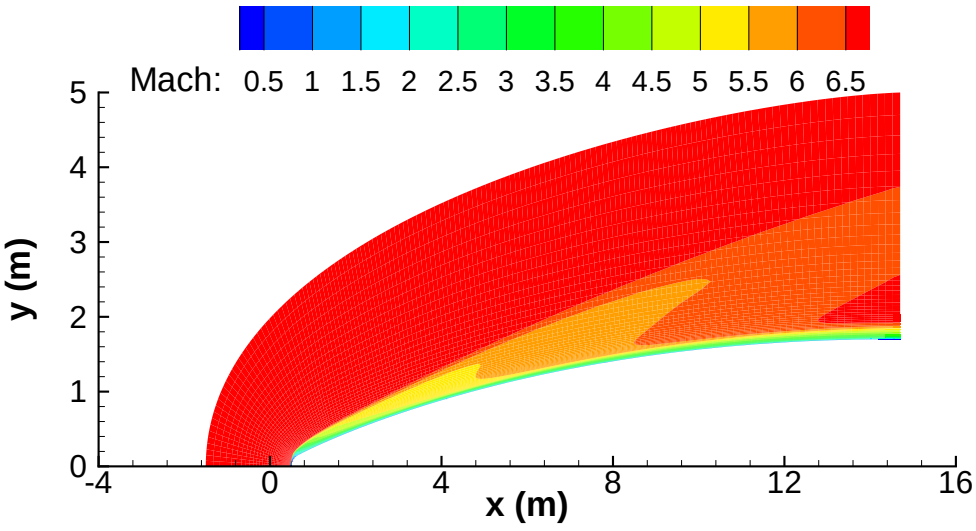

(b)

Figure 3.5: Density contour, (a.), and Mach contour, (b.), for the Mach 7 flow

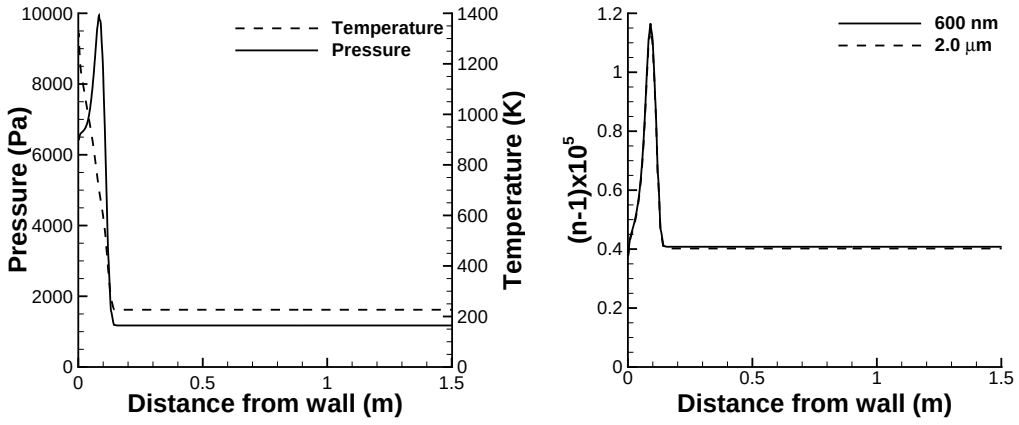

(a) (b)

Figure 3.6: Temperature and Pressure profiles, (a.), and index of refraction profiles, (b.), extracted along path A

optical or infrared distortion. It should be noted that Method I only predicts the optical distortion from the variation of index of refraction across the boundary layer provided by the RANS simulation, as such only the mean index of refraction is utilized with this method. Therefore, this method does not directly consider the fluctuating mechanisms of turbulent flow. It does, however, account for aspects such as elevated wall temperatures and the resulting mean density profiles. The method employed here provides an accurate estimate of aberration if turbulent fluctuations have little effect on optical distortion calculations. The pressure and temperature profiles along Path A are presented in Fig. 3.6a. The temperature is highest at the wall which causes a slight decrease in density near the wall, as can be predicted by the ideal gas law; see Fig. 3.6. The pressure increases sharply from the freestream value due to the shock. Pressure then decreases slightly in the near wall region, as the flow expands to satisfy the wall conditions.

The index of refraction is presented in Fig. 3.6b. In the figure, we can see that the index of refraction profile shows a similar trend to the pressure profile; both curves rise away from the wall before falling to the freestream value.

The temperature, pressure, and index of refraction profiles are presented in Figs.

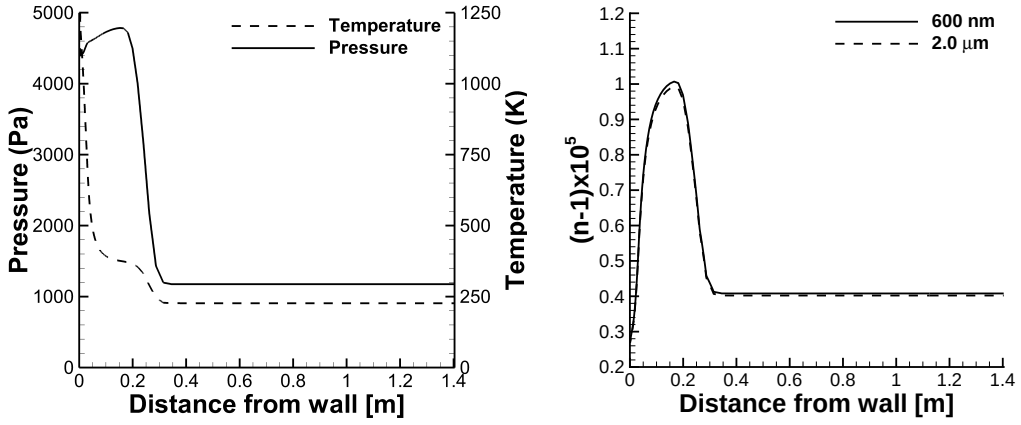

(a) (b)

Figure 3.7: Temperature and Pressure profiles, (a.), and index of refraction profiles, (b.), extracted along path B

3.7 and 3.8 for Paths B and C. These figures illustrate the differing strength shocks that occur over various portions of the vehicle's body as indicated by the temperature and pressure gradients present in each path's profiles. The gradients in Path B and C's profiles are smaller when compared to Path A's gradients in temperature and pressure. The resulting gradients in index of refraction have optical implications; the gradients are integrated over each region of interest, in this case the boundary layer, to arrive at the Strehl ratio.

The pressure and temperature profiles for Paths B and C largely follow the same trend as Path A's profiles. Temperature is highest near the wall and then falls off toward the freestream. Pressure decreases slightly near the wall, increases in the shock, and then decreases to the freestream value. A notable difference between Paths B and C is the distance the signal must traverse inside the boundary layer. Path B crosses the boundary layer at a larger angle relative to the vertical than Path C. For this method of optical analysis, the distance a beam must traverse plays a large role in the distortion the beam will experience. However, it must be noted that this method is not intended to account for the effects of the strong gradients within the flowfield.

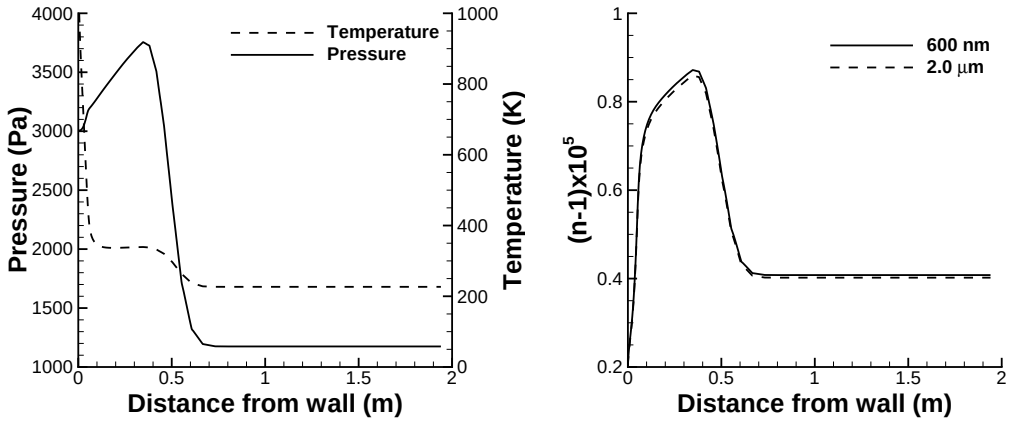

(a) (b)

Figure 3.8: Temperature and Pressure profiles, (a.), and index of refraction profiles, (b.), extracted along path C

With the temperature and pressure data, and the aid of Eqns. (3.1) through (3.4), the Strehl ratios in Table 3.3 are produced utilizing Method I. The Strehl ratio is the ratio of the peak intensity of the distorted image to the peak intensity of an unaberrated image. A completely undistorted image would have a Strehl ratio of 1. The Strehl ratios produced by Method I are close to 1, with the exception of the

Table 3.3: Strehl ratios produced by method I

Location	Optical (λ=600 nm)	Infrared (λ=2 μm)
Path A	1.0	1.00
Path B	0.732	0.973
Path C	0.901	0.991

optical distortion in Path B. Path B experiences a larger distortion due to the distance the beam must travel along this path as well as the relatively high level of variation in the index of refraction (when compared to Path C). These Strehl ratios suggest this flow does not distort an EO/IR beam to a great extent. Method I provides a best case scenario signal distortion level because it does not directly account for turbulent fluctuations. This method is not well suited for flow features such as shocks, another method is investigated.

3.4.1.2 Analysis Using Method II

Method II is adapted from an equation presented by Wyckham [63]. In this analysis, the same paths are utilized as with Method I. The Strehl ratios are produced with Eqs. (3.7) and (3.9). Table 3.4 shows the Strehl ratios calculated with Method II. The Strehl ratios predicted with Method II are lower than those predicted with

Table 3.4: Strehl ratios produced by Method II

Location	Optical (λ=600 nm)	Infrared (λ=2 μm)
Path A	0.951	0.996
Path B	0.036	0.749
Path C	0.155	0.851

Method I. The findings highlight the importance of including turbulent fluctuations. These fluctuations have a strong effect on optical distortion which is not captured by Method II. Method II was derived to specifically handle the large eddy motions within the boundary layer. It is likely that this method under predicts Strehl ratios when they are 0.3 or below [63]. Like Method I, Method II is derived for a very specific flow type while employing many assumptions (e.g., no pressure gradients and application of the strong Reynolds analogy).

3.4.2 Radio Blackout

The plasma density is explored along the same paths that are utilized for the EO/IR analysis. Three plasma density profiles, representative of Paths A, B, and C, are shown in Fig. 3.9. Path C experiences the highest plasma number density with a peak number density of $4.22 \times 10^8\ m^{-3}$. With this peak value and Eqn. (3.12), the radio frequency below which the signal will be distorted is found. An RF signal with a frequency of 1.8 x 10^2 kHz or lower would be obscured if it traverses Path C. This frequency is well below the frequencies used in most sensor applications (see Table 3.1). The lowest frequency of interest in Table 3.1 is two orders of magnitude larger. Furthermore, the highest plasma density over the entire geometry used in this

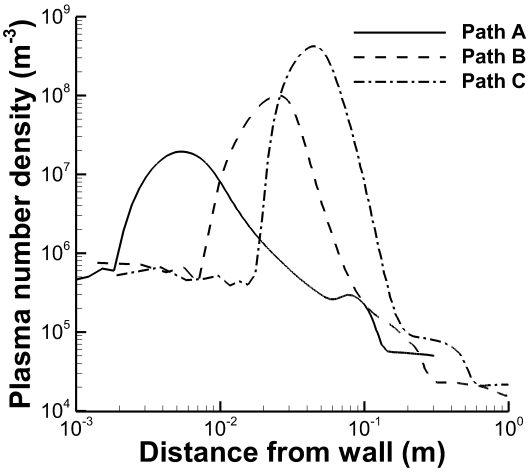

Figure 3.9: Plasma Density profiles extracted along the three paths in Fig. 3.4

study is 1.09 x $10^9 m^{-3}$. This represents a critical plasma density for signals of 2.97 x 10^2 kHz which is also far below the frequencies discussed in Table 3.1. As a thought experiment, another simulation is run at an altitude of 20 km. The low altitude corresponds with a higher density that will cause the number of energy exchanging collision to increase. The plasma density in this simulation predicted that frequencies at 7.5 x 10^2 kHz or below will be distorted.

3.4.3 Surface Temperature Considerations

The profile of temperature along the vehicle surface obtained from the 30 km simulation is shown in Fig. 3.10. The peak surface temperature is approximately 1600 K at the stagnation point. The surface temperature findings suggest that as long as a silica window is not used at the stagnation point, the temperature of the vehicle surface is unlikely to cause any type of damage to the sensor or sensor window. The silicon nitride and sapphire windows, which can withstand temperatures above 2000 K, can be placed anywhere on the vehicle used in this study's surface.

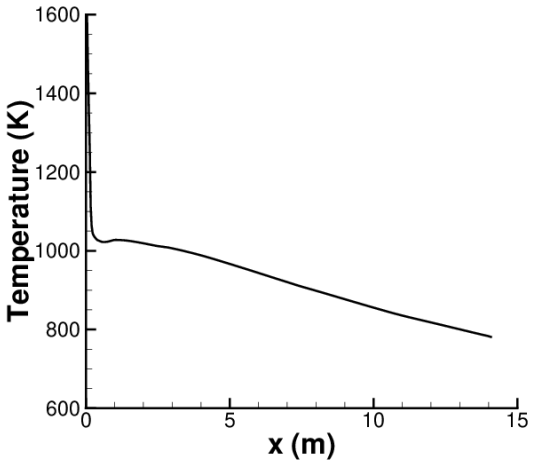

Figure 3.10: Profile of Surface Temperature

3.5 Summary

When traveling at hypersonic speeds, a number of different flow phenomena must be considered. These phenomena may impact ISR sensor performance. Three different types of sensor interference were considered in this preliminary study. EO/IR aberrations, RF signal degradation, and elevated surface temperatures were analyzed to determine if they are significant. For the Mach 7, 30 km altitude case considered, it was determined that optical and infrared signals may be highly distorted when traversing the boundary layer; however, the methods employed in this study are insufficient for broad application of high fidelity signal assessment. Both models were derived for specific flow types and it is unclear how they perform when the flow type deviates from the original assumptions. Both methods also have multiple shortcomings. The existing equation in Method II does not account for the anisotropy that is inherent in turbulence. A study showed that the differing turbulent structures affect the distortion in different manners. Hairpin vortices are particularly detrimental to optical signals [57]. Method II also is not intended for flow with strong pressure gradients. Method I may be unable to assess flow through a shock. Furthermore, neither method provides information regarding the specific role of turbulence and

thermochemical nonequilibrium in signal degradation. As such, more rigorous, high fidelity methods are required to assess EO/IR sensor distortion in hypersonic shock layers.

This study also showed that at the conditions in this study, it is unlikely that there will be interference with RF signals. The critical plasma densities for sensors that are commonly utilized are much higher than the plasma densities produced in this study.

The final aspect of his study was an analysis of the surface temperature. This investigation yielded surface temperatures that would not degrade the sensor windows unless the sensor is placed on or near the stagnation region. The particular material properties of the sensor windows should be included in future simulations such as emissivity and thermal conductivity.

CHAPTER IV

Effects of Modeling Thermochemical Non-Equilibrium

4.1 Introduction

To accurately assess signal propagation through a hypersonic flowfield, high enthalpy flow physics need to be appropriately accounted for in optical distortion prediction. Specifically, high enthalpy effects in high gradient regions, such as strong shocks and boundary layers, need to be addressed in the optical assessments. When the flow passes through these high gradient regions, it takes a finite amount of collisions for the internal energies to adjust to a new thermodynamic state, often resulting in regions of nonequilibrium and relaxation [55]. Vibrational and chemical energy exchange processes are often relatively slow (compared to translational and rotational energy exchange processes) to adjust to the rapidly changing flowfields, and thus nonequilibrium in these modes prevail.

Chapter IV presents flows over a blunt body at freestream Mach numbers of 11, 13, and 15. These Mach numbers are chosen to illustrate the effects of varying degrees of nonequilibrium in the flowfield around the body. The blunt body consists of a hemisphere cylinder that has a nose radius of 7 mm and a total length of 10 mm. The free stream parameters correspond to previous experiments and computations and are

repeated in Table 4.2 [42]. In this study, we perform nonequilibrium computational fluid dynamics (CFD) analyses, and we focus on the effects of nonequilibrium on optical properties, specifically, the influences on optical path length (OPL) and optical path difference (OPD).

After a presentation of the general flow fields of each of the Mach flows, in section 4.3.1, Chapter IV presents a comparison of the real gas flows to simulations that are performed utilizing a calorically perfect gas assumption. The Gladstone-Dale relation is used to calculate the optical quantities, with the appropriate constant values applied to each flow according to their respective mass fraction profiles. This comparison will quantify the effects that thermochemical nonequilbrium has on optical distortion through altering both the general flowfield (e.g. boundary layer thickness) and the aero-optical quantities (e.g. index of refraction).

Chapter IV also presents a detailed study regarding the sensitivity of optical distortion to nonequilibrium aero-optical quantities. In this portion of the study, we use the Gladstone-Dale relation to compute the index of refraction from the variables provided by the real gas CFD [4], [37]. The optical calculations are performed using two distinct Gladstone-Dale constants. The first uses a single Gladstone-Dale constant for (perfect gas) air, and the second uses a distribution of Gladstone-Dale constants calculated from the real gas mixture. The optical distortion provided by the perfect gas assumption (in the optical quantification) supplies a reference for the nonequilibrium optical calculations.

Finally, Chapter IV presents the effect of species mass diffusion on optical path length and optical path difference.

Chapter IV is structured as follows: Section 4.2 presents the freestream conditions and the grid convergence study; Section 4.3 shows the results. The results are further divided. Section 4.3.1 presents a general description of the real gas flow fields. Section 4.3.2 presents a comparison of optical distortion created by the real gas flows and

perfect gas flows. Section 4.3.3 illustrates the sensitivity of optical distortion to nonequilbrium modeling of optical quantities. Section 4.3.4 presents the effects of mass diffusion on optical distortion in real gas flows. Section 4.4 presents conclusions drawn from this study.

4.2 Conditions Investigated

The conditions of the numerical simulations are presented in two sections. Section 4.2.1 presents the flow conditions for the Mach 11, 13, and 15 studies. Section 4.2.2 discusses the grid convergence assessment performed for this study.

4.2.1 Flow Parameters

Three conditions are studied to assess the effects of nonequilibrium on optical assessments. The parameters that describe the flow for each are shown in Table 4.1. The flow parameters are derived from published computational and experimental data and are chosen because they promote thermochemical nonequilibrium to occur in the simulation. The Mach 11 case was compared with experimental data [42]. The geometry for all cases is an axi-symmetric hemisphere-cylinder with a 7 mm nose radius and a body that is 10 mm in length; see Fig. 4.1 for illustration. Note the areas in red and green which designate the areas of optical assessment. For each case an isothermal, non-catalytic wall is used.

Table 4.1: Test Conditions

Parameter	Test 1	Test 2	Test 3
Mach Number	11.2	13.2	15.2
$T_{wall}\,(K)$	1000	1000	1000
$T_{\infty}\,(K)$	293	293	293
$P_{\infty}\,(Pa)$	1200	1200	1200

The simulations in the present study utilizes AFRL's high enthalpy computational fluid dynamics code ANDEE. ANDEE couples the Navier-Stoke equations with

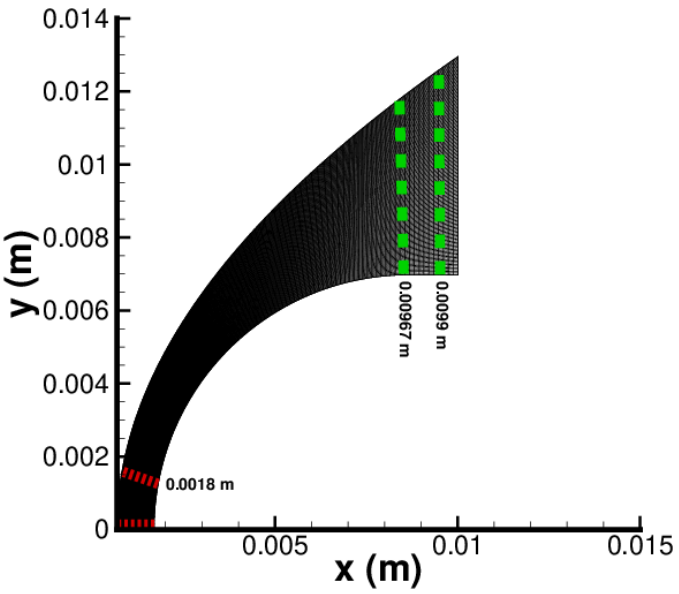

Figure 4.1: Schematic of grid with the solid lines denoting sensor windows and the area considered for optical assessment.

thermodynamic and transport models to simulate flowfields that experience thermochemical nonequilibrium. Vibrational relaxation is described using the Landau-Teller Model with Millikan and White relaxation times; see Chapter II.

4.2.2 Grid Convergence

Three grids are tested for convergence using each set of flow conditions. The coarse grid has 40 x 30 nodes (in the body normal direction and in the body tangential direction, respectively). The medium grid has 170 x 150 nodes. The fine grid has 240 x 210 nodes. For this study, we rely on densities for the calculation of optical properties, and it is ensured that there are enough grid points to capture the large gradients in the shock wave and in the boundary layer. Figures 4.2 and 4.3 show the mesh convergence for density variation normal to the surface at the forebody and aftbody, respectively. As can be seen in Fig. 4.2, at the forebody, the mesh density has an effect in the region of the shock front and is negligible in the rest of the shock

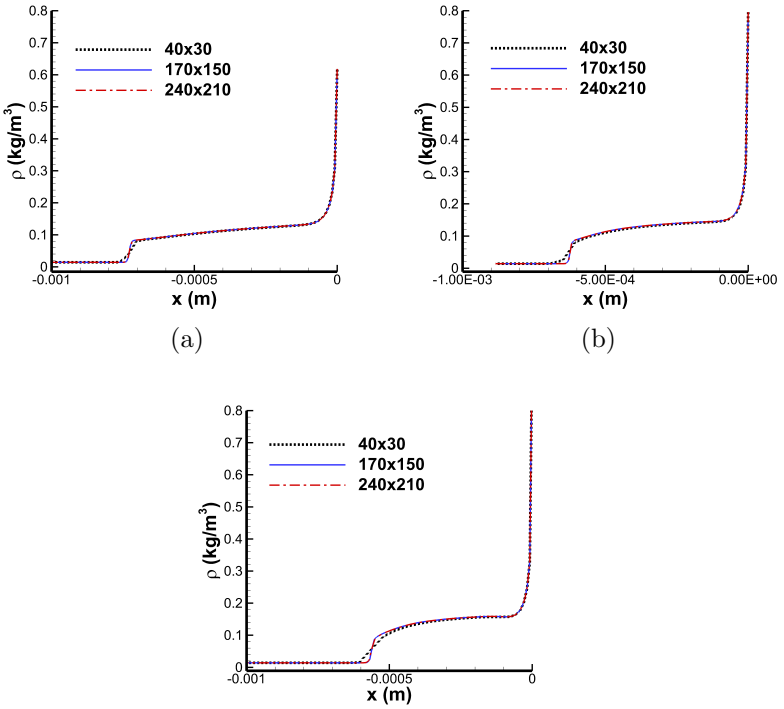

Figure 4.2: Grid Study: Mass density along the stagnation streamline for course, medium, and fine grids shown for (a.) Mach 11, (b.) Mach 13, and (c.) Mach 15.

layer. The shock fronts are located at 7.24×10^{-4}, 6.23×10^{-4}, and 5.63×10^{-4} m from the wall in Figs. 4.2a, b, and c, respectively. The effect of the grid on the solutions in the aftbody, Figs. 4.3, shows a greater dependence on the grid density in the shock layer and the boundary layer. It is determined that the medium grid is sufficient for this study. As Figs. 4.2 and 4.3 show density variation between the medium and fine grids is negligible for all cases (average absolute difference of less than 1%). The flow meshes are also used for the optical calculations.

4.3 Results

The results are divided into four sections. The first presents a general analysis of the nonequilbrium flow fields at Mach 11, 13, and 15. The next section presents a

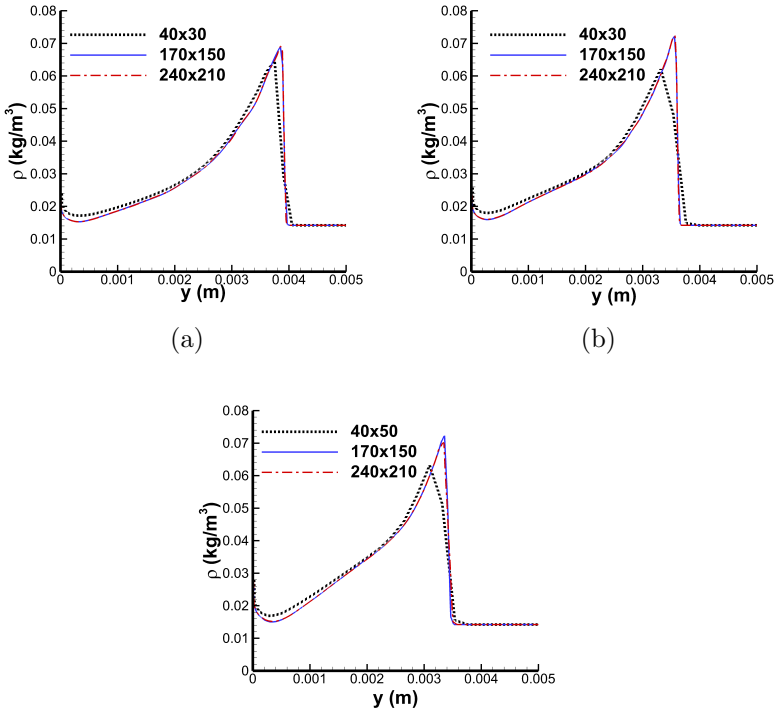

Figure 4.3: Grid study: mass density in the expansion zone (x=9.7 mm from the stagnation point) normal to the body for coarse, medium, and fine grids shown for (a.) Mach 11, (b.) Mach 13, and (c.) Mach 15.

comparison of optical distortion created by the real gas flows and a perfect gas flow. The third section presents the sensitivity of optical distortion to thermochemical nonequilbrium modeling of optical properties. The fourth and final section of the results presents the effects of species mass diffusion on optical distortion. Optical distortion in all sections is quantified using OPL and OPD.

4.3.1 General Flowfield Analysis

Figure 4.4 presents Mach number and translational temperature contours for Mach 11, 13, and 15. Figure 4.4a compares Mach contours of Mach 11 (top) and 13 (bottom), and Fig. 4.4b compares Mach 11 (top) and 15 (bottom). Shock standoff distance decreases with increasing Mach number due to an increase in endothermicity. The shock stand-off distances are increased by 7.68% for Mach 13 compared to

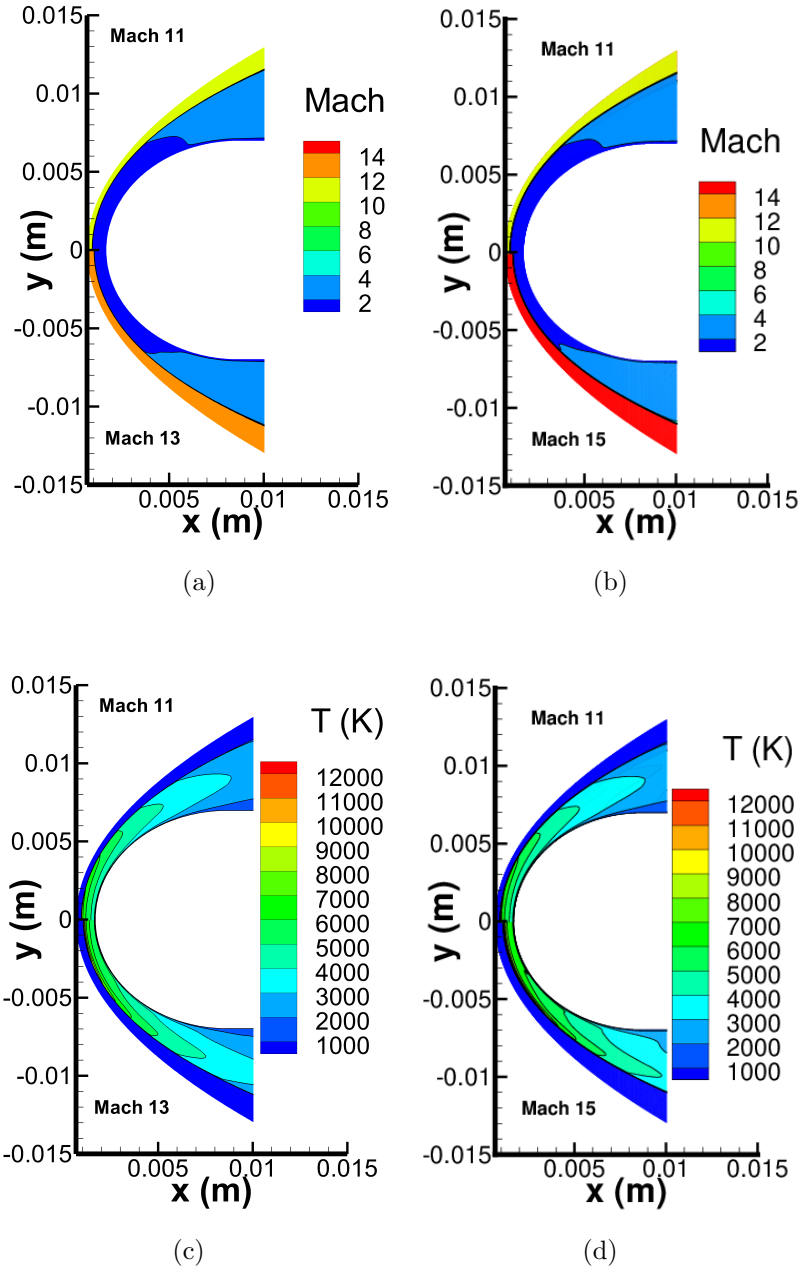

Figure 4.4: Comparison of Mach number contours, (a.) Mach 11 and 13, (b.) Mach 11 and 15, and comparison of temperature contours, (c.) Mach 11 and 13, (d.) Mach 11 and 15.

Mach 11, and by 22.3% for Mach 15 compared to Mach 11. Figure 4.4c compares temperature contours between the Mach 11 (top) and 13 (bottom) flows, and Fig. 4.5d compare temperature contours for Mach 11 (top) and 15 (bottom) flows. The flow in

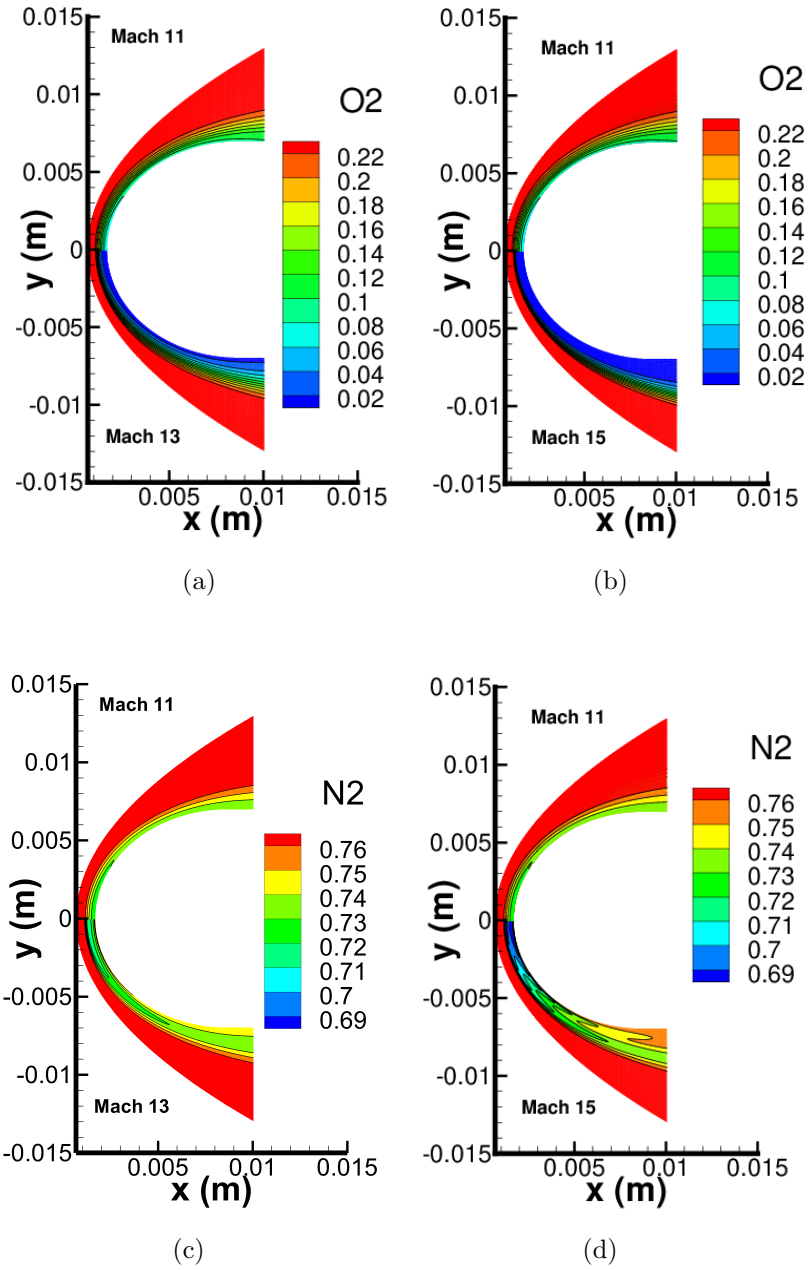

Figure 4.5: Comparison of mass fraction contours, (a.) O_2 for Mach 11 and 13, (b.) O_2 for Mach 11 and 15, (c.) N_2 for Mach 11 and 13, and (d.) N_2 for Mach 11 and 15.

the post-shock region of the forebody is slowed to subsonic speeds. The high kinetic energy of the oncoming flow is converted into random thermal energy in the shock wave which manifests as a higher translational temperature. Thus, flows at higher

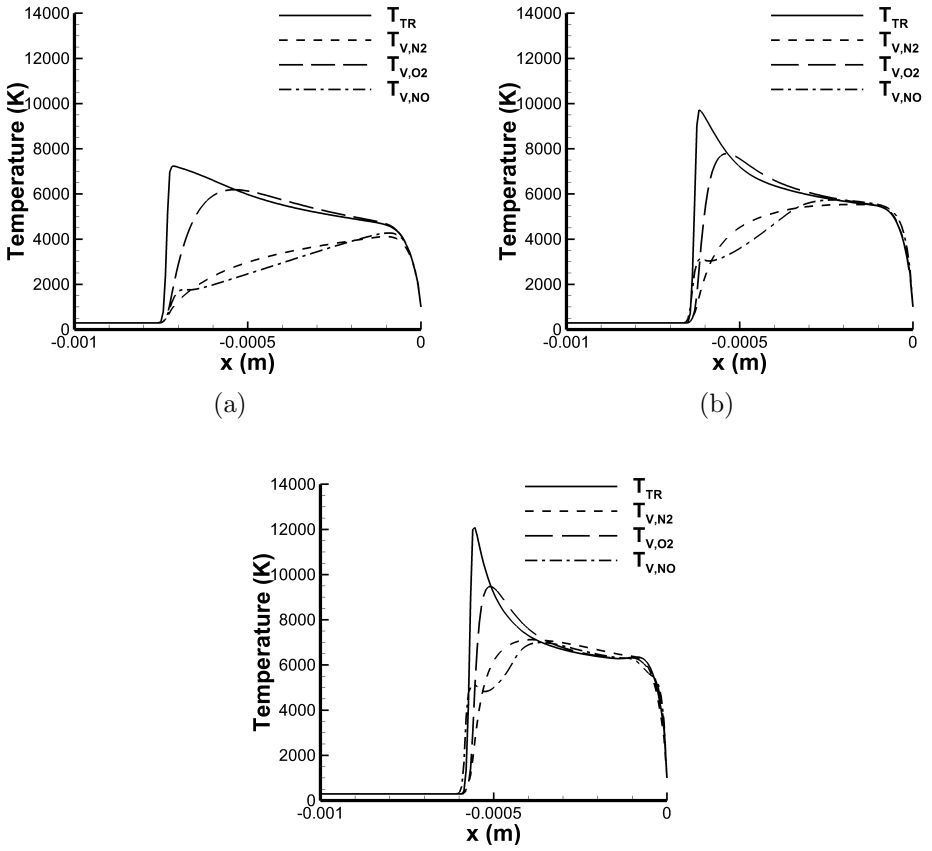

Figure 4.6: Temperature Distribution along the stagnation streamline for (a.) Mach 11, (b.) Mach 13, and (c.) Mach 15.

Mach numbers experience higher post shock temperatures. The highest post-shock temperatures are along the stagnation streamline, and the post-shock temperatures in the expansion region are reduced by a factor of approximately two for all freestream Mach numbers considered in this study. The effects of these energy exchanges behind the shock promote mass fraction profiles that vary throughout the flowfield. Figure 4.5a compares the molecular nitrogen mass fraction profiles for Mach 11 (top) and 13 (bottom), and Fig. 4.5b compares that for Mach 11 (top) and 15 (bottom). Post-shock temperatures reach 7000 K, 10000 K, and 12000 K for Mach 11, 13, and 15, respectively, as can be seen in Figs. 4.4c and d. These high post shock temperatures lead to higher dissociation for the higher Mach numbers. There is 92% less diatomic

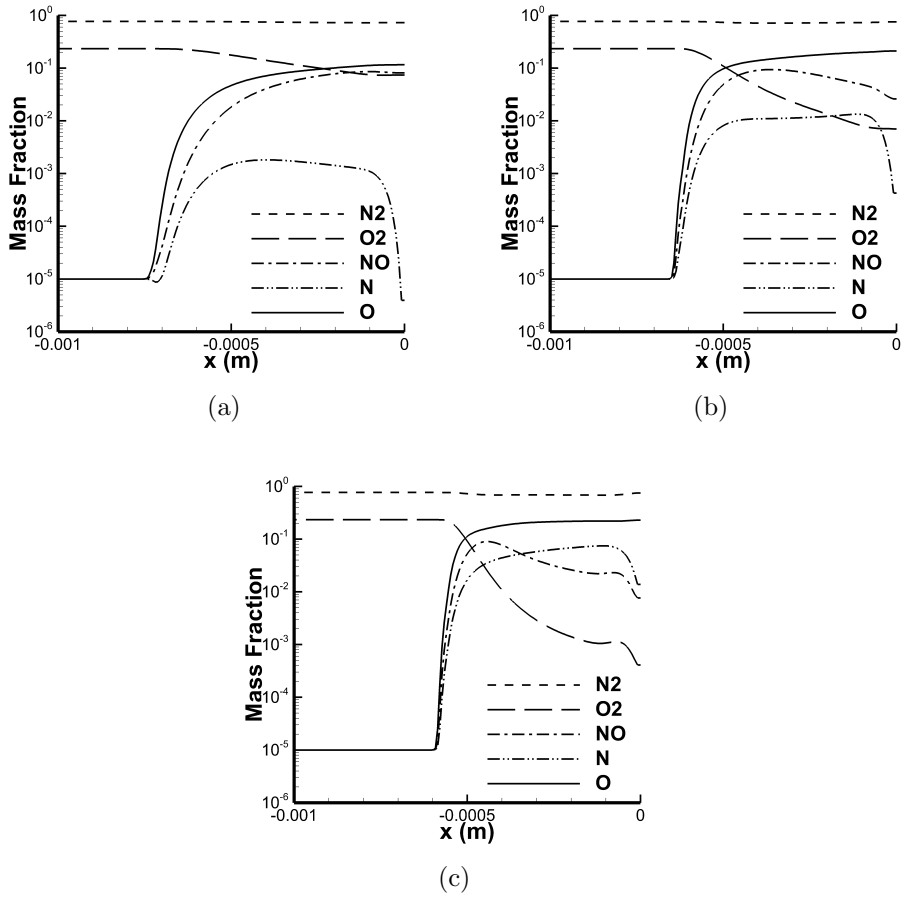

Figure 4.7: Mass Fraction Distribution along the stagnation streamline for (a.) Mach 11, (b.) Mach 13, and (c.) Mach 15.

nitrogen at Mach 13, and 99% less molecular nitrogen at Mach 15, than at Mach 11. Most of the dissociation occurs in the forebody, as seen in Figs. 4.5a and b for nitrogen and in Figs. 4.5c and d for oxygen. Oxygen dissociates more readily, and all of the oxygen is dissociated in the shock layer for the Mach 13 and 15 flow. In order to better examine the Mach 11, 13, and 15 flows, translational and vibrational temperature profiles along the stagnation streamline are shown in Figs. 4.6a-c, respectively. In the post-shock region, the translational temperature peaks at the highest value followed by the vibrational temperature of O_2, then N_2 and NO. The energy transfer occurs from the translational to the vibrational mode. It should be noted that at all Mach numbers there is equilibrium amongst the temperatures near the wall. This is

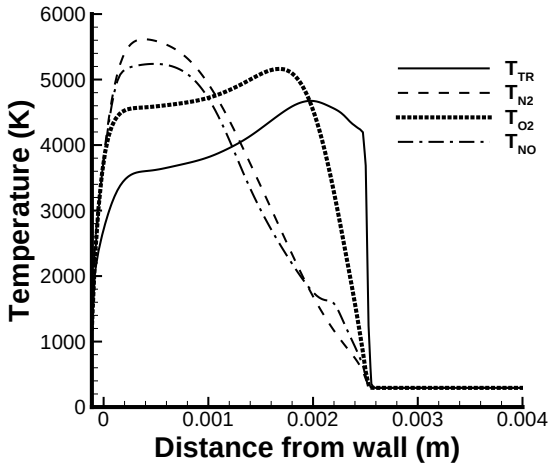

Figure 4.8: Temperature distribution normal to the surface at the aftbody (x=9.7 mm from the stagnation point).

an important consideration because optical sensors are placed on the vehicle's surface. The vibrational temperature rise of NO occurs before the rise in translational temperature for the Mach 15 flow and is attributed to an effect of mass diffusion of the NO molecules. Figures 4.6a-c show peak temperatures of 7000 K, 10000 K, and 12000 K for Mach 11, 13, and 15, respectively. The temperature equilibrates at 4000 K for Mach 11, 6000 K for Mach 13, and 7000 K for Mach 15. The higher Mach number flows reach equilibrium closer to the shock front due to more energetic collisions. Figures 4.7a-c show species mass fractions along the stagnation streamline for Mach 11, 13, and 15, respectively. Dissociation is coupled to the thermal excitation and occurs when the sum of internal energy exceeds the dissociation energy. The mass fraction of N_2 is highest at Mach 11 (Fig. 4.7a) and decreases at Mach 13 and 15 (Figs. 4.7b and c). The relatively cool wall (compared to the flow), promotes N_2 recombination as shown in Figs. 4.7b and c by an increase in the mass fraction of N_2 near the wall. There is significant dissociation of O_2 at Mach 11, and O_2 dissociates fully at Mach 13 and 15. NO formation occurs through the exchange reaction (Eqn. 2.4(iii)). The temperatures are insufficient at Mach 11 to cause NO to dissociate, as

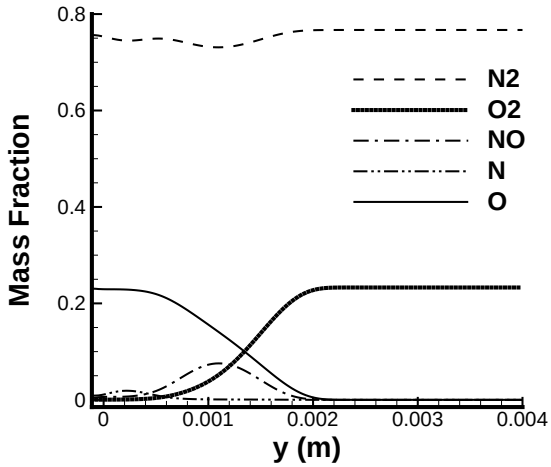

Figure 4.9: Mass fraction distribution normal to the surface at the aftbody (x=9.7 mm from the stagnation point).

shown in Fig. 4.7a. At Mach 13 and 15, NO does experience dissociation and peaks at 3.76×10^{-4} and 4.47×10^{-4} m from the wall, respectively.

Figure 4.8 shows the translational and vibrational temperature distribution along an extraction line normal to the wall and a distance of x = 9.7×10^{-3} m for the Mach 15 flow. In this region, the translational temperature is initially lower than the vibrational temperatures. The peak temperature in this region is approximately half of the temperature along the stagnation streamline, as in Fig. 4.6. Also, the temperature equilibrates much closer to the wall in the aftbody expansion region.

Figure 4.9 shows the mass fraction profiles normal to the wall in the expansion region at x= 9.7×10^{-3} m for the Mach 15 flow. When compared to the forebody, one can see that there is much less dissociation, particularly for N_2; however, O_2 is completely dissociated. NO peaks further away from the shock front at a distance of 1.04×10^{-3} m from the wall. This has implications on the optical properties. The real gas optical quantities in the aftbody are closer to the perfect gas value due to lower dissociation.

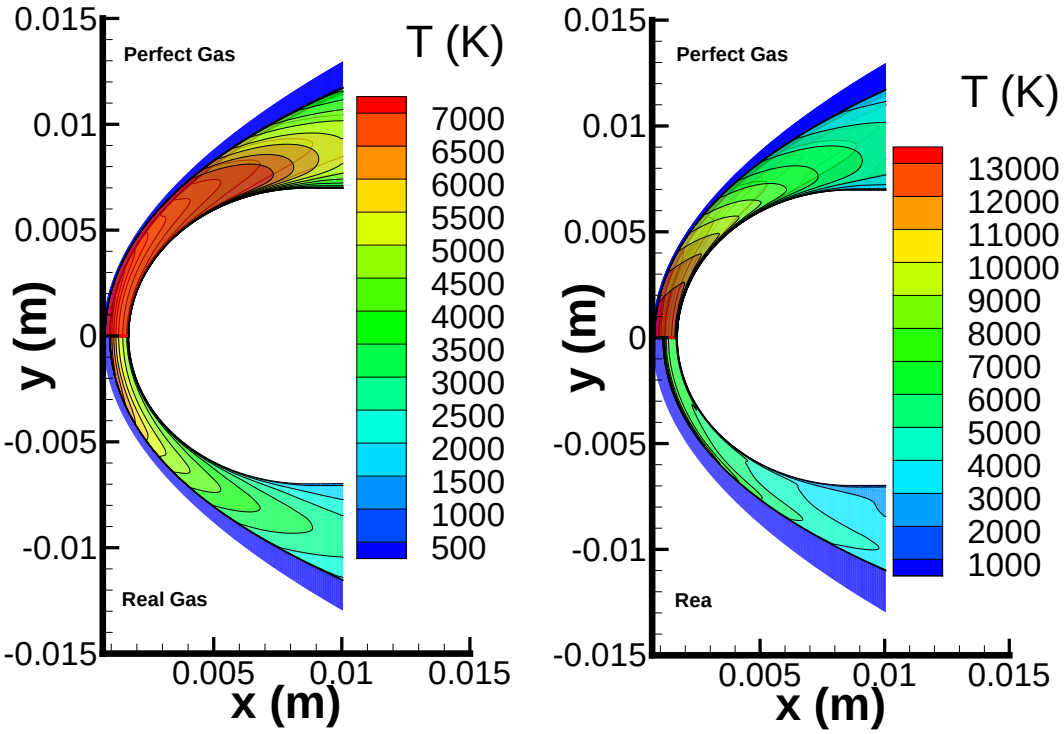

(a) (b)

Figure 4.10: Temperature Contours comparing Real and Perfect Gas Flows at Mach 11 and 15

4.3.2 Comparison with Perfect Gas Solution

The Mach 11 and 15 cases are compared to flows modeled as calorically perfect gases. Figure 4.10 shows translational temperature contours for the Mach 11 and Mach 15 flows, respectively. As shown in Fig. 4.10, the shock standoff is reduced in the real gas cases. For the Mach 15 flow, the shock standoff is reduced by about 82%, and for the Mach 11 case the shock standoff is reduced by approximately 83%. As discussed in section 4.3.1, the temperature in both flows is high enough to excite the chemical and vibrational modes. For both real gas simulations, energy is transferred into the excited chemical and vibrational modes. Thus, the temperature in the shock layer is lower in the simulations that are performed utilizing thermochemical nonequilibrium models. Pressure behind the shock is also higher in the perfect gas simulation

(when compared to the real gas simulation); as such, the pressure "pushes" the shock further from the body resulting in the increased stand-off distance that was discussed previously.

Figures 4.11 and 4.12 present the perfect gas density profiles extracted for both Mach 11 and 15 flows in the (forebody) stagnation and (aftbody) expansion regions. Note that the real gas profiles are shown again on the figures for ease of comparison. The density profiles for all flows are extracted normal to the wall.

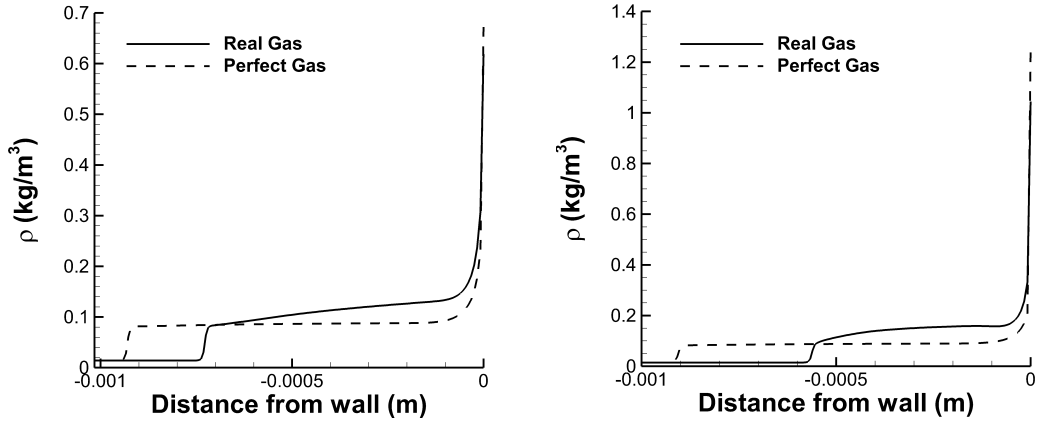

(a) (b)

Figure 4.11: Density profiles in the stagnation region for the Mach 11, (A.), and Mach 15, (B.), hemisphere flow

The sharp increase in density is indicative of the shock, and in Fig. 4.11, we can again see the reduction in shock standoff. In the post-shock region, the perfect gas temperature is higher causing the perfect gas molecules to diffuse further into the freestream (and have lower density).

Figure 4.12 presents a comparison of the density profiles in the aft-body expansion zone. Again, the density is extracted along a line beginning at the wall extending in a normal direction into the freestream. The real gas profiles for both Mach flows peak at a location preceding the peak in the perfect gas flow. In the region bounded by the wall and the location of the maximum density, the density in the real gas cases is higher than in perfect gas cases.

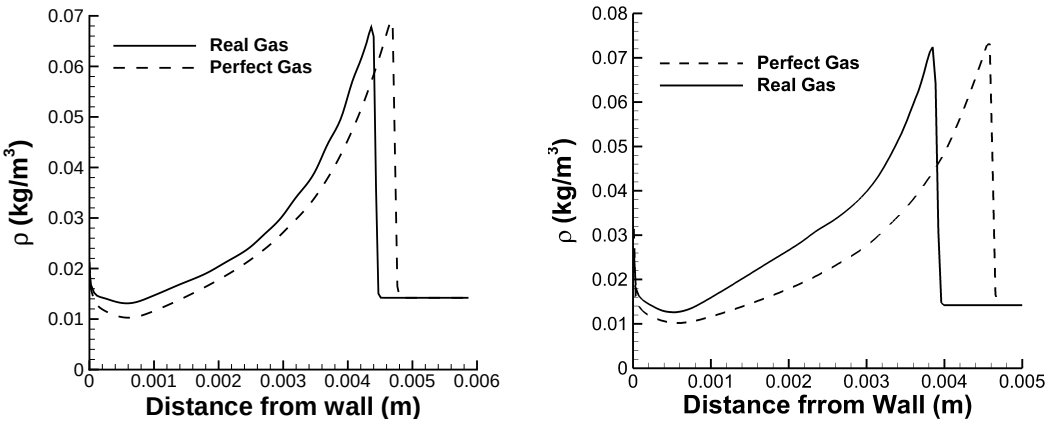

(a) (b)

Figure 4.12: Density profiles in the expansion region for the Mach 11, (A.), and Mach 15, (B.), hemisphere flow

Optical distortion analyses are performed on all flowfields. The distortion calculations are performed in two regions, as shown in Fig. 4.1. Note the two regions are bounded by the red lines for the fore-body and green lines in the aft-body. These regions are chosen because of the varying flow phenomena each area experiences. Flow in the fore-body stagnation region will experience a strong, almost normal shock and high heating while flow in the expansion region experiences a weaker, oblique shock. Each region will involve differing thermochemical nonequilbrium features in the real gas flows. These differences have been discussed above and may have optical ramifications.

Figure 4.13 presents a comparison of the optical distortion in the stagnation region for the Mach 11 and Mach 15 flows, respectively. The OPD_{RMS} is 0.6% higher for the real gas flow at Mach 11 and 5% larger for the real gas flows at Mach 15. For both Mach flows, the absolute difference in optical path length from the mean is maximum at the point nearest to the stagnation point. As distance along the wall is increased, the OPD profiles for the perfect and real gases approach each other. The slope in the real gas OPD decreases relative to the perfect gas slope in OPD. The relative decrease is caused by varying concentrations of species in the

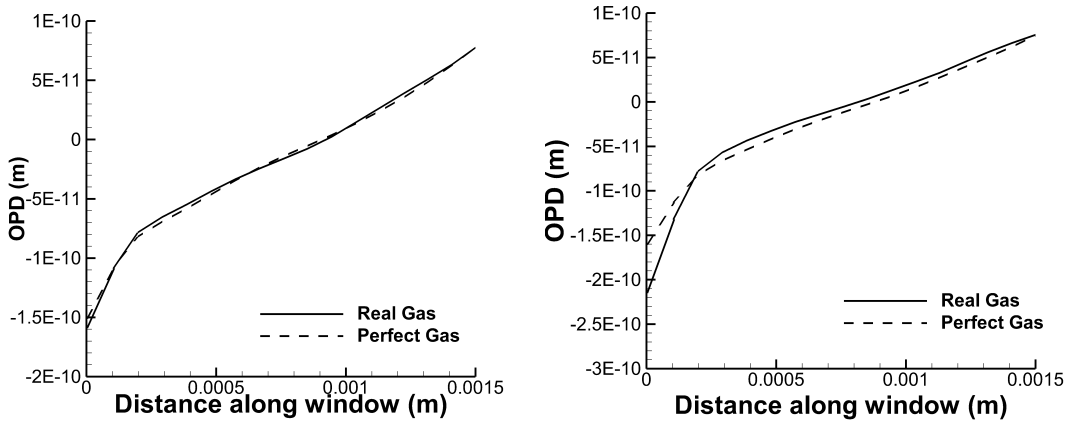

(a) (b)

Figure 4.13: OPD profiles for the hemisphere flow: (A.) Mach 11; (B.)Mach 15 in the stagnation region

real gas flows. Away from the stagnation point, the concentration of dissociated species decreases. Dissociated species have larger Gladstone-Dale constants than their respective molecular counterparts. The increase in the OPD caused by a larger shock layer height is competing with a decreasing Gladstone-Dale value for both real gas cases. We can also see in Fig. 4.13 that all profiles in the fore-body begin with an initially steep slope that then decreases due to the decreasing shock strength as distance from the nose is increased; see section 4.3.3.2 for further explanation. The Mach 15 flow experiences stronger shocks and consequently larger OPDs. All differences between the Mach 11 perfect and real gas optical distortions are very small with variation of less than 1%. A similar optical analysis is performed in the expansion region, denoted in green in Fig. 4.1. The OPD_{RMS} for real gas cases are 2% and 7% larger for the Mach 11 and Mach 15 flows, respectively. The OPD profiles for all flows are essentially straight lines. In this region, strong changes in gradients like those existing in the stagnation area, are not present. Figure 4.14 illustrates that the differences in OPD between the perfect and real gas flows are approximately symmetric about the center of the sensor "window." The mass fractions in this region do not cause the Gladstone-Dale value to vary significantly, and the real gas OPD

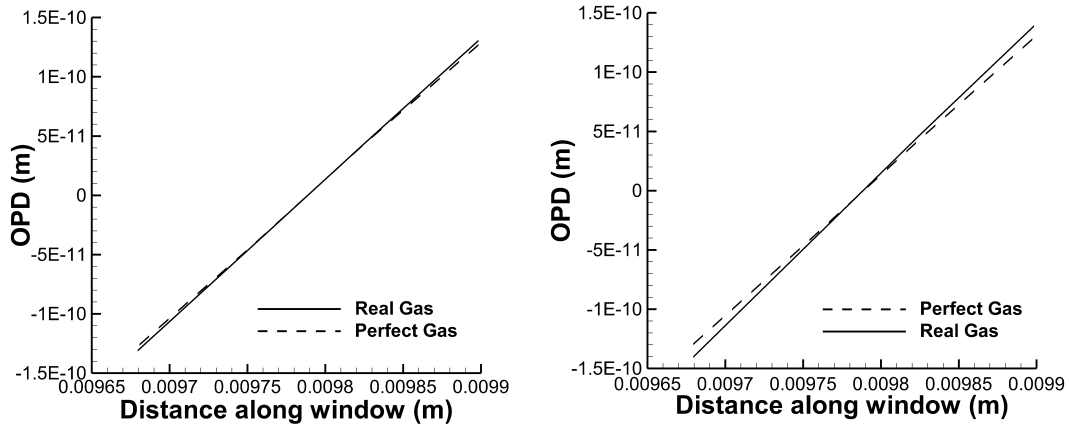

(a) (b)

Figure 4.14: OPD profiles for the hemisphere flow: (a.) Mach 11; (b.) Mach 15 in the expansion region

does not approach the perfect gas value.

4.3.3 Effects of Nonequilibrium Modeling in Optical Calculations

The results of subsection 4.3.3 are presented in three sections. The first section presents a discussion regarding the nonequilibrium flow features effect on the index of refraction. The effects of the index of refraction variation on OPL and OPD are presented in the second section. The third section discusses the effect of modeling species' mass diffusion on OPD and OPL.

4.3.3.1 Variation of Index of Refraction

The nonequilibrium flow field effects discussed in Section 4.3.1 lead to the variations in the index of refraction which can be attributed to changes in the Gladstone-Dale constants and density. Because the Gladstone-Dale constants are responsible for the variations between the (perfect gas) air and the real gas index of refraction at each freestream Mach number, they are discussed in this section. The nonequilibrium effect of dissociation will be highlighted since it directly influences the value of the Gladstone-Dale constant (via Eqn. (2.16)). It should be noted that thermal excita-

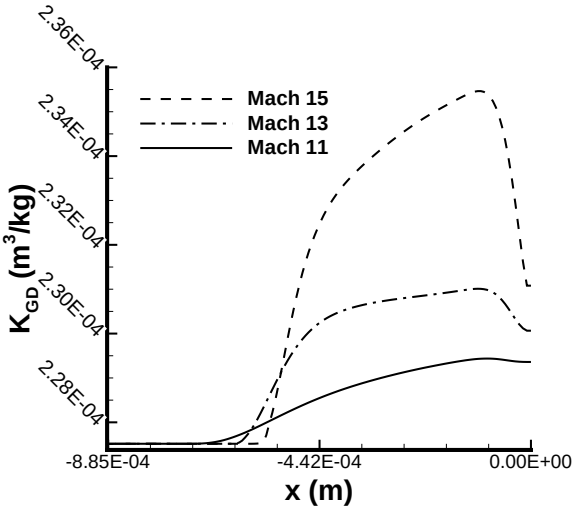

Figure 4.15: Profiles of the Gladstone-Dale constant along the stagnation streamline.

tion and dissociation are coupled processes in the flow and thus thermal excitation will also be accounted for in the optical properties. Figure 4.15 shows the profile of the Gladstone-Dale constants along the stagnation streamline for each Mach number. Of the three Mach numbers considered in this study, the Gladstone-Dale value peaks for the Mach 15 flow because of the high level of dissociation. In general, atoms have higher Gladstone-Dale constants than their molecular counterparts because, as explained in Chapter II Section 2.4, the Gladstone-Dale constant is inversely proportional to molecular weight. Figure 4.16 presents the relative importance of each species to the Gladstone-Dale constant, shown for N_2, O_2, NO, N, and O along the stagnation streamline for the Mach 15 flow. The figure shows the species mass fraction (black) as well as the relative contribution of each species to the total Gladstone-Dale constant of the air mixture (blue) which is calculated using Eqn. (4.1).

$$\left(K_{GD,s} \times \frac{\rho_s}{\rho} \right) K_{GD} \tag{4.1}$$

The relative contribution of the Gladstone-Dale constants of N_2 and N are higher than their respective mass fractions, whereas those of O_2 and O are lower. The

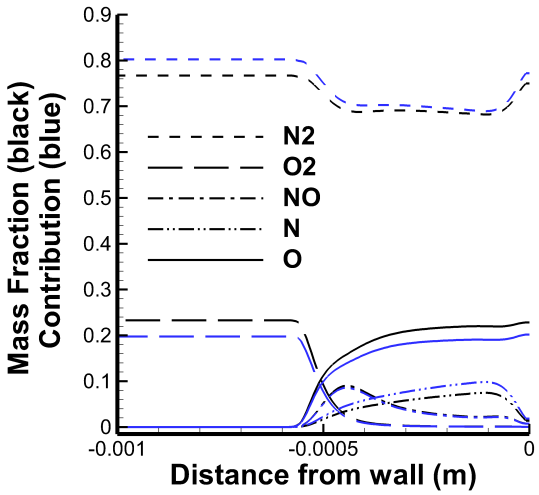

Figure 4.16: Comparison of species mass fractions with mass weighted fraction of Gladstone-Dale constant for each species along the stagnation streamline for Mach 15 flow.

contribution of NO to the Gladstone-Dale constant is comparable to the mass fraction of the species.

The variation of the Gladstone-Dale constant along the stagnation streamline is shown in Fig. 4.17. The figure shows the following: (1) the product of a species' Gladstone-Dale constant and its mass fractions and (2) the sum of these products over all species (total Gladstone-Dale value referred to in the figure as K_{GD}). It is noted that the largest contributor to the Gladstone-Dale constant at all Mach numbers is N_2 which has the highest mass fraction.

Atomic N and O affect the variation of the total mass-weighted Gladstone-Dale constant as follows. We see from Fig. 4.17 that the rise in total K_{GD} distribution in the post shock region follows the trend of $K_{GD,o}$ x Y_o as seen at approximately 6×10^{-4} m from the wall for all Mach numbers. In addition to the effects of atomic oxygen on the Gladstone-Dale constant, the increases in nitrogen atoms contribute to the rise in the Gladstone-Dale constant profile at Mach 13 and 15, Figs. 4.17b and c. However, in Figs. 4.17b and c, we see that the contributions of the oxygen atom are still dominant (over N).

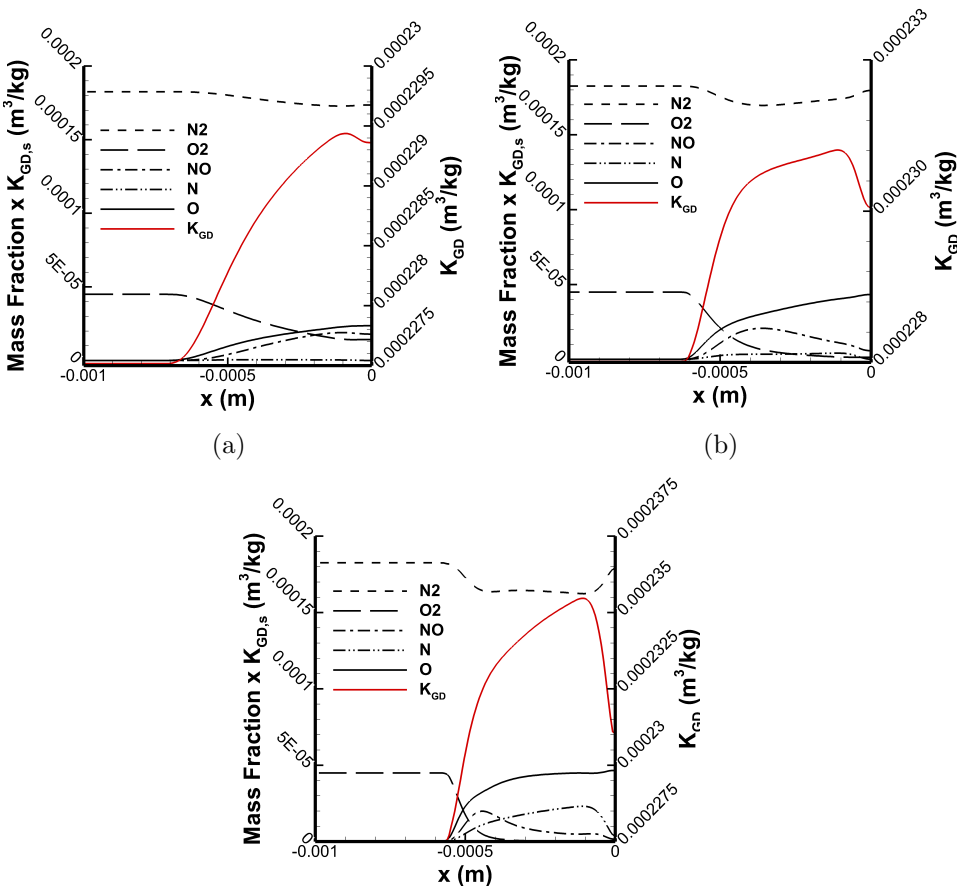

Figure 4.17: Profiles of the product of mass fraction and Gladstone-Dale constant along the stagnation streamline at (a.) Mach 11, (b.) Mach 13, and (c.) Mach 15.

The profile of the Gladstone-Dale constant for NO is directly proportional to the rise in the atomic species at Mach 11, Fig. 4.17a. At Mach 15, Fig. 4.17c, the NO mass fraction peaks at approximately 3.76×10^{-4} m from the wall. Consequently, there is a reduction in the slope of the total Gladstone Dale constant from 3.76×10^{-4} m to 9.85×10^{-5} m from the wall. Near the wall, we see that the Gladstone-Dale values decrease where the atomic nitrogen recombines.

4.3.3.2 Index of Refraction Variation effects on OPD

We now present the effect of the variation in the index of refraction (via varying Gladstone-Dale constants which are discussed above) on the optical distortion for

a signal that propagates normal to the body as shown in Fig. 3.25; the optical windows are shown schematically in red and green. The method for performing these calculations is outlined in Chapter II. The OPL considering the real gas effects in

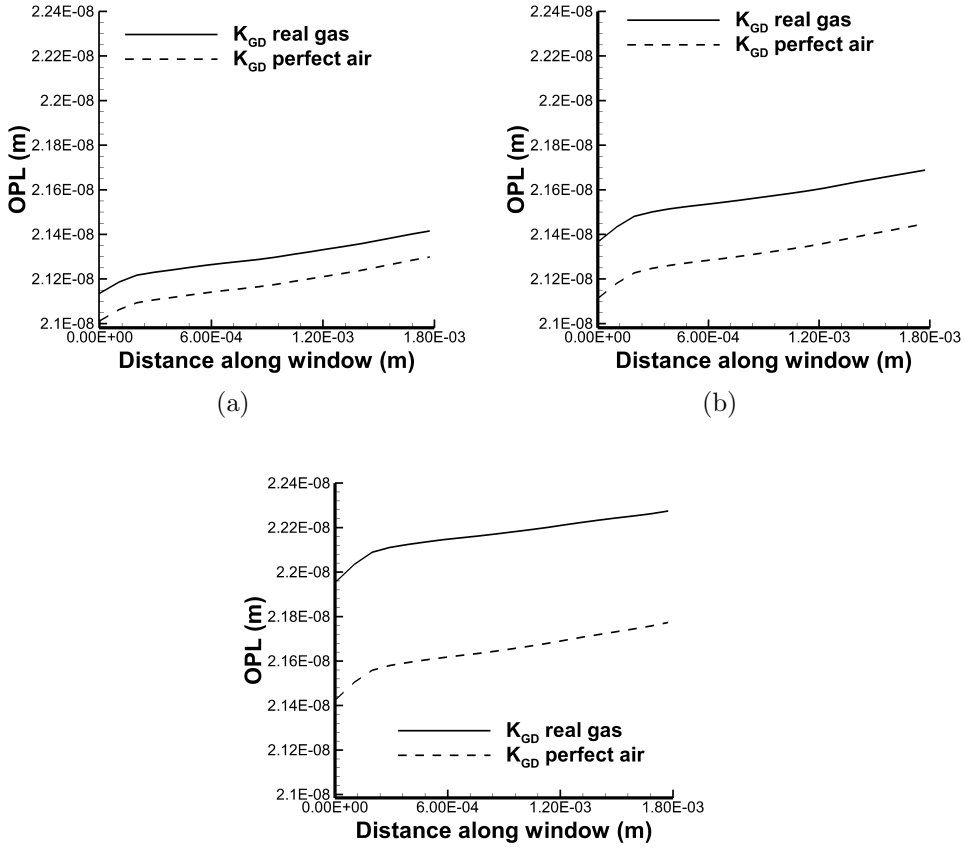

Figure 4.18: OPL in the red zone (Fig. 3.1) for (a.) Mach 11, (b.) Mach 13, and (c.) Mach 15.

the optical calculations for each Mach number is shown in Figs. 3.25a, b and c. The OPL using the Gladstone-Dale constant of (perfect gas) air is shown for reference. Both OPLs have a similar trend: there are strong thermal gradients in the stagnation region causing the rise in OPL, Fig. 4.18, up to approximately 2×10^{-4} m from the stagnation point. As the flow expands beyond 2×10^{-4} m from the stagnation point, the thermal gradients decrease near the wall causing the slope of the OPL to decrease. However the slopes of each OPL profile are not the same. At Mach 11,

13, and 15, the slope at 8×10^{-5} m from the edge of the window is steeper than in the region closer to the aftbody and increases with Mach number. Nearer to the aftbody or at 0.0016 m from the edge of the window, the slopes are approximately 50% less than in the stagnation region and decrease with increasing Mach number (see Fig. 4.18). The slopes decrease with distance from the stagnation point and are functions of freestream Mach number (or degree of dissociation). The difference

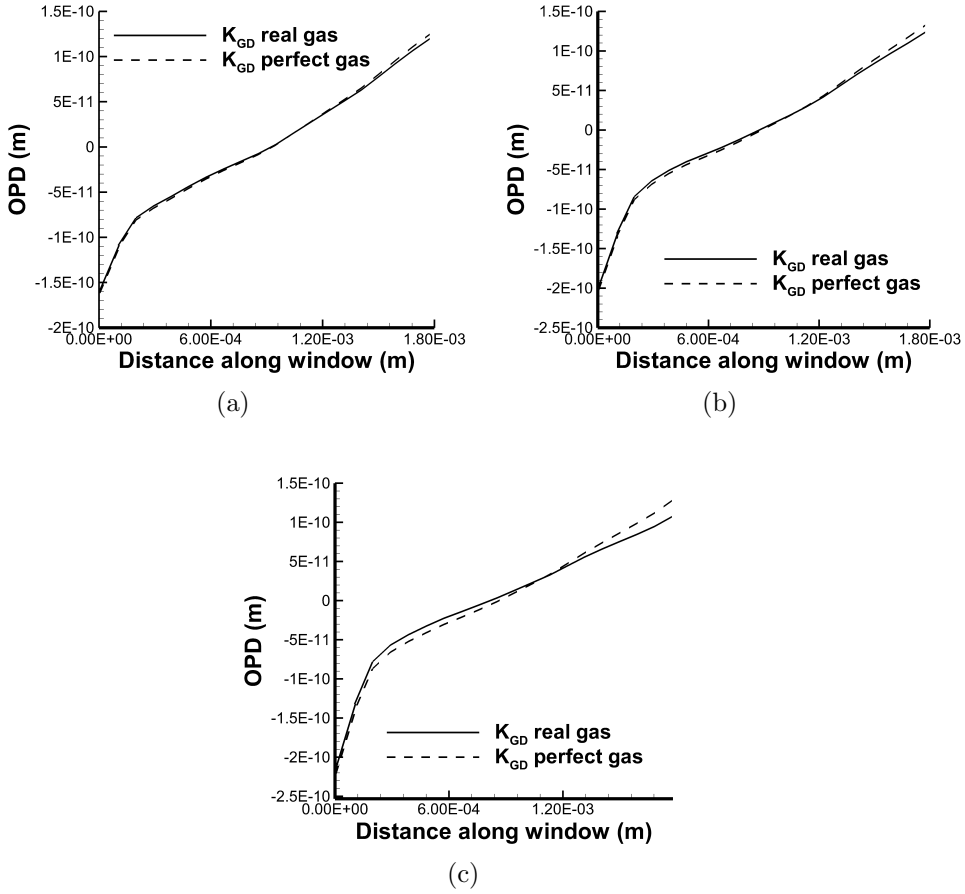

Figure 4.19: OPD in the red zone (Fig. 1) for (a.) Mach 11, (b.) Mach 13, and (c.) Mach 15.

between the OPLs including real gas effects and those that do not is higher with increasing Mach number. The average OPLs with real gas effects are larger than the average OPLs that use a (perfect gas) air Gladstone-Dale constant for the Mach 11, 13, and 15 flows. This is due to the dominant effect of atomic species concentration

on the Gladstone-Dale constants, as discussed earlier in sections 4.3.1 and 4.3.3.1.

Once the OPLs are obtained, the spatial average of the OPLs (across the sensor aperture) is subtracted from each OPL to obtain an OPD map. Figure 4.19 shows the OPD in the plane of the window for the stagnation region (denoted in red in Fig. 3.1) for the Mach 11, 13, and 15 flows. The results shown in Figure 4.19 illustrate the sensitivity of OPD prediction to the choice of K_{GD} (derived from perfect gas or real gas).

The OPD shows negligible difference for the Mach 11 flow, Fig. 4.19a, for the choice of K_{GD} considered in the study. For Mach 13 and 15 flows, Figs. 4.19b and c, the initial rise in the slope shows very little sensitivity to the different K_{GD}s but as all slopes decreases (2×10^{-4} m away from the stagnation point), the OPD based on the K_{GD} with real gas effects is higher than that based on (perfect gas) air. Further along the body, there is a cross-over (at approximately 1×10^{-3} m from the stagnation point), and the OPD based on the K_{GD} with real gas effects is lower than that based on K_{GD} for (perfect gas) air. The magnitude of the maximum difference between the OPDs found with the (perfect gas) air assumption and those found with the real gas models increases with Mach number.

Much like the slope of the OPL, which generally becomes lower with increasing distance from the stagnation point, the OPD gradients (for both perfect and real gas) decrease with increasing distance from the stagnation point, Fig. 4.19. The gradient of the OPD considering real gas effects is further reduced due to the decreases in atomic species away from the stagnation point. We may conclude that the pattern of optical distortion is altered by the inclusion of real gas effects. Figure 4.20a shows the OPL for Mach 15 flow in the expansion region denoted in green in Fig. 3.1. It may be noted that since the boundary layer lacks strong thermal gradients, we do not see the initial steep gradient in the OPL and OPD (as was observed in the stagnation region). The OPL considering real gas effects is approximately parallel to and less than 1%

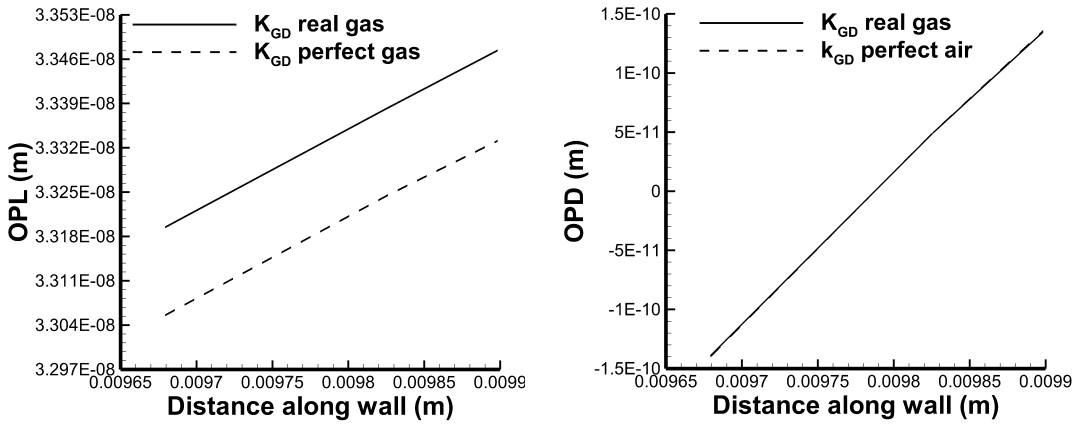

(a) (b)

Figure 4.20: OPL (a.) and OPD (b.) profiles for the Mach 15 flow in the aftbody region.

larger than the (perfect gas) air OPL. As a consequence of these minor differences in OPL, there is negligible difference in the OPD between the real and perfect gas case shown in Fig. 4.20b.

4.3.4 Effects of Diffusion on Optical Properties

In hypersonic flows with real gas effects, there are molecular and atomic species of different molecular weights diffusing at different rates relative to the mean flow gradients. One may note that there is strong uncertainty in modeling the diffusion effects in hypersonic nonequilibrium flows. We study the effect of mass diffusion on the optical properties presented in this section. We show the results in the stagnation region as this is where the concentration gradients are the highest. Figure 3.29 shows the effect of diffusion for the Mach 15 case. Figure 3.29a shows mass fractions along the stagnation streamline for N_2, N, O_2, O, N and NO with and without diffusion. Referring to Table 2.2 (Gladstone-Dale constants for the species at a wavelength of approximately $0.5\mu m$ in the temperature range 5000-9000 K), we see that the Gladstone-Dale constant is the highest for N. From Fig. 3.29a, the mass fraction for N_2 with diffusion is lower at the wall than without diffusion. Conversely, the mass

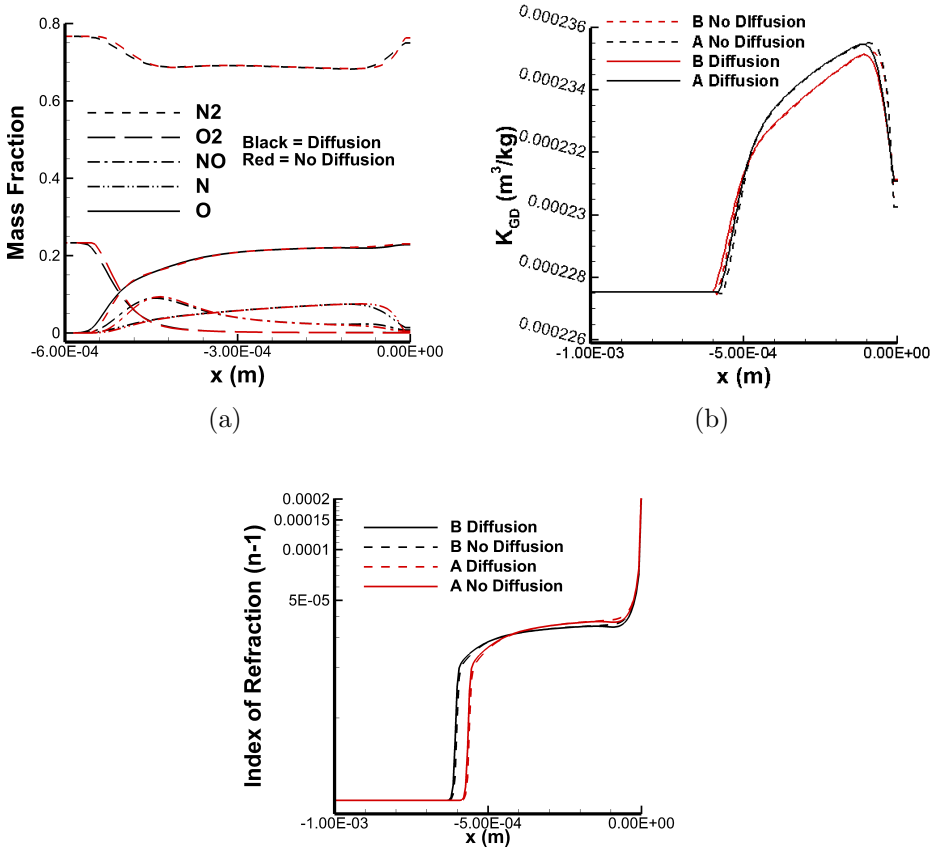

Figure 4.21: Effects of diffusion along the stagnation streamline for Mach 15 flow on (a.) mass fraction (Zone A), (b.) Gladstone-Dale constant profiles, and (c.) modified index of refraction.

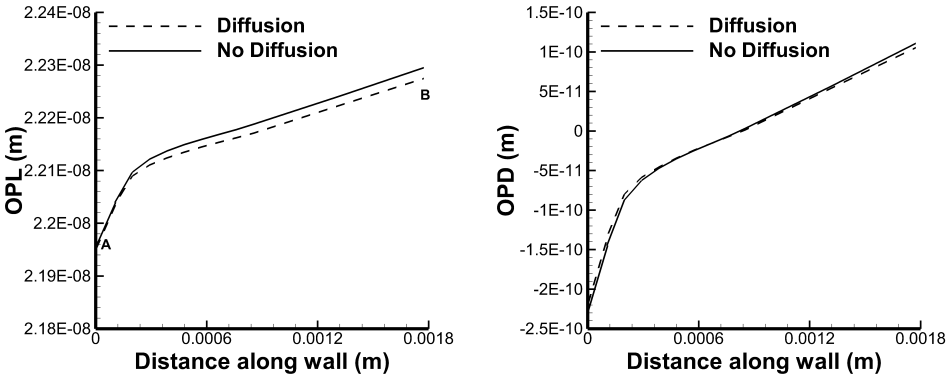

(a) (b)

Figure 4.22: OPL (a.) and OPD (b.) with and without diffusion.

fraction for N with diffusion is higher at the wall. The mass fraction of NO with diffusion is higher at the wall. Consequently, we see in Fig. 3.29b that K_{GD} is higher at the wall with effects of diffusion included, Fig. 3.29b. The contribution of the mass fractions of O_2 and O to the K_{GD} at the wall are negligible.

Figure 3.29c shows profiles of the modified index of refraction, n-1 in this study, normal to the wall at locations marked as A and B in Fig. 4.22a. The diffusion effects have negligible influence on the index of refraction along a beam radiating normal to the body beginning at the stagnation point, location A. There is a similar negligible influence of the index of refraction at location B, or 0.0018 m along the body from the stagnation point. One may note that even though the K_{GD} at the wall is higher with diffusion included, the index of refraction, which is a product of mass density and K_{GD}, shows negligible effect with and without diffusion.

Figure 4.22 shows the OPL distribution on the surface. The OPL in the stagnation region has negligible variation, with the differences between the profiles increasing with distance from the stagnation point, with a maximum difference of less than 1% at location B. Figure 4.22b shows the OPD distribution along the sensor window surface. The magnitude of the OPD is higher for the case without diffusion; however, these differences are also small.

4.4 Summary

A computational study was performed to assess the optical properties of flows experiencing thermochemical nonequilibrium. We considered flows with freestream Mach numbers of 11, 13, and 15 past a hemispherical cylinder. Signal distortion was simulated along the plane of two windows that are on the body (flush with the surface), one in the stagnation region and the other in the aftbody expansion region. The optical features considered were optical path length (OPL) and optical path difference (OPD), as obtained from index of refraction. The Gladstone-Dale relation was used to relate the index of refraction to flowfield quantities.

When compared to simulations performed utilizing a calorically perfect gas assumption, the simulations which included thermochemical nonequilibrium models produced larger optical path differences. These differences are small (approximately 2%) at Mach 11 but increase with increasing Mach number (5% at Mach 15).

At all Mach numbers considered, the real gas OPL increased due to the predominant effect of the dissociation of oxygen. Dissociated nitrogen had a lesser and additive affect at the higher Mach numbers. Production of NO had little effect on optical distortion in the five species air model considered. It is concluded that the accuracy of aero-optical properties depends on accurately predicting the dissociation of oxygen molecules. Furthermore, since dissociation is related to internal energy, vibrational energy and consequently accuracy of the vibrational relaxation rates also affect optical distortion.

While inclusion of diffusion did alter the Gladstone-Dale constants, the alteration had a minimal effect on optical distortion; the OPD predicted when excluding diffusion was less than 0.1% greater than the distortion predicted when including diffusion.

CHAPTER V

Effects of Modeling Turbulence

5.1 Introduction

In Chapter II, the numerical approaches that allow for prediction of optical abberations in various classes of flow are introduced. In the present chapter those methods are applied to turbulent flows over flat plates. This chapter first introduces a numerical procedure used to induce turbulence and bypass natural transition. The bypass method will be presented preceding discussion of the test sets because all cases in Chapter IV utilize this numerical scheme. Chapter IV will then continue to present the two test cases, each labeled with their respective freestream Mach number.

The first case documented in this study consists of three flows at Mach 6 over a flat plate. These simulation are performed using implicit large eddy simulation (ILES), the Menter SST closure to the Reynolds averaged Navier-Stokes (RANS) equations, and laminar flow solutions. These simulations make it possible to quantitatively compare the effects of turbulence resolution and modeling on optical aberrations. The conclusions of this study will provide the information necessary to decide if incurring the additional computational cost associated with ILES is required for aero-optic applications. This study assumes ILES provides the more accurate description of the flow field and resulting effects on aero-optics. In this case, thermochemical nonequilibrium effects are not included.

The second case discussed in this chapter consists of two turbulent Mach 4 flows over a flat plate. Both computations are performed using ILES. While Mach 4 is not in the traditional hypersonic regime, flow conditions are such that they induce nonequilibrium and turbulent effects. The freestream flow parameters are representative of post-shock conditions for a 21 degree wedge flying at Mach 20 at 20 km in altitude [17]. The two cases in this test set differ in their inclusion of thermochemical nonequilibrium models (one case is treated as a real gas and the other is treated as a calorically perfect gas). The perfect gas case provides a comparison for the real gas simulation. The results from this test set will highlight the role of thermochemical nonequilibrium in aero-optical assessments of high enthalpy, turbulent flows.

For both case sets, the optical calculations are performed on each flowfield and any pertinent differences are quantified. The optical calculations are carried out as a post-processing step for all cases using the Gladstone-Dale relation. During this post-processing routine, a separate grid is created for the optical assessments and the appropriate integrations are conducted along the signal propagation path.

Each case is presented in the following manner: first, the simulation conditions and geometry are discussed with particular emphasis placed on mesh generation; next, general descriptions of all flowfields are presented; the optical results are then presented for each case in their respective sections. Each case concludes by presenting a summary with the relevant conclusions that are discerned from the studies.

5.2 Bypass Transition

The turbulent simulations detailed in this chapter are performed using US3D, as described in Chapter II. The simulations are run using an implicit filter. The implicit filter utilizes high order finite volume inviscid flux splitting schemes to capture the physics in the turbulent inertial range while reducing the number of grid points required to do so. An implicit LES method is not intended to resolve the smallest

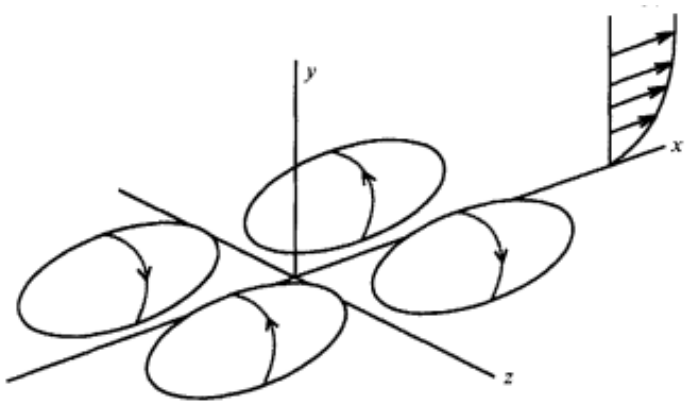

Figure 5.1: Counter-rotating vortices used to induce turbulence [10]

flow features. ILES relies on the numerical dissipation that is intrinsic to the flux splitting scheme to dissipate all small scale flow features; all vortical flow features that are not resolved by the mesh are numerically dissipated [19]. This level of resolution is acceptable for an optical study because the most optically important features are approximately the size of the boundary layer [57].

In the present study, turbulence on the flat plate is induced by imposing alternating pairs of counter-rotating vortices. These disturbances are imposed on a laminar boundary layer at an inflow plane, and they create both down and up-wash flow features. The numerics employed here were originally developed to mimic the induction of turbulence in an experiment which used a moving membrane to produce localized vortices [10]. Figure 5.1 is representative of the counter-rotating vortices that are introduced in the span-wise direction to the laminar solution. These vortical features are developed from the stream function, Eqn.(5.1).

$$\Psi = AU_\infty \overline{x}\overline{y}^3\overline{z}\exp\left(-\overline{x}^2 - \overline{y}^2 - \overline{z}^2\right) \tag{5.1}$$

where the velocity disturbances are described in Eqn.(5.2):

$$u' = 0 \quad v' = -\frac{\partial \Psi}{\partial z} \quad w' = \frac{\partial \Psi}{\partial y} \tag{5.2}$$

$\overline{x}, \overline{y}, \overline{z}$ are coordinates scaled with the characteristic lengths of the vortex disturbance as described in [53], and A is the strength of the vortices. A is a fraction of freestream velocity and is chosen to be approximately 0.1 for the cases described in this study.

The laminar solutions, both real and perfect, are produced by the NASA Data Parallel-Line Relaxation (DPLR) code [62], which has been used successfully to compute both real, and perfect gas, laminar boundary layers for instability and transition modeling [25].

5.3 Mach 6 Cases

The Mach 6 flat plate cases are utilized to quantify the differences in optical distortion that are produced by varying levels of turbulence resolution. An implicit large eddy simulation, a RANS simulation, and a laminar simulation are presented. These cases are run without nonequilibrium models in order to discern the effects of turbulence alone on optical aberrations. Section 5.3 is further divided into three sections. Subsection 6.3 describes the geometry and flow conditions, subsection 5.3.2 presents the numerical results, and subsection 5.3.3 summarizes the conclusions of the study.

5.3.1 Details of the Numerical Simulation

The simulation conditions are presented in two sections. Section 5.3.2.1 discusses the simulation parameters for each portion of the study. Section 5.3.1.2 discusses the grids used for this analysis.

5.3.1.1 Flow Parameters

The Mach 6 cases simulate flow over a flat plate. The flat plate length for all simulations is 0.5625 m. For the large eddy simulation only, the bypass transition is imposed on the laminar boundary layer (from the converged DPLR solution) at

0.0375 m from the leading edge. The laminar and RANS solutions are corrected for this 0.0375 meter offset to enable comparison at the appropriate boundary layer height. These cases are run assuming a perfect gas in order to isolate the effects of the varying turbulence approaches; see Table 5.1 for the perfect air freestream conditions. These conditions are chosen to replicate those published in Ref. [53]. The unit Reynolds number for these simulations is $1.7 \times 10^7\ m^{-1}$. The turbulent unit

Table 5.1: Turbulence Study Flow Parameters

Parameter	Value
M_∞	5.97
ρ_∞	0.144 kg/m^3
T_∞	254 K
P_∞	10.5 kPa

Reynolds number is $4.0 \times 10^5\ m^{-1}$, as calculated from the ILES turbulent kinetic energy. The isothermal wall is set to 300 K.

5.3.1.2 Mesh Structure

The initial laminar and RANS simulations are run on progressively denser meshes until changes in the solution cease. The resulting mesh sizes are presented in nodal dimensions and are shown in Table 5.2.

The ILES mesh is created to have $\Delta x+ = 27.38$, a $\Delta z+ = 32.8$, and a $\Delta y+ = 0.2$. These values represent a well resolved large eddy turbulent simulation [19].

Table 5.2: Flat plate Mesh Parameters

Simulation	Mesh Size	Total Computational Time
Laminar	100×64	1.93 Hours
Menter SST	119×100	2.47 Hours
ILES	$5389 \times 256 \times 181$	$864,000$ Hours

The initial mesh for the laminar study has a Reynolds number of one in the cells adjacent to the wall. The initial Menter SST grid is created to ensure that the $\Delta y+$

in the cells adjacent to the walls does not exceed one. For both the laminar and the Menter SST simulations, meshes are created in two dimensions.

ILES, however, requires a three-dimensional mesh to obtain physical results. Turbulence is an inherently three dimensional phenomenon and detailed ILES modeling requires simulations to be performed in the full three dimensions. For ILES, the mesh is divided horizontally into three regions. Figure 5.2 presents these divisions, and they are denoted in red. The first region nearest the wall consists of a $\Delta y+ = 0.2$

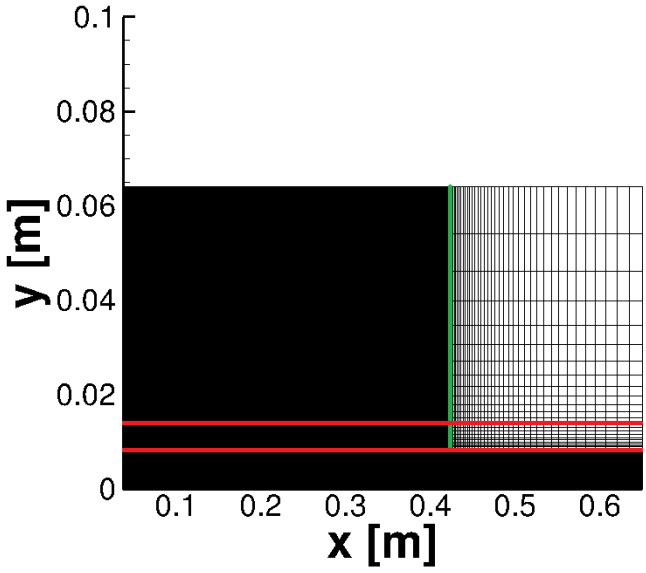

Figure 5.2: Mesh Structure for the Mach 6 Flat Plate

stretching to a $\Delta y+ = 20$. The second region has equal spacing and extends to the point at which 1.4 times the expected boundary layer at the exit plane is reached. The third region is then stretched to the top boundary. The mesh is further divided vertically into two regions, and is denoted in green in Fig. 5.2. The first is the region of computational interest and has uniform spacing. The second region is stretched to the outflow boundary in an effort to dampen out fluctuations in this region.

Table 5.2 also provides the total computational time that elapsed for each simulation. The laminar and RANS solution took a similar amount of time when compared to ILES. ILES took approximately 10^6 times longer to run and capture relevant statis-

tics.

5.3.2 Results

The results of this study are presented in two sections. The first section details the general flowfield for each simulation, with particular attention paid to the flow features which affect optical distortion. The second presents the optical distortion generated by these flowfields.

5.3.2.1 Flowfield Results

The flow for the Mach 6 turbulence study is typical of a high speed, relatively high Reynolds number, flat plate case. It consists of a weak oblique shock at the leading

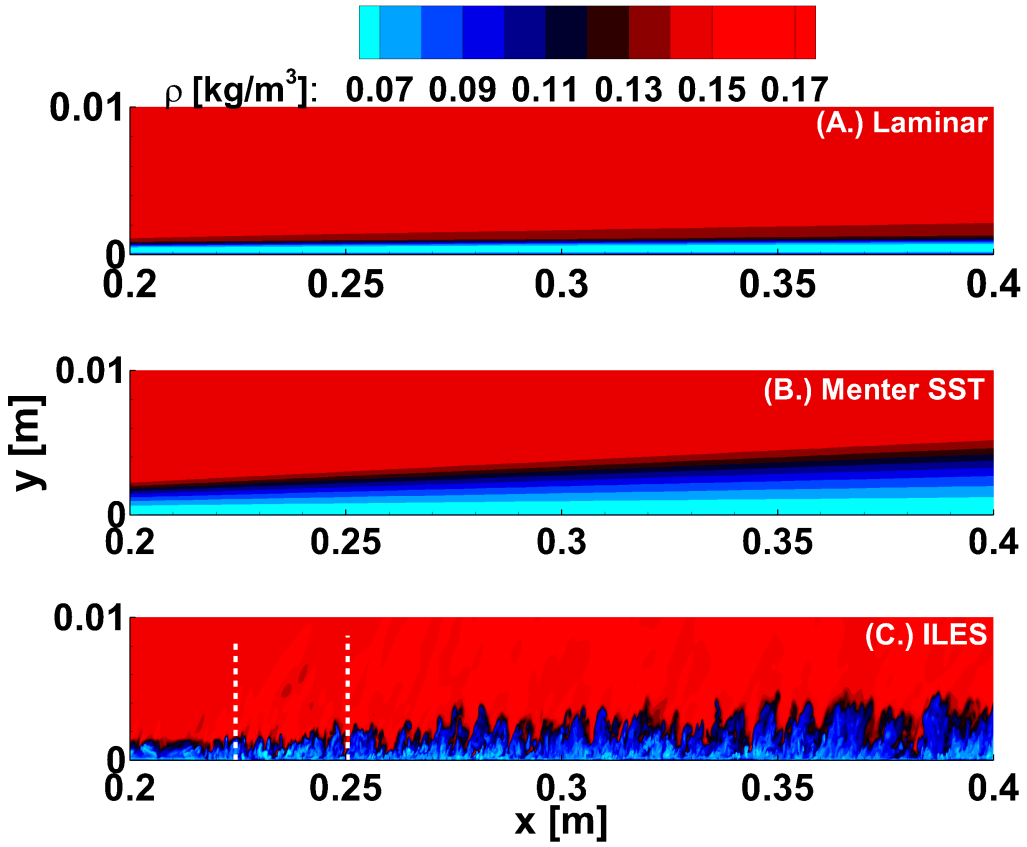

Figure 5.3: Flat plate density contours (ILES t= 0.25 ms)

edge of the plate and a thin boundary layer confined to the area near the wall.

Figure 5.3 presents density contours for (A.) the laminar simulation, (B.) the Menter SST simulation, and (C.) the ILES simulation. The ILES data in this study are taken at z=0.0129 meters and at time = 0.25 ms. Note that these figures do not show the entire computational domain; only the portion of the ILES flow over the flat plate that is in turbulent equilibrium is shown. In this figure, we see that the laminar boundary layer is thin and consists of rather parallel layers. The Menter solution produces a thicker, but still uniformly varying, layer. The fluctuations are only present in the ILES predicted data. The ILES fluctuations extend much further into the free stream than any of the wall effects produced in the laminar and RANS simulations.

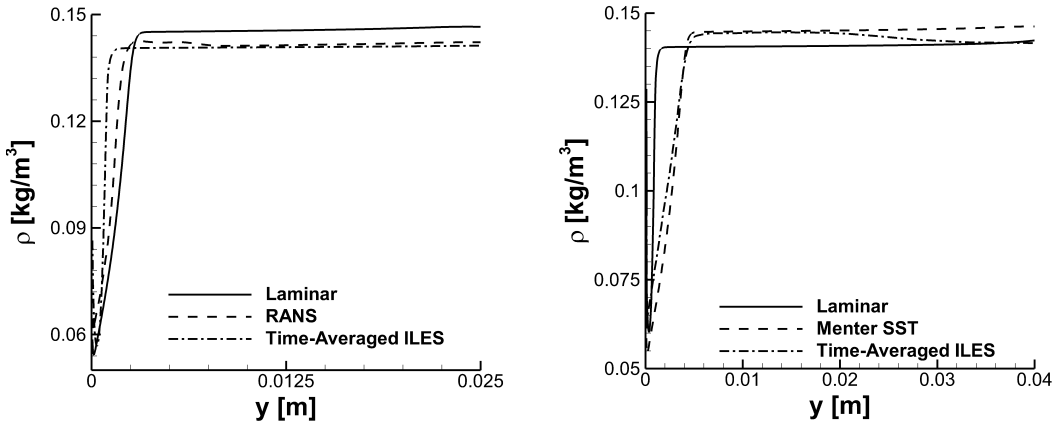

Figure 5.4: Density curves at (a.) x= 0.23 meters and (b.) x= 0.33 meters

To obtain and observe the mean flow behavior of the ILES solution, the simulation is run until mean flow statistics converged (as measured by the residual produced from progressive averaging of mean flow quantities). The average density profile is then compared to the RANS and laminar profiles (the RANS case is run in a fully turbulent manner and no transition calculations are included) at two differing x locations; see Fig. 5.4. Figure 5.4 shows density profiles extracted at x=0.23 m and x=0.33 m,

respectively. These locations are chosen such that they are at the extrema of the region in turbulent equilibrium. When comparing the three density profiles, we see that the boundary layer is thinnest for the laminar case and that the boundary layer produced by the RANS solution is much closer in thickness to that produced by the ILES. The Menter SST and time averaged ILES curves predict approximately the same boundary layer height and density value at the wall. The laminar solution does not accurately predict either property. Some disagreements between the ILES and Menter SST data sets appear as the oblique shock created from the leading edge of the plate is approached.

5.3.2.2 Optical Results

Data from a zone ranging from x = 0.23 meters to x = 0.25 meters is extracted and analyzed for optical properties; this zone is shown on Fig. 5.3 (C.) as the area between the two white lines. The OPD is calculated for this zone, assuming the beam propagates normal to the wall surface. The density variation between successive x locations dictates optical distortion, as described with the Gladstone-Dale relation and Eqns. (2.47)-(2.48). Figure 5.5 shows the density profiles at x=0.23 m, x=0.235 m, and x=0.24 m. Note the significant variation in shape between the various locations for the ILES simulation. The laminar and Menter SST profiles are almost identical to one another, experiencing variation of less than 1%.

Figure 5.6 presents the standard deviation in the density profiles across the area of optical interest. Standard deviation is a statistical quantity that describes the spread of the data; low standard deviation values indicate that the data is tightly clustered about the mean (there is not significant variation in that data set). For the Mach 4 flows, low standard deviation values for density indicate that the density does not vary significantly between successive x locations in the flow. We would expect to see low standard deviations for the laminar and Menter SST flow, and much higher values

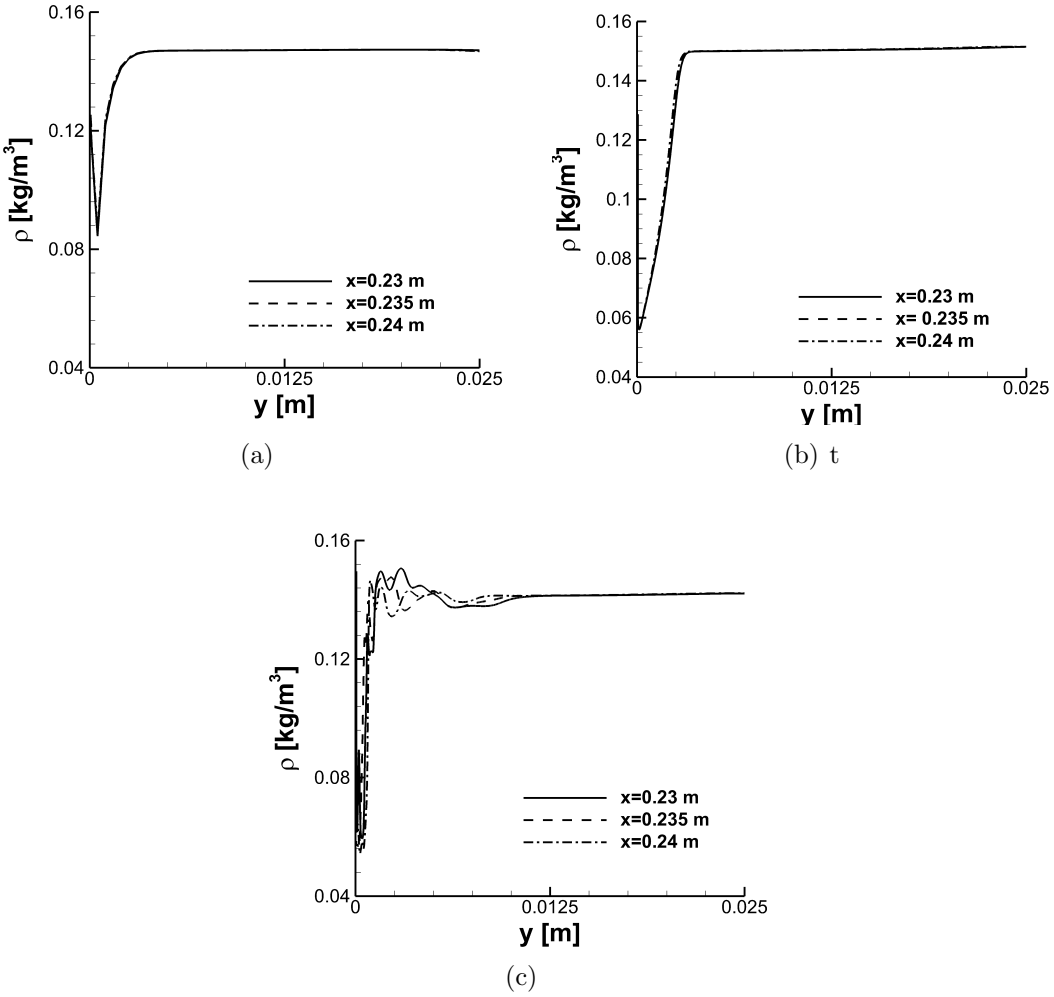

Figure 5.5: Flat plate density profiles for (a.) laminar simulation, (b.) RANS, and (c.) ILES (t=0.25 ms) for Optical Zone

for the ILES flow. In Fig. 5.6 we can see the hypothesized patterns are exhibited. The standard deviation is highest for all flows at a y location within the boundary layer. The ILES peaks at the highest value which is approximately 29 times larger than the peak deviation produced by the Menter SST simulation. The laminar simulation has the lowest peak in standard deviation. Figure 5.6 shows only the variation in the growing boundary layer. The freestream data is not included since variation in this portion of the flow is essentially zero for all simulation types. The conclusion drawn from Fig.5.6 has optical implications which can be seen in Fig.5.7 that shows the

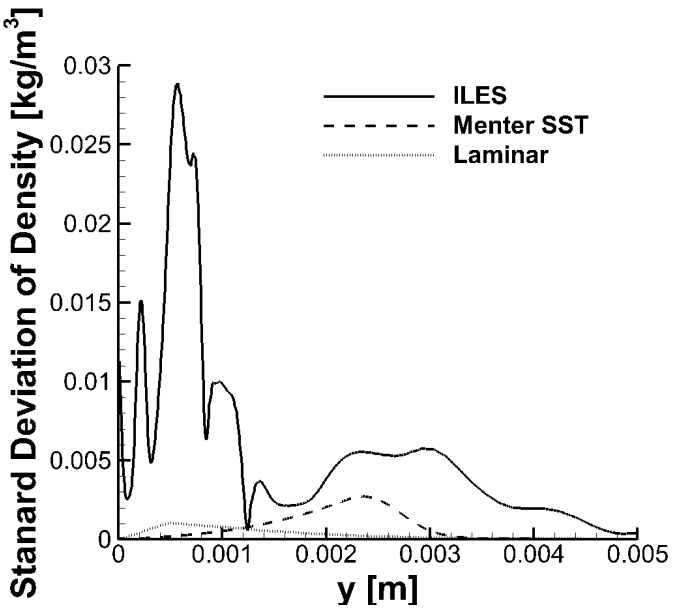

Figure 5.6: The standard deviation in density for ILES, Menter SST, and laminar flows

optical distortion of the flow over the plate from x = 0.23 m to x = 0.25 m. Variations in density cause optical distortions in all gas flows. It is, therefore, unsurprising that ILES produces the largest OPDs. The larger OPDs obtained from the ILES solution stem from this models ability to capture fluctuating densities. While the Menter SST simulation produces a similar boundary layer thicknesses and mean flow quantities, it is unable to provide fluctuating values. Because of the inability of RANS to capture fluctuating data, the associated OPD profile is not significantly dissimilar to the laminar OPD profile. Both the Menter SST and laminar flow fields produce linear OPDs that are, on average, two orders of magnitude lower than the non-linear OPDs predicted from ILES. Furthermore, it is anticipated that downstream, where fluctuations are larger, these OPDs could be more disparate. The optical data for the zone is taken in a manner to ensure that all relevant flow features are captured; each data set is taken from the wall extending normal into the freestream.

The resolved turbulent data shown in Figs.5.3-5.7 are taken at a plane where z=0.0129 meters and at time t = 0.25 ms. Additional data sets are collected at other

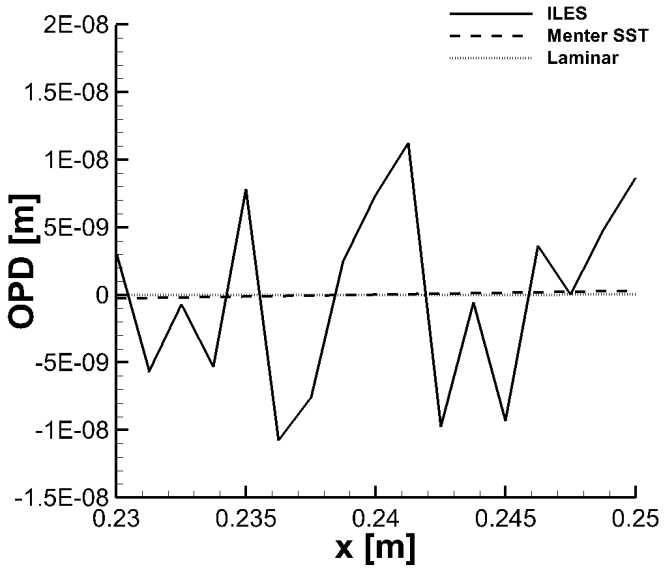

Figure 5.7: OPD profiles for the flat plate flow

z-planes, and the conclusions drawn from each are the same. Figure 5.8a shows optical distortion predicted from several z planes. Because of the similarities between the planes, further data from other streamwise planes is not shown. Data are also taken at

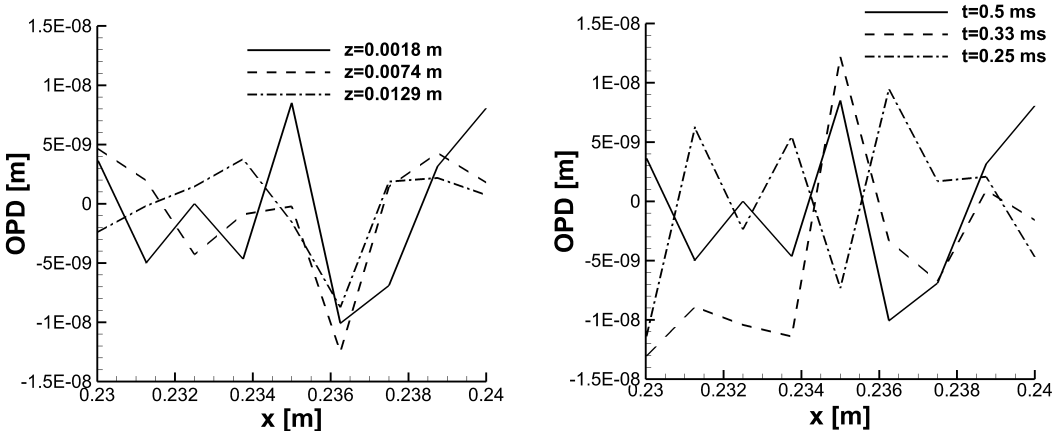

(a) (b)

Figure 5.8: Profiles of OPD obtained from the ILES flow simulation: (a.) in 3 different streamwise planes (t=0.25 ms); (b.) at 3 different time steps (z=0.0129 m)

different points in time to assess time independence of the conclusions drawn from this

study. Figure 5.8b shows the optical distortions at different times, and the distortion produced at all times is similar. Although the locations of the peaks and troughs in OPD have shifted, the magnitude of the fluctuations appears to be independent of time.

5.3.3 Summary

The Mach 6 flat plate simulations were conducted to determine the effects of varying levels of turbulence resolution. This case set showed that both laminar and Menter SST simulations produced relatively small, linear OPD profiles. The ILES solution produced non-linear OPD profiles with an average that is two orders of magnitude larger than the laminar and Menter SST values.

ILES is the only method presented that has the ability to produce turbulent fluctuating quantities. ILES is necessary to capture an accurate description of optical distortion of a fluctuating flowfield; the simpler Menter SST calculation did not produce OPDs close to those generated by ILES. Furthermore, in the studies presented in this thesis, inclusion of resolved turbulence has a larger effect on optical distortion calculations than inclusion of thermochemical nonequilibrium; see Chapter IV. It is important to note that these studies did not include both turbulence and thermochemical non-equilibrium in the same simulation. Turbulent flow in thermochemical nonequilbrium may have an important affect on aero-optical analysis and is the topic of Section 5.4.

5.4 Mach 4 Cases

The Mach 4 test cases are run to determine the role thermochemical nonequilibrium has in the assessment of the effects of high speed, turbulent boundary layers on aero-optics. Both perfect and real gas simulations are presented. The perfect gas solution is provided for comparison. Section 5.4 is divided into three subsections: the

first portion discusses numerical conditions; the numerical results are presented next; and lastly, a summary is presented.

5.4.1 Details of the Numerical Simulation

The numerical simulation conditions are further divided into two sections. Section 5.4.1.1 discusses the simulation parameters for each portion of the study. Section 5.4.1.2 discusses the computational meshes used in this analysis.

5.4.1.1 Flow Parameters

The simulations in this study are conducted on a turbulent Mach 4 flow over a flat plate. The flat plate extends in the streamwise direction to approximately 0.64 meters. The cases, both real and perfect gases, are run with the free stream conditions described in Table 5.3. An adiabatic wall condition is utilized. The free

Table 5.3: Mach 4 Test Case Flow Parameters

Parameter	Value
M_∞	4
ρ_∞	0.5 kg/m^3
T_∞	5000 K
$Y_{O2}/Y_{N2}/Y_{NO}/Y_N/Y_O$	0.0166/0.616/0.0501/0.00890/0.309

stream mass fractions are set to their equilibrium values at 5000 K. These conditions are representative of the post shock conditions for a 21 degree wedge flying at Mach 20 at 20 km in altitude. Free stream conditions are chosen as such to allow qualitative comparisons to the readily available data [17].

5.4.1.2 Mesh Structure

The ILES mesh is created to have $\Delta x+ = 15$, $\Delta z+ = 25$, and $\Delta y+ = 0.14$. These values are deemed sufficiently refined for an ILES simulation following guidelines outlined in Ref. [19]. Much like the ILES in the Mach 4 cases, the mesh is

three-dimensional to obtain physical results since turbulence is an inherently three dimensional phenomena. The size of the domain in the Cartesian z dimension (spanwise) is 0.1475 meters.

In the same way as the Mach 6 case, the mesh is divided horizontally into three regions (denoted in red); see Fig. 5.2. The first consists of a $\Delta y+ = 0.14$ at the wall stretching to a $\Delta y+ = 28$. The second region has equal spacing and extends to point at which 1.4 times the expected boundary layer at the exit plane is reached. The third region is then stretched to the top boundary. The grid is also split into two vertical regions. The first consists on uniform spacing and begins at the front of the plate and extends to x= 0.4 meters. After x=0.4 meters the grid is stretched to x=0.6 meters.

5.4.2 Results

The results are divided into two sections. The first section presents a general assessment of the Mach 4 perfect and real gas flows over a flat plate. This section emphasizes features that are important to optical assessments. The influence of these features on optical distortion is presented in the second section. All data unless otherwise noted are taken at t=0.5 ms.

5.4.2.1 Flowfield Results

In order to determine the validity of the simulations presented here, Fig. 5.9 is created and assessed. The non-dimensional velocity boundary layer profile is plotted and compared to the theoretical boundary layer solution [54]. Originally derived by von Karman, the law of the wall assumes that the turbulence near the wall can be described in variables pertaining to that wall only. It further assumes that non-dimensionalized velocity is only a function of non-dimensionalized distance from the wall [54]. The velocity and distance from the wall (Cartesian y) are non-

dimensionalized, as illustrated in Eqn.(5.3).

$$y+ = \frac{yu_\tau}{\nu} \quad u_\tau = \sqrt{\frac{\tau_w}{\rho}} \quad u^+ = u/u_\tau \tag{5.3}$$

where τ_w is shear stress at the wall. As can be seen in Fig.5.9, the solutions produced by the real gas (bottom) and perfect gas (top) are in agreement with the trends of the theoretical curves. The differences that are present between the real gas velocity

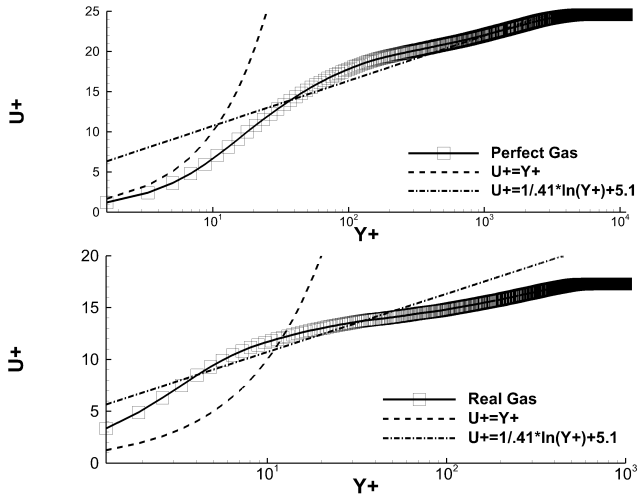

Figure 5.9: Velocity profiles for perfect and real gas compared to theoretical curves

profile and theory can be attributed to the derivation of the law of the wall which considered neither compression nor nonequilibrium effects.

To further assure that appropriate data are acquired for optical calculations, progressive averages are monitored for the conserved variables. A plateau in these values is indicative of the onset of equilibrium turbulence. Figure 5.10 shows the progressive average of the turbulent kinetic energy (TKE) for the perfect gas and real gas simulations, respectively, at a location near the wall (in dimensional coordinates x=0.35 meters, y=0.001 meters, and z=0.0077 meters). The progressive averages are collected at multiple locations, and the same temporal evolutions are obtained. At approximately 4000 samples and 100 samples for the perfect gas and real gas simu-

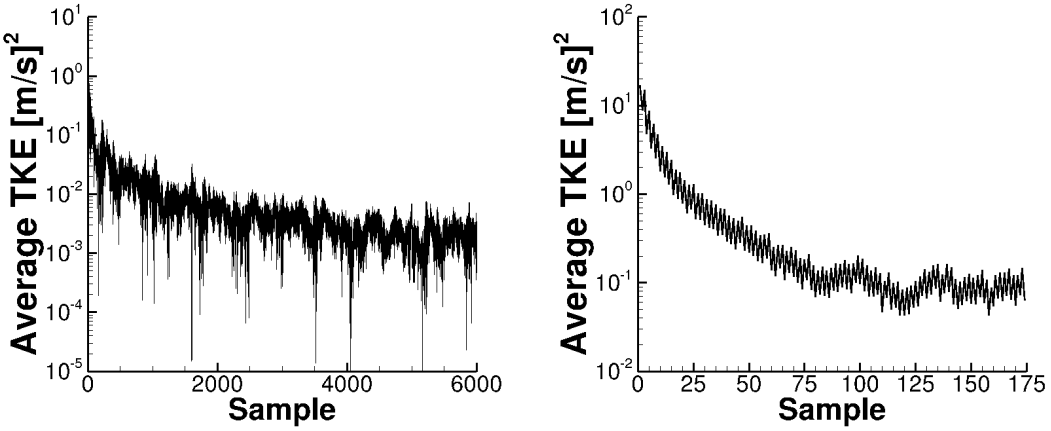

(a) (b)

Figure 5.10: Progressive average of TKE for (a.) Perfect Gas and (b.) Real Gas

lations, respectively, the progressive averages plateau which indicates that the initial transients in the flow have diminished. Due to the nature of progressive averages, this data is taken over multiple times (not simply at 0.5 ms). Once the simulations and temporal data collection methods are validated, it is possible to analyze the flowfields produced with each simulation method.

Figure 5.11 presents the temperature profiles of (A.) the perfect gas flow and (B.) the real gas flow for Mach 4 flow over the flat plate. The data is extracted from a plane at z=0.077 m. Both flows are characteristic of a high speed turbulent flow over a flat plate. There is a thin fluctuating boundary layer confined in the area near the wall. The temperature at the wall reaches approximately 18000 K in the perfect gas simulations and 7500 K in the real gas simulation. The resultant difference in temperature is caused by the inclusion of the high temperature effects. Endothermic reactions in the real gas flow consume energy that would otherwise be in the translational and rotational modes (as it is in the perfect gas flow). It should be noted that the entire computational domain is not shown in Fig.5.11; instead, the area in the fully turbulent regime (for the nonequilibrium simulation) is illustrated.

Figure 5.12 presents the density contours for the flow over the flat plate for the

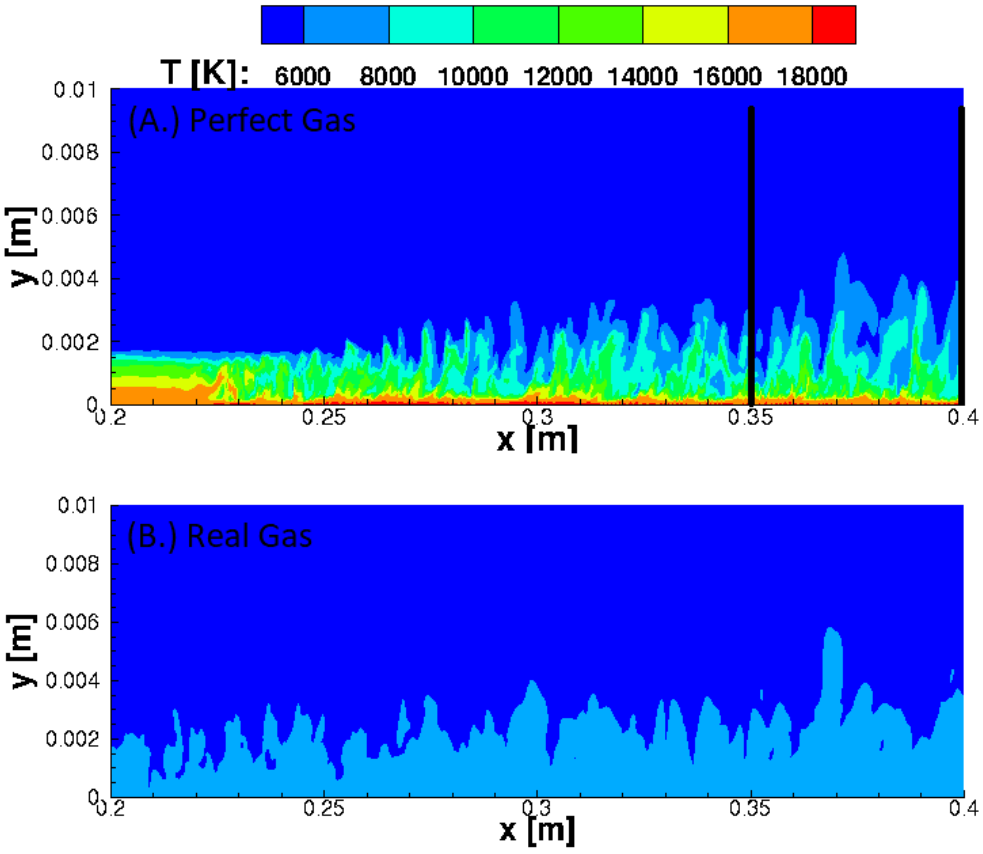

Figure 5.11: Temperature contours for (A.) perfect gas flow and (B.) real gas flow

perfect gas (A.) and the real gas (B.) simulations, respectively. Again, the figure illustrates that both flows are typical of a high speed, high Reynolds number flow over a flat plate. Due to the high temperature of the adiabatic wall, we see in Fig.5.12, that the density decreases near the wall. The decrease is more significant for the perfect gas flow, which is consistent with higher temperature and the equation of state.

Figure 5.13 presents the density extracted at x=0.35 meters (the beginning of the zone used for optical assessment). This figure shows only the boundary layer to emphasize differences between the perfect and real gas density profiles. Figure 5.13 illustrates the relatively low density at the wall for the higher temperature, perfect gas simulation. The density at the wall is 50% lower for the perfect gas case.

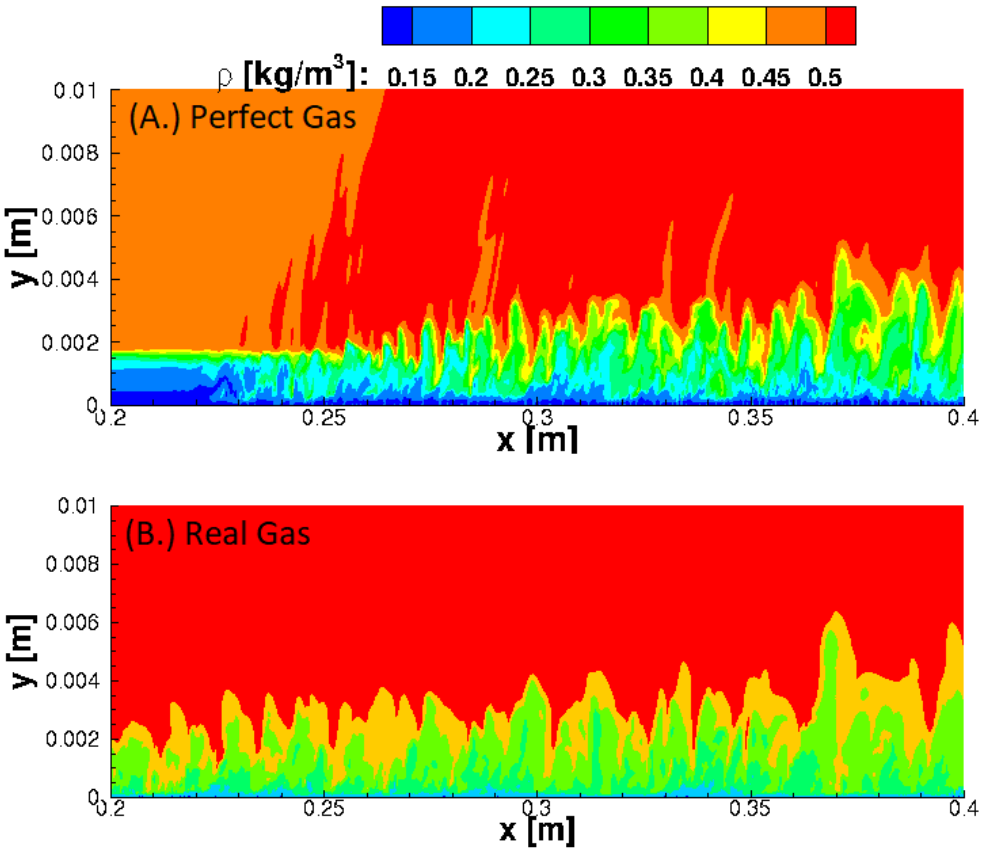

Figure 5.12: Density contours for (A.) Perfect Gas and (B.) Real Gas

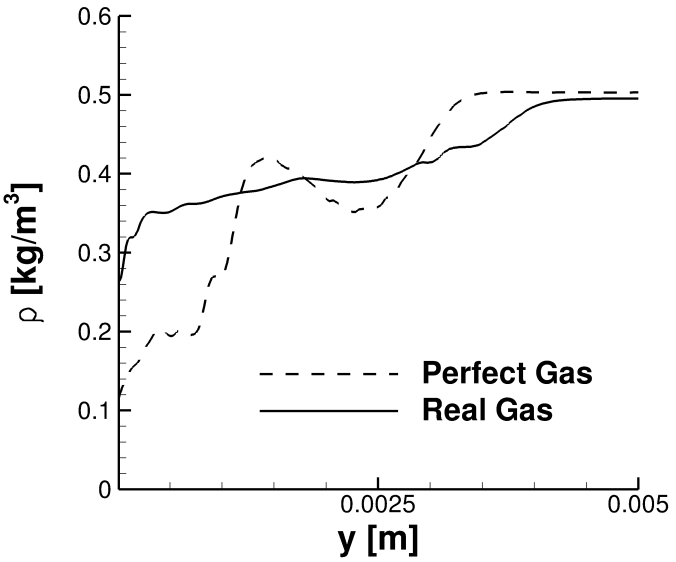

Figure 5.13: Density profile at x=0.35 m

We may also note that in Fig. 5.12, the real gas flow transitions to fully developed turbulence before the perfect gas flow transitions. The real gas trip mechanism, which is the same strength as the perfect gas trip, is imposed on a field that has multiple energy modes (translational, rotational, vibrational, and chemical). The total energy is divided amongst these energy modes in real gas case (unlike the perfect gas, which has only the translational and rotational modes which are in equilibrium). The higher translational energy of the perfect gas flow pushes the transition location downstream. Once the turbulence has fully developed, the density fluctuates within the boundary layer for both flows, as is expected with turbulent flows.

Further analysis of transition locations leads to Fig. 5.14 which shows the skin friction coefficient for the real and perfect gas simulations along the plate for a plane at z=0.077 meters. The skin friction upstream of x=0.2 m for the perfect gas and near x=0.01 m for the real gas is lower, which is indicative of laminar flow. At approximately x=0.2 m for the perfect gas and x=0.01 m for the nonequilibrium gas case, the skin friction coefficient increases sharply. This increase is indicative of transition to turbulence. The skin friction coefficient remains high throughout the

turbulent regime.

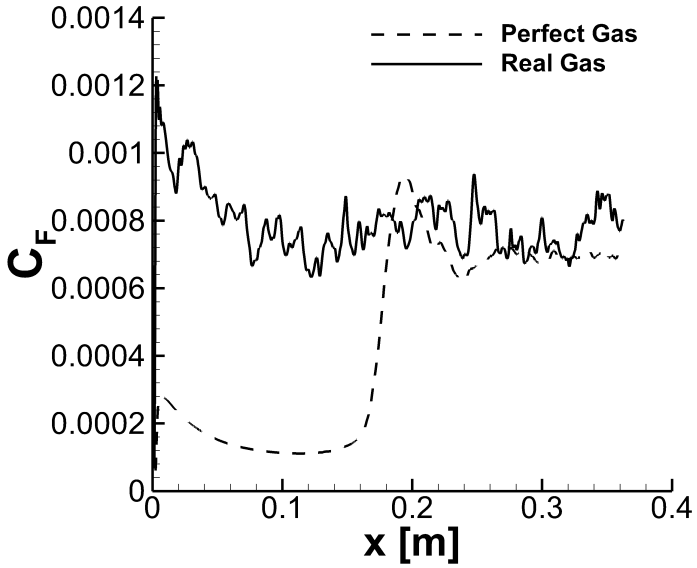

Figure 5.14: Skin friction coefficient

As previously mentioned, the nonequilibrium features of the real gas flow can drastically alter the mean properties associated with that flow (temperature at the wall, density at the wall, etc.). To understand the effects of real gas features, we analyze data at z=0.077 meters and x=0.35 meters. At the high temperatures present in the flow, the vibrational mode of energy becomes excited. While there are differences present in the vibrational and translational temperatures of the flow in this study, the differences are slight. Energy transfer into the vibrational mode does not play a large role in this particular flow. The lack of thermal nonequilibrium can be attributed to the high pressure in the flow (approximately 8 atm) which promotes energy exchanging collisions and consequently pushes the flow towards thermal equilibrium.

Nonequilibrium flow also often experiences energy being absorbed by the dissociation of the diatomic air species, N_2 and O_2. The result of this phenomenon is mass fraction profiles that vary throughout the computational domain. Figure 5.15 shows the mass fraction profiles of the 5 species in air taken from the real gas solution at x=0.35 meters and z=0.077 meters. Near the hot wall, the fraction of diatomic

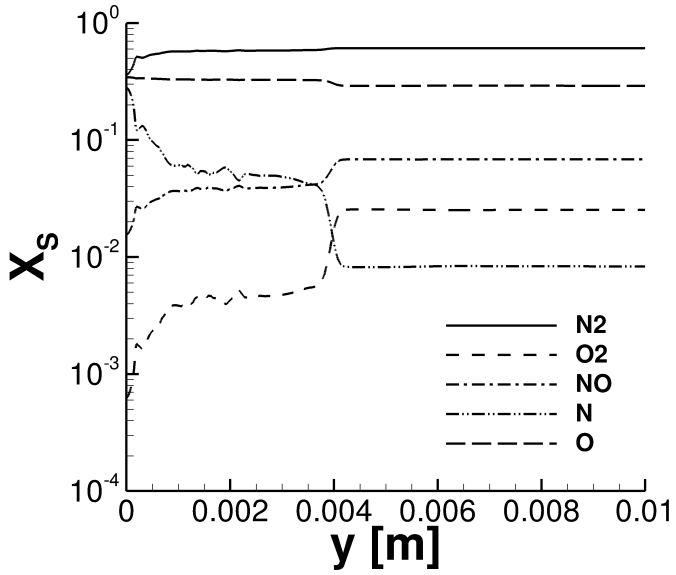

(1).png

Figure 5.15: Mass fraction profiles (z=0.0077 meters, x=0.35 meters)

nitrogen decreases as the wall is hot enough to promote significant nitrogen dissociation. Large changes in the concentration of diatomic and monatomic oxygen are not observed. The free stream temperature is already high enough to support oxygen dissociation. Near the wall the mass fraction of NO decreases; there is enough energy near the wall to support NO dissociation. These mass fractions modify the index of refraction.

In addition to affecting the mean flow properties, the various energy exchanges that occur in nonequilibrium flows have an effect on the turbulent fluctuations. Figure 5.16 shows the density fluctuations at x=0.35 meters and z=0.077 meters, which are up to 75% smaller than for the perfect gas simulation. This figure supports the conjecture that energy is taken from the turbulent kinetic energy and transferred into the thermal and chemical energy modes [39], [36]. Again, the density fluctuations are shown because of their large influence on the optical properties of the flow via the Gladstone-Dale relation. The more varied the density profiles are, the larger the variation in optical path lengths/differences there are (which are used to describe the phase shift for a beam traversing a flow field).

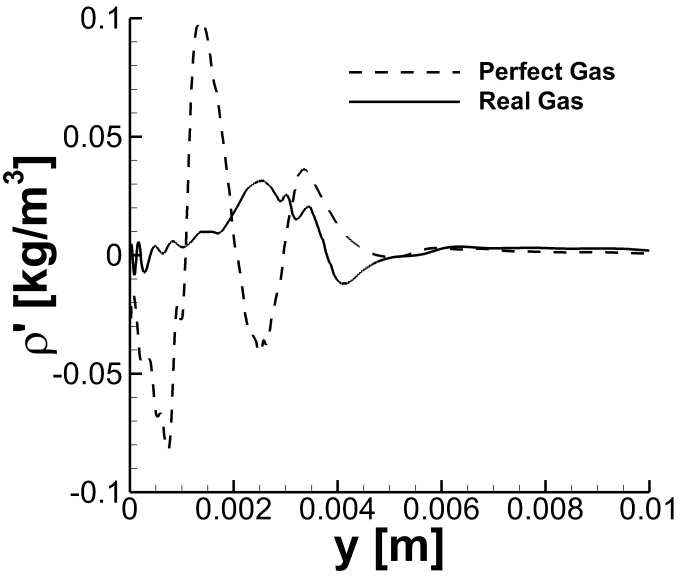

Figure 5.16: Density fluctuations of perfect and real gas (z=0.0077 m, x=0.35 m)

5.4.2.2 Optical Results

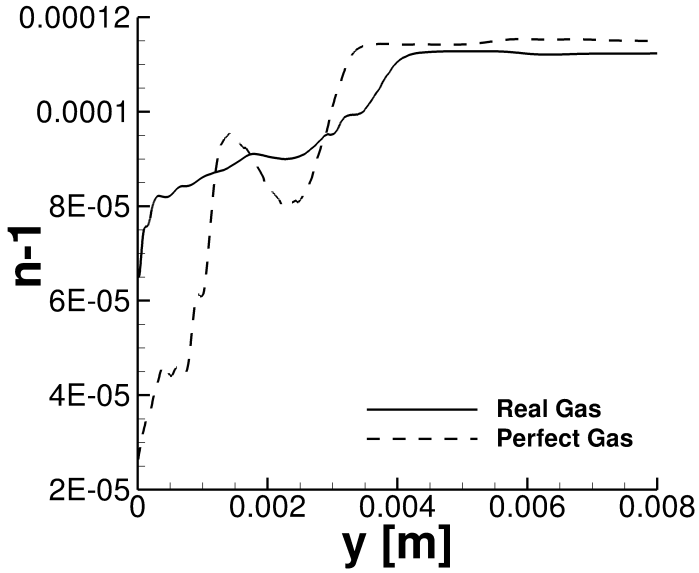

Figure 5.17: Index of refraction profile

When the Gladstone-Dale relation is applied to the perfect gas and real gas density profiles at x=0.35 meters and z=0.0077 meters, Fig.5.17 is obtained. It should be noted that for the perfect gas simulations, a single Gladstone-Dale constant is

utilized. A Gladstone-Dale profile is used for the nonequilibrium simulation, as the mass fractions vary throughout the field in the real gas simulation. The index of refraction largely follows the trends of the density profiles with minor modifications due to species concentrations (in the real gas flow); see Fig. 5.13. In fact, the percent difference between the real gas and perfect gas indices of refraction is 53% which is similar to the percent difference in the density at the wall (location of maximum difference).

Index of refraction profiles, as in Fig.5.17, are integrated, and the resulting OPDs are obtained. Figure 5.18 depicts the optical distortion calculated on a plane where z is equal to 0.077 meters and x ranges from 0.35 meters to 0.40 meters; see Fig.5.11 for area of optical interest. From this figure, we see optical path lengths vary more from the mean optical path length for the perfect gas simulation. This difference can be attributed to the larger fluctuations in density (see Fig.5.16) that are present in the perfect gas simulation. Although the Gladstone-Dale constant does fluctuate slightly due to the varying mass species in the real gas simulation, this is not the dominant contributor to optical distortion. The perfect gas OPD_{RMS} is 89% larger than the

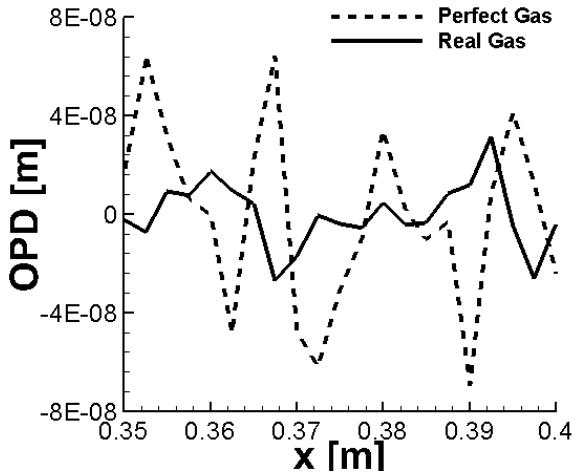

Figure 5.18: Optical path distortion

real gas OPD_{RMS} at the plane and time (z=0.077 m and t=0.5 ms) reflecting the

greater variation in the optical lengths for the perfect gas case. Similar results are obtained at other times and z locations; though the positions of the peaks and troughs shift, the relative RMS magnitude of the fluctuations remains approximately constant at each location and is independent of time.

5.4.3 Summary

A flat plate simulation was conducted to determine the effects of resolved high enthalpy turbulence on aero-optical properties. The simulation was conducted at Mach 4 over an adiabatic wall with a free stream density of 0.5 kg/m^3, and a free stream temperature of 5000 K. The free stream is representative of the post shock conditions of a wedge flying at Mach 20 (at an altitude of 20 km). Optical calculations were performed on each flow using the Gladstone-Dale relation. The flow fields, obtained with both perfect and real gas assumptions, produced non-linear OPD profiles, characteristic of fluctuating, turbulent flow. Furthermore, the perfect gas OPD was on average 89% larger than the real gas OPD. This is caused by the larger fluctuations in density experienced by the perfect gas flow (due to the relatively higher energy in the translational mode when compared to the real gas flow). The results presented suggest that capturing the features of resolved turbulence experiencing thermochemical nonequilibrium are important for aero-optical calculations. For the conditions studied, if nonequilibrium flow phenomena were to be neglected the optical distortion would be over-predicted.

Chapter IV presents the optical distortions that can be predicted in turbulent, high enthalpy flows. This was completed with only a cursory look at the various energy exchange processes. Chapter V is dedicated to discussing the energy exchanges in detail that can be seen or are expected to be seen in flows experiencing vortical break-down and thermochemical nonequilbrium.

CHAPTER VI

Role of Thermochemical Nonequilibrium in Turbulent Flows

6.1 Introduction

In Chapter V, a discussion of the aero-optical effects of a turbulent flow experiencing thermochemical nonequilibrium is presented. This study illustrates that the inclusion of thermochemical nonequilibrium in a turbulent flow caused conditions that reduced the optical distortion when compared to the same simulation performed utilizing a perfect gas assumption. The conclusion is presented without a detailed study of the energy exchanges that occur in turbulent flows experiencing thermochemical nonequilibrium. The goal of present chapter is to provide insight into the energy exchanges that occur when real gas effects are introduced to a flow characterised by vortical motion, as the result of these exchanges can have a significant impact on optical distortion.

Chapter VI presents a study on the canonical Taylor-Green vortex problem in order to discern the alterations in turbulent energy exchanges that occur when real gas effects are present in turbulent flow. This fundamental flow replicates many phenomena that are characteristic of turbulence [12], [15], [16]; turbulent decay and energy dissipation are present in this flow. Much like the phenomena that are ex-

perienced in real turbulent flows, the eddies stretch, dilate, and interact with one another [12]. Studying a more fundamental flow allows an investigation of the energy exchanges without the use of excessive computational resources or complications that are introduced with more realistic flow conditions.

The simulations presented in Chapter VI are performed using a perfect gas assumption and thermochemical nonequilibrium models. Two cases are run with each model type. One set utilizes an oxygen flow. The second set uses nitrogen as the simulation gas. Because each molecule vibrationally relaxes and dissociates at a different (molecule prescribed) energy level, studying different molecular species allows us to determine the effects of different nonequilibrium phenomena. Specifically, the oxygen flows are run to determine the effects of dissociation, while the nitrogen cases are utilized to determine the effects of vibrational relaxation. The initial conditions are prescribed such that vibrational excitation and dissociation occur within the region of interest for the vortical decay while still being somewhat representative of high altitude air-breathing hypersonic flight. The perfect gas simulations are included to provide a comparison for the simulations run with nonequilibrium models.

Chapter VI is divided into four section. Section 6.2 first presents the Taylor-Green vortex problem and presents how this canonical problem is altered to satisfy the requirements of this study. Section 6.3 then presents the specific conditions utilized in the study. Next, Section 6.4 presents the results from the O_2 and N_2 studies. Section 6.5 concludes with a summary of the pertinent findings of this study.

6.2 Taylor Green Vortex Problem

As discussed in Chapter I, turbulent eddies can range in size from the size of the boundary layer to very small scales which can be dissipated by viscosity. The large eddies break down into smaller eddies due to inviscid stretching. The resulting eddies then break down again due to the same phenomena. This process continues until the

eddies are small enough that viscous forces have an influence on the structures. At these small scales, the eddies are dissipated by viscosity. This process describes how kinetic energy is transferred through a turbulent flow and is often referred to as the turbulent energy cascade. The process of turbulent energy transfer and capturing all of the relevant scales can be computationally infeasible to resolve. As such, simplified flows can provide much insight into these flow phenomena.

One such simplified flow is the Taylor-Green Vortex (TGV) problem. The Taylor-Green Vortex is a simplistic problem where the turbulent cascade can be numerically obtained [12]. The TGV problem utilizes a single length scale (signifying a simple geometry) to represent complex phenomena. In the TGV, vortices are induced by the initial conditions presented in Eqn. (6.1).

$$u = U_\infty sin\left(\frac{x}{L}\right) cos\left(\frac{y}{L}\right) cos\left(\frac{z}{L}\right) \tag{6.1}$$

$$v = -U_\infty cos\left(\frac{x}{L}\right) sin\left(\frac{y}{L}\right) cos\left(\frac{z}{L}\right) \tag{6.2}$$

$$w = 0.0 \tag{6.3}$$

where ∞ signifies freestream conditions and L is the characteristic length of the computational domain which consists of a three dimensional, triply periodic box of size $2\pi L \times 2\pi L \times 2\pi L$. The thermodynamic variables are not modified due to vortical concerns and are applied according to Eqn. (6.4).

$$T = T_\infty \tag{6.4}$$

$$P = P_\infty \tag{6.5}$$

where, again, ∞ denotes freestream conditions.

The vortex sheets applied with Eqn. (6.1) are reduced to continuously smaller scales through the processes of three dimensional vortex stretching; see Fig. 6.1

which presents the canonical breakdown experienced in the Taylor Green Vortex problem. In Fig. 6.1, we see that the initial dynamics are relatively smooth. These

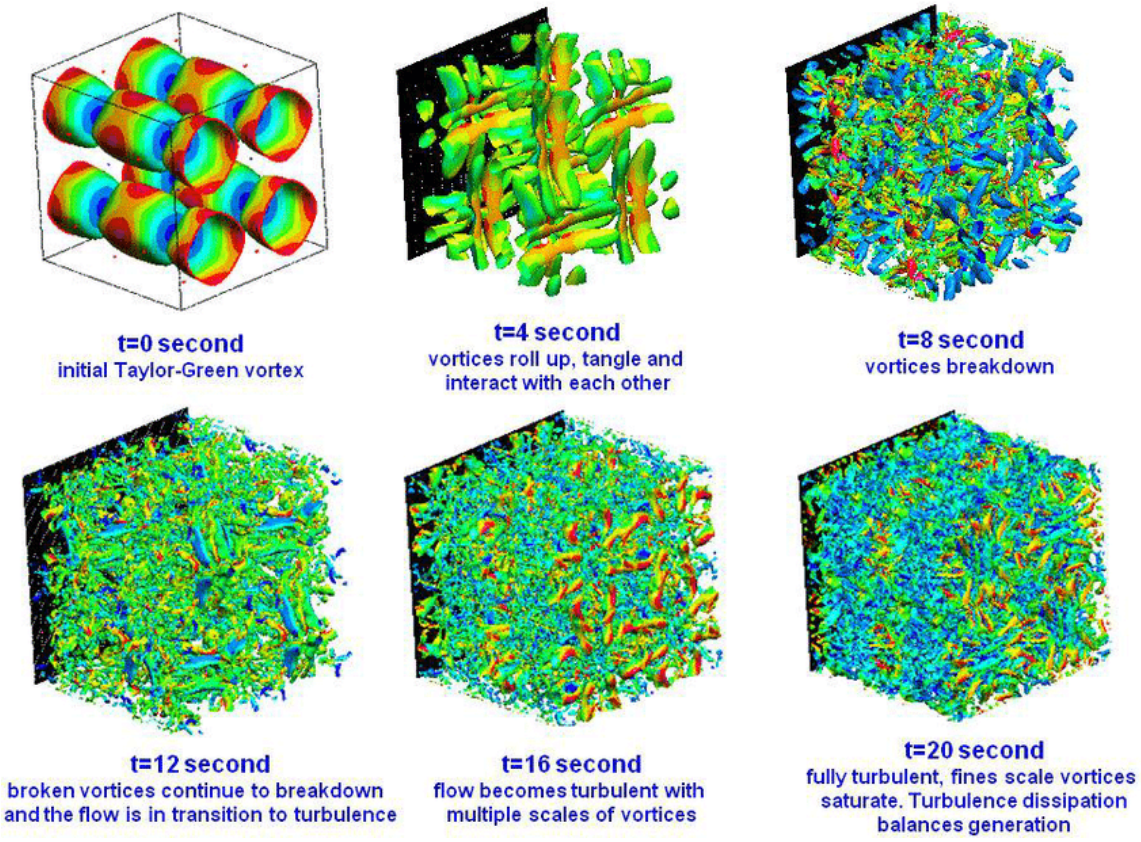

Figure 6.1: Vortical breakdown characteristic of the Taylor Green Vortex [64]

structures break down due to instabilities which are inherent to vortex-line stretching and reconnection; the flow becomes increasingly chaotic [12]. The stretching and eddy size reduction controls the evolution of the flow and is similar to that which occurs in turbulent flow.

Without further modification, the TGV problem does a poor job of mimicking hypersonic flow phenomena (lacks strong gradients in flow properties). In order to address this issue, a mean bulk velocity is added to the initial conditions. Eqn. (6.1)

is modified, and Eqn. (6.6) results from the modifications.

$$u = U_\infty + 0.1 \cdot U_\infty sin\left(\frac{x}{L}\right) cos\left(\frac{y}{L}\right) cos\left(\frac{z}{L}\right) \tag{6.6}$$

$$v = U_\infty - 0.1 \cdot U_\infty cos\left(\frac{x}{L}\right) sin\left(\frac{y}{L}\right) cos\left(\frac{z}{L}\right) \tag{6.7}$$

$$w = 0.0 \tag{6.8}$$

The adjustment imposes a mean velocity, about which the vortical perturbations are applied. This make the problem more realistic as flows around a hypersonic vehicle have mean velocities. The next issue to be addressed is the lack of thermal nonequilibrium present in the TGV. The TGV problem also lacks realistic areas of strong gradients that are likely to induce such thermal excitation and consequently thermal nonequilibrium. This is addressed by simply applying one temperature to describe the translational energy of the flow and applying a different temperature to describe the vibrational energy. These temperatures are chosen to be representative of post-shock conditions; section 6.3 details the exact conditions considered in this study. After these initial conditions are imposed, the flow can progress in time to relax according to each physically prescribed relaxation time. The initial temperatures are also chosen to ensure that the dissociation process for the oxygen molecule is activated.

6.3 Conditions of Numerical Simulation

The conditions of numerical simulation are presented in two sections. The first section presents the initial flow parameters. The second section presents the mesh and computational specifications utilized in the simulations.

6.3.1 Flow Parameters

The numerical conditions are chosen to approximately realize the post-shock conditions around an air-breathing hypersonic vehicle while keeping computational re-

quirements feasible. The velocity is chosen to represent the flow near a blunt body, away from the stagnation region (where the flow is reduced to sub-sonic speeds by a near-normal shock). The length scale is set to 1 m to ease the complexity of calculations. The flow conditions are presented in Table 6.1. Pressure is chosen to be

Table 6.1: Test Conditions

Parameter	Value
L	1 meter
Mach Number	1.2
T_v	300 K
T_∞	4000 K
P_∞	1200 Pa

sufficiently high to satisfy the Reynolds number requirement for realistic turbulence; the Reynolds number for both sets of simulations is on the order of 10^5. While this higher pressure promotes equilibration of flow due to increased number of collisions, creation of realistic turbulent-like fluctuations in this study is of great importance.

6.3.2 Mesh and Computational Considerations

The simulations in this study are conducted on periodic boxes with sides of length $2\pi L$. All simulations are performed on the same grid to facilitate comparison. Initial grids of size 32^3 are used. Simulations are run on progressively denser meshes until the solution, as indicated by the turbulent energy cascade, approaches the DNS published data [15]. These simulations are run on 4096 processors for approximately 100 hours.

This study is conducted with the use of Hypercode, a computational fluid dynamics code created for use with high enthalpy flows. Hypercode uses a finite volume approach to approximate the Navier-Stokes equations. The code utilizes 4th-order central schemes for the viscous fluxes. The inviscid fluxes are calculated using a 5th-order WENO stencil with AUSM flux splitting [34], [49]. Progression in time is conducted using the implicit RK-3 method. Hypercode utilizes finite rate chemistry with Park coefficients and the Landau-Teller model to describe thermochemical

nonequilbrium [43],[32]. Viscosity is described with Wilkies mixing rule and Blottner curve fits [60],[7]. Thermal transport is described using Eucken's formulation [9]. An explicit sub-grid scale is not applied, nor is an attempt to resolve all flow features made. Instead, an implicit large eddy approach is taken. All features that are not resolved by the grid are numerically dissipated with the aid of the finite volume formulation, which is inherently diffusive.

Hypercode is a code that is still in early developmental stages. As such, it is important to verify and validate the results it produces. In order to accomplish validation, a set of experimental results is normally required. However, the literature regarding turbulent flows in thermochemical nonequilibrium is very sparse and often computational in nature. In order to verify and validate the applications presented in this study, Hypercode was utilized to reproduce the unmodified Taylor-Green vortex problem as published at the AIAA 1st International Workshop on High Order CFD methods. This case was specifically developed to test and evaluate the performance of higher-order CFD codes. The AIAA test case utilizes Eqns. (6.1) and (6.4) as initial conditions. Because many LES codes are non-dimensional, AIAA presents these cases as consisting of a turbulent Mach number of 0.1 and a Reynolds number of 1600 [15]. The freestream parameters used with Hypercode are presented in Table 6.2.

Table 6.2: Test Conditions

Parameter	Value
L	1 meter
Mach Number	0.1
T_∞	300 K
P_∞	1200 Pa

Figure 6.2 presents the resulting decay of kinetic energy. Kinetic energy is presented as it is the characteristic result of the Taylor-Green Vortex problem. In Fig.

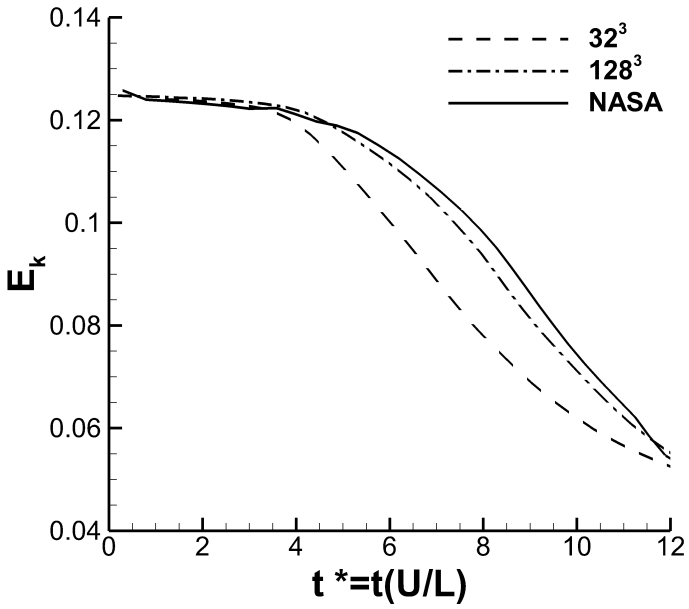

Figure 6.2: Comparison of vortical energy decay for various mesh sizes produced by Hypercode and decay produced WRLES [15]

6.2, kinetic energy is non-dimensionalized as in Eqn. (6.9).

$$E_k = \frac{1}{\rho_o \omega} \int \rho \frac{u_i u_i}{2} d\omega \tag{6.9}$$

A solution produced by NASA's high-order finite difference code WRLES is provided for comparison [15]. In Fig. 6.2, we see that the coarse mesh begins to decay earlier than the fine grid and the NASA produced solution. The decay does, however, appear to occur at the same rate. The coarse grid damps out the fluctuations more than the finer grid. The finer mesh produces a decay that varies from NASA's solution by less than 8%. Due to the computational requirements associated with Hypercode, it is infeasible to run simulations on denser grids at the present time.

The thermochemical models as implemented in Hypercode are evaluated by comparing the results of Hypercode to the established codes US3D and LeMANS [35],[53]. This is done by implementing the exact same models used in the established codes

and monitoring them while running a simple one dimensional problem. After each iteration, the mass fractions, vibrational relaxation coefficients, and nonequilibrium source terms are monitored and compared to ensure they were the same. Each code produced sufficiently similar values for each monitored variable. Compressible features of the code were validated by running the simplistic Sod shock tube problem [47].

6.4 Results

The results are divided into three sections. Section 6.4.1 presents a general assessment of the physics present in the flows. Section 6.4.2 presents the energy exchanges that occur within the flows with particular emphasis placed on the how the turbulent kinetic energy decay varies in the real gas simulations when compared to the perfect gas simulations. Section 6.4.3 presents an assessment of the resulting vortical structures present in each flow type.

6.4.1 General Flow Analysis

Figure 6.3 illustrates the evolution of the z-vorticity for the N_2 perfect gas case by presenting the contours at three different instances in time. It should be noted that all simulations in this study progress in an identical manner. The flow progression for all Taylor-Green simulations begins as smooth vortices; see Fig. 6.3a. These vortices then stretch and interact with one another. The flow becomes more chaotic. Figure 6.3b presents the vortical structure at an intermediate time in the vortex decay. As can be seen, the vortices have begun to break down and the areas of coherent structure are smaller. Figure 6.3c shows the computational domain near the end of the decay in energy. As the flow continues to experience stretching, the coherent structures become smaller and appear to be more disorderly.

Figure 6.4 presents the temperature evolution for the real gas cases for O_2 and

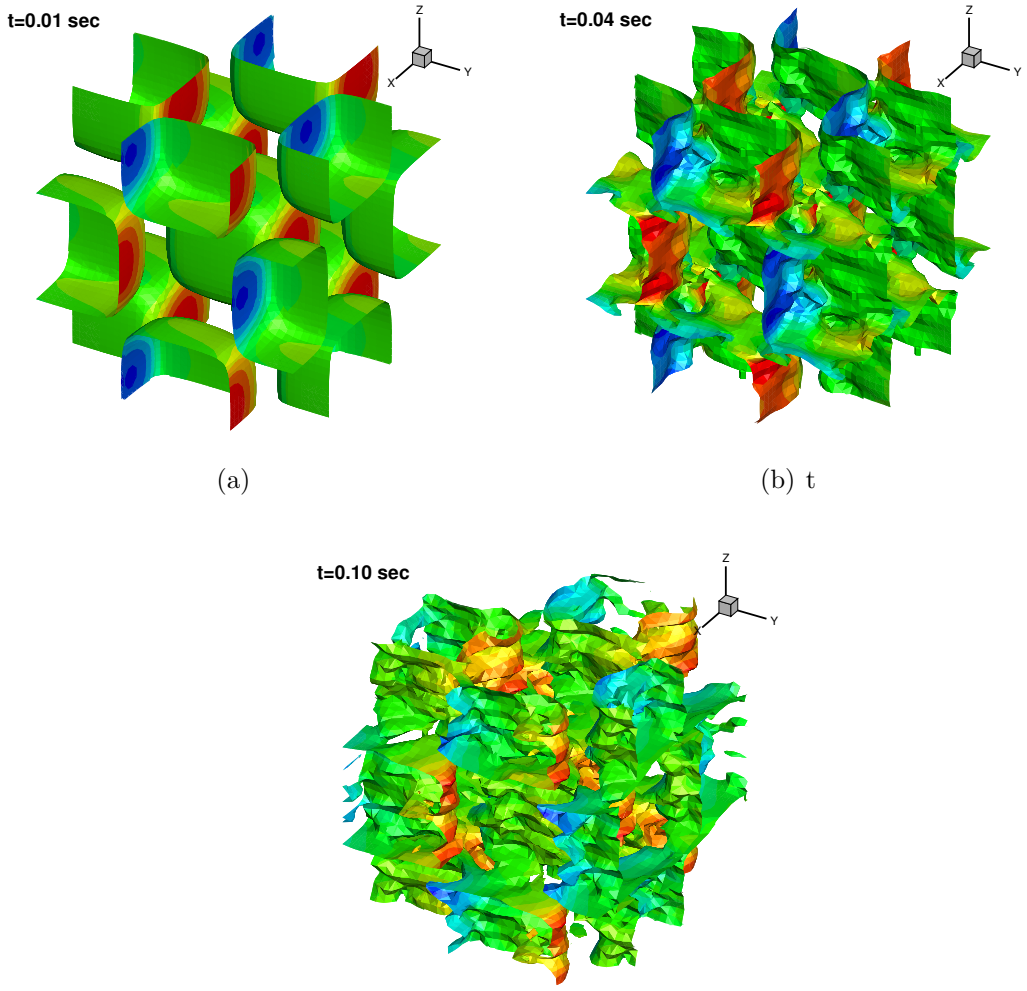

(a) (b) t

(c)

Figure 6.3: Vortical break down (as illustrated with vorticity iso-contours) experienced in the O_2 perfect gas flow at t=0.01 sec, (a.), t=0.04 sec, (b.), and t=0.10 sec,(c.).

N_2, respectively. The perfect gas simulations are not presented here since these simulations do not include the effects of excitation and relaxation; the temperature in the perfect gas simulations remains constant at 4000 K. As dictated by the molecule-prescribed relaxation rate, which is 66% higher for oxygen at the conditions present near the beginning of each simulation, oxygen quickly reaches equilibrium in the thermal modes; see Fig. 6.4a. At 1×10^{-4} seconds, well before the energy of the vortical motion decays appreciably, the oxygen flow is in thermal equilibrium. The equilibrated temperatures then continue to decrease in a near-concave manner. As

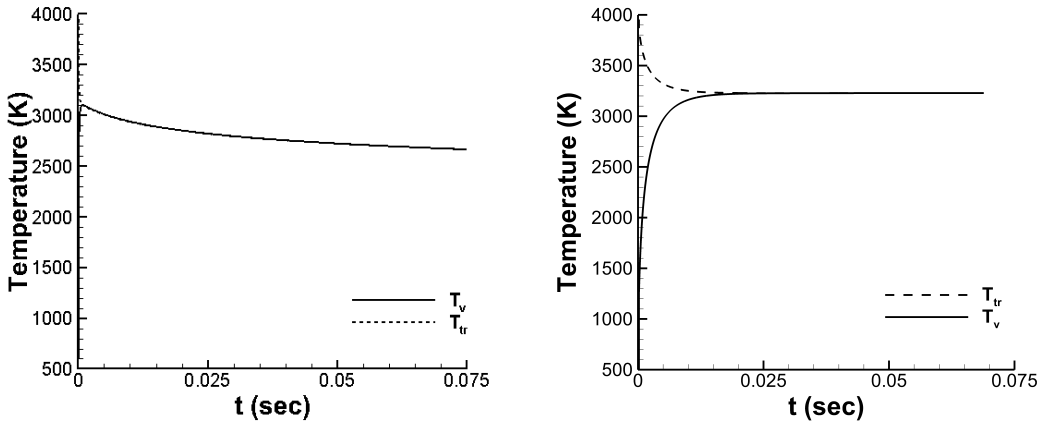

(a) (b)

Figure 6.4: Evolution of translational and vibrational temperature for (a.) O_2 and (b.) N_2 at 4000 K

we can see in Fig. 6.4b, the nitrogen simulation reaches thermal equilibrium at a later instance in time than the oxygen simulation. The translational and vibrational temperature which describe the nitrogen flows possess slight differences in value until approximately 0.03 seconds. These differences exist well into the initial decay of the vortical structures. Once the temperatures (representative of energy) equilibrate, they remain approximately constant. Unlike the oxygen flow, once the simulation is in thermal equilibrium little, or no energy is transferred into the chemical mode.

Dissociation occurs after the sum of the internal modes exceeds the dissociation energy. Oxygen will begin to dissociate at 2000 K and nitrogen begins to dissociate

at 4000 K in equilibrium conditions [2]. In order to illustrate the dissociative effects, Figure 6.5 presents the mass fraction evolution for the N_2 and O_2 flows, respectively. Again, the perfect gas simulations are not presented because the mass fractions in those simulations remain constant. As predicted by the temperature profiles, there is

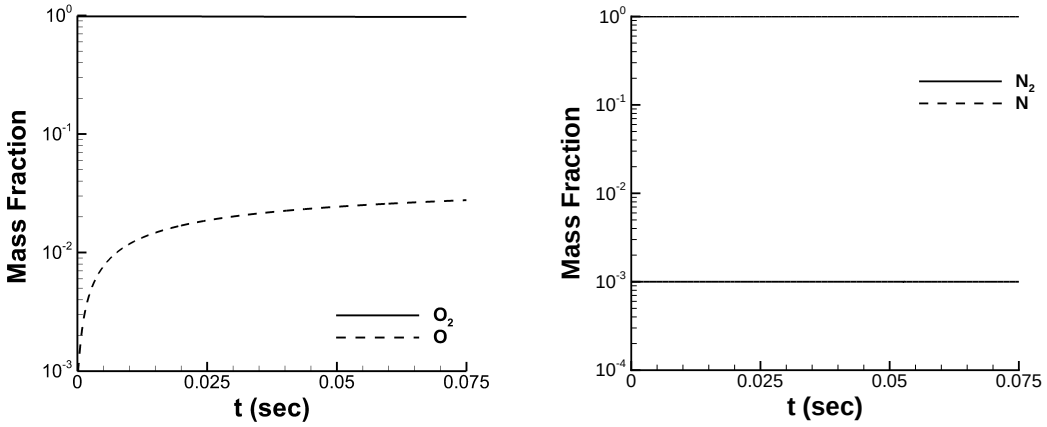

Figure 6.5: Evolution of mass fraction for the O_2 flow, (a.), and the N_2 flow, (b.), at 4000 K

no alteration in mass fraction values as the flow evolves for the nitrogen simulation. The temperature of the nitrogen flow reaches equilibrium in the thermal modes at approximately 3300 K, this is lower than the temperature at which the nitrogen is seen to begin dissociation. As suggested above, oxygen begins to dissociate at much lower temperatures. This fact is also evident in Fig. 6.5a. Diatomic oxygen's mass fraction begins to decrease in the flow, around 1×10^{-4} seconds after the flow reaches thermal equilibrium, and monatomic oxygen's mass fraction increases. The energy required to break the molecular bonds leaves the translational/vibrational modes and can be seen in Fig. 6.4a as a decrease in equilibrated temperatures for the real gas oxygen flows.

6.4.2 Energy Exchanges

The physics of the bulk flow quantities discussed in section 6.4.1 are manifestations of the energy exchanges which occur between the various modes available in each flow. Figure 6.6 illustrates the energy evolution for the real gas simulations of molecular nitrogen and oxygen flows, respectively. The vibrational, translational, and chemical energies are presented. In Fig. 6.6a, we see that the translational energy associated with the nitrogen simulation decreases until approximately 0.03 seconds (with the most of the decrease happening in the first 0.02 seconds). As the translational energy

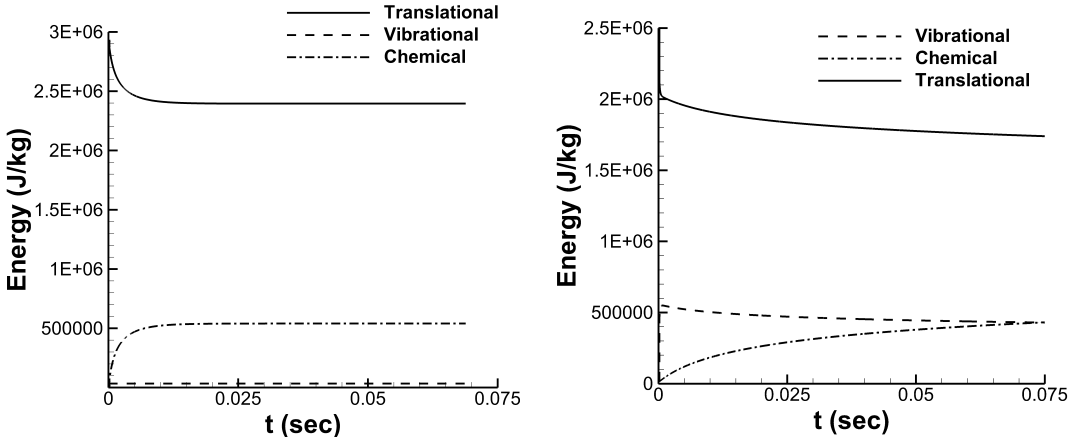

Figure 6.6: Energy evolution for N_2, (a.), and O_2, (b.), at 4000 K

decreases for the nitrogen flow, the energy in the vibrational mode increases until the point at which the vibrational mode is saturated. Once the translational and vibrational modes are in thermal equilibrium, the energy curves plateau, suggesting that there are no further energy exchanges occurring into the chemical mode. These trends are congruent with the trends in temperature and mass fraction evolution which are presented in Figs. 6.4 and 6.5.

In Fig. 6.6b, oxygen‘s vibrational energy rapidly increases while, at the same time, the translational energy quickly decreases. This exchange occurs at the earliest timesteps in the simulation, ending at t = 1×10^{-4} seconds. Once the vibrational

and translational modes are equilibrated, the energy in both modes decreases. Energy from the equilibrated modes is depleted through breaking the bonds within the oxygen molecule. Energy in the chemical mode, therefore, increases and continues to evolve over the lifespan of the Taylor-Green Vortex in the oxygen simulation. It is worth noting that the initial increase in chemical energy is steeper, approaching an eventual plateau (This provides a reason as to why the rate of change in kinetic energy does not continue to differ significantly from the perfect gas throughout the entire simulation).

Because the turbulent fluctuations have a profound impact on the optical distortion produced by a flowfield, the energy associated with the turbulence itself is of particular interest in this study. The cascade of energy created from the decay of vortical energy in the Taylor-Green problem is analogous to the decay of energy present in turbulent flows. Figure 6.7 presents the energy cascade of the vortical motion in the flow (the kinetic energy of the mean velocity is subtracted from the total kinetic energy) which is characteristic of the Taylor-Green problem. Figure 6.7a presents the vortical kinetic energy of the nitrogen simulation for the perfect and real gas simulations, respectively. Figure 6.7b presents the vortical energy decay of the oxygen simulations for the perfect and real gas simulations, respectively. For each flow set,

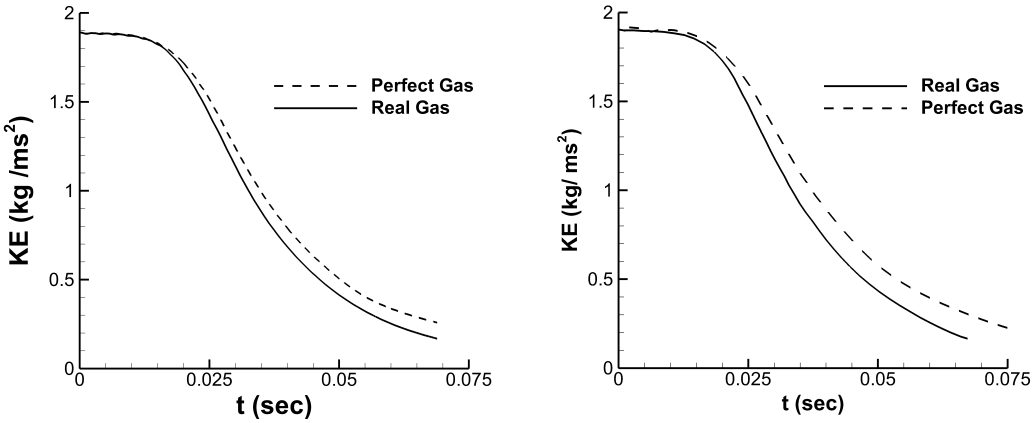

(a) (b)

Figure 6.7: Turbulent kinetic energy evolution of the Taylor Green vortices of perfect and real gases for N_2, (a.), and O_2, (b.)

the real gas simulations initially decay faster than the perfect gas simulations. The steeper decay can be attributed to the translational energy which is being transferred out of the this mode and into the vibrational and chemical modes.

While for both species real gas vortices appear to begin to decay at approximately 0.02 seconds, the real gas simulation diverges from the perfect gas simulation in a distinct manner for each species. Due to the differing energy exchanges that each real gas flow experiences, the energy decay differential evolves differently for the nitrogen and oxygen flows. In order to facilitate meaningful discussion on these differences, we introduce the acronym RPD which refers to the real gas/perfect gas differences in decay. At the onset of decay, the nitrogen simulation presents with a distinct RPD. As the simulation progresses, the RPD is nearly non-existent (the slope of decay for the real and perfect gas simulations is nearly identical). The initial RPD in the oxygen simulations appears to exist for a longer period of time (as indicated by the different slopes in the perfect and real gas curves). In all flows examined in this study, the vibrational energy exchanges occur more quickly than chemical dissociation, as such, much of its effects manifest at an early time.

To better illustrate and quantify the differences in the decay of each system's vortical kinetic energy Fig. 6.8 is presented and shows the time rates of change of kinetic energy for the real gas nitrogen and oxygen simulations, respectively. Each species' figure also presents the time rate of change in the kinetic energy for the perfect gas flows in order to facilitate discernment of the effects of thermochemical nonequilibrium on vortical energy exchanges. The rate of decay for the nitrogen real gas simulation shows a slight deviation (of less than 5%) from the perfect gas curve which begins at t=0.02 seconds and reaches a maximum at 0.025 seconds. The rate of decay for real gas nitrogen then proceeds to become nearly indistinguishable from the perfect nitrogen gas flow. The general shape and behavior of the decay is largely unaltered; the maximum rate of decay occurs at approximately the same time for the

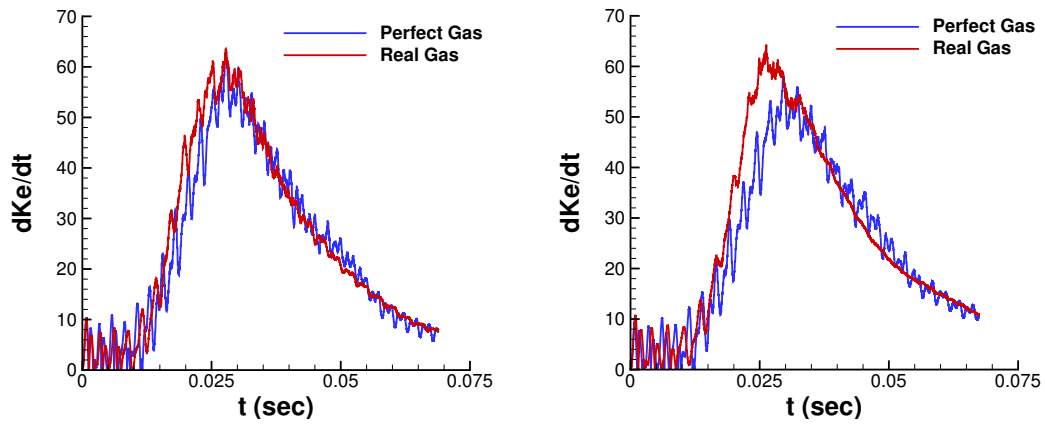

Figure 6.8: Evolution in change in kinetic energy for (a.) N_2 and (b.) O_2 at 4000 K

nitrogen real and perfect gas simulations.

Larger differences are present in the oxygen flows. For these flows, rate of decay of the kinetic energy deviates from the perfect gas flow curve from approximately 0.02 seconds to 0.04 seconds. The real gas deviation from the perfect gas flow is also larger. The maximum rate of decay is higher and occurs at an earlier time. Another difference for the rate of decay of kinetic energy between real and perfect flows can be found in the behavior of the curves at times greater than 0.04 seconds; see Fig. 6.8. The oxygen real gas flow produces rates of decay that appear to evolve in a much smoother manner. This behavior suggests that there are less oscillations in the kinetic energy between concurrent time steps.

The differences present between each species' energy evolution is introduced into this study through the inclusion of thermochemical nonequilibrium. For all real gas flows, the inclusion of such effects enhances the rate of decay of the vortical features present in the flows. The differences are smaller for the nitrogen case which experiences only vibrational relaxation, as the chemical dissociation is minimal and unimportant in the flow. The differences introduced to the oxygen simulations produce larger effects and are the result of chemical dissociation, as the vibrational relaxation

occurs very rapidly in the flow (as it would for many pressures of interest to the assessment of hypersonic turbulent flow).

6.4.3 Analysis of Vortical Structure

Lower levels of vortical kinetic energy at an instant in time indicates that the vortices in the flowfield at that time are less energetic and have smaller perturbations about the mean velocity within the flow. Section 6.4.3 presents a qualitative assessment of these structured fluctuations and the effects that real gas flow phenomena have on them.

Figure 6.9 presents vorticity iso-contours (magnitude of vorticity equal to 64 to highlight structural differences) for the nitrogen real and perfect gas flows at t=0.04 seconds, respectively. This time is chosen because at this point in the flow, the vortices

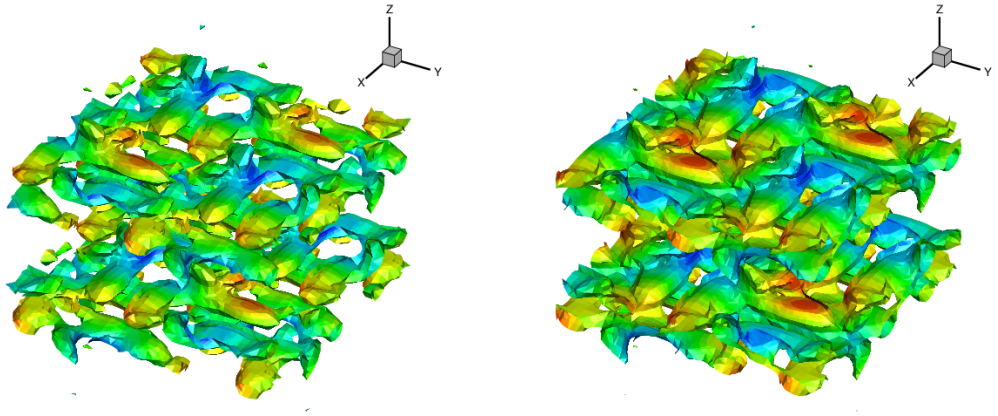

(a) (b)

Figure 6.9: Vorticity iso-contours for N_2 real, (a.), and perfect, (b.), gas simulations at 4000 K

have had sufficient time to begin the decay process. As consistent with the lower kinetic energy at this instance in time, the structures (representing vortical motion) in the real gas flow are seen to be damped. In Fig. 6.9, the real gas structures are smaller in appearance than the perfect gas structures. The structures in the perfect gas flow are thicker and populate more of the computational domain. Because this

portion of the flow is not near the initial decay of the vortices, the structures present in the real and perfect gas flows are chaotic in appearance. The initial vortices have been broken down, resulting in small vortical structures in the flows.

Figure 6.10 presents vorticity iso-contours (magnitude of vorticity equal to 64 to highlight structures) for the oxygen real and perfect gas flows at time = 0.04 seconds, respectively. At this instance in the lifetime of the vortical decay, the flow

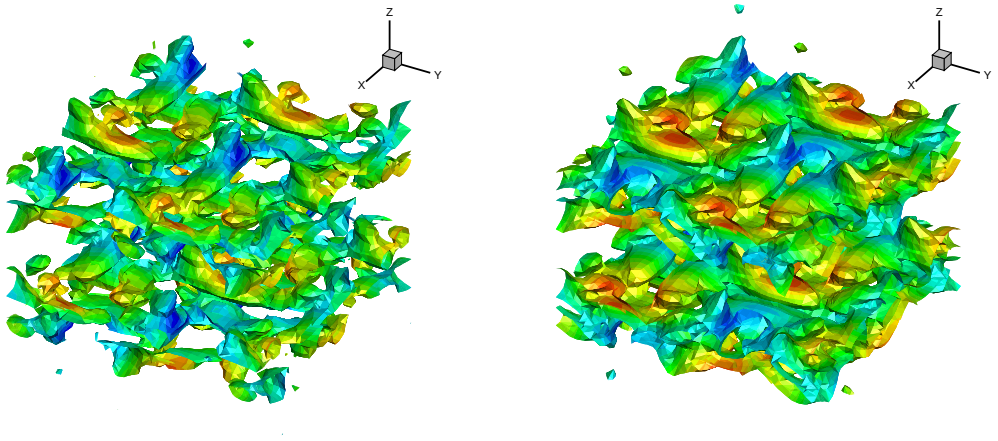

(a) (b)

Figure 6.10: Vorticity iso-contours for O_2 real, (a.), and perfect, (b.), gas simulations at 4000 K

is approximately half way through the decay process. Both the real and perfect gas contours illustrate Taylor-Green vortices that have undergone much stretching and consequent break-down. The flows, in general, are similarly chaotic to the flows presented in Fig. 6.9 due to the time at which the results are analyzed. The structures in the real gas flow are damped when compared to those produced while utilizing the perfect gas assumption in the oxygen flow. The structures in the real gas simulation are smaller and occupy less room, as indicated by the presence of more whitespace in the iso-contour.

The damping of vorticity and velocity can also manifest as the presence of less density variation. Density is presented here due to the large influence it has on optical abberations. As a beam travels through a field of varying density, it experiences dif-

ferent indices of refraction. Therefore, the portions of the beam will travel at different local speeds. The resulting signal has portions that have experienced phase shifts. Figure 6.11 presents the average density iso-contours for the real and perfect gas nitrogen flows. The real gas density iso-contour occupies more of the computational

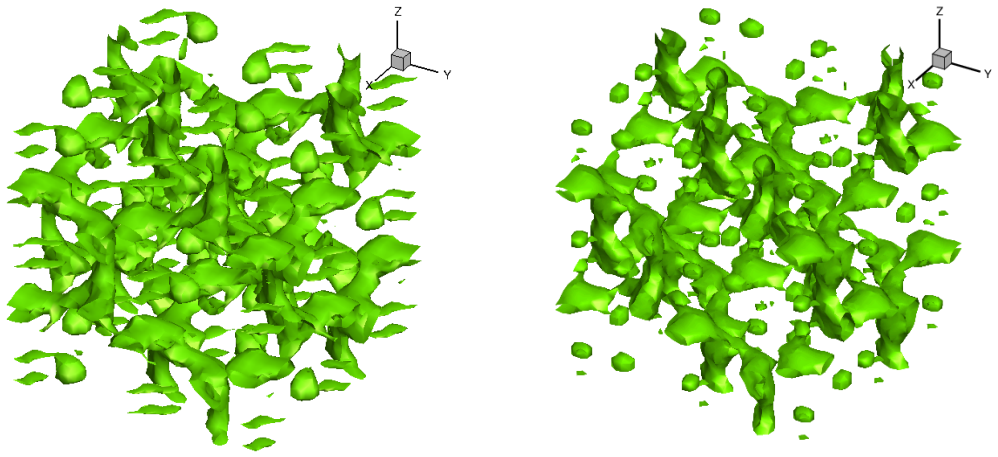

(a) (b)

Figure 6.11: Density iso-contours for N_2 real, (a.), and perfect, (b.), gas simulations at 4000 K

domain than the perfect gas density iso-contour for the nitrogen simulations. In Fig. 6.11a, a larger area of the computational domain in the real gas simulation is at a constant level of density, suggesting there is less variation in this variable. More of the density-varying vortices have been damped in the real gas flow than in the perfect gas flow. This is due to the energy leaving the translational mode and going into the excited vibrational mode.

Figure 6.12 presents the density contours for the real and perfect gas flows for the oxygen flows, respectively. The patterns seen in Fig. 6.11 are replicated here. The area of constant density is larger for the real gas flow due to the presence of density varying structures in the real gas flow that are smaller than those in the perfect gas flow.

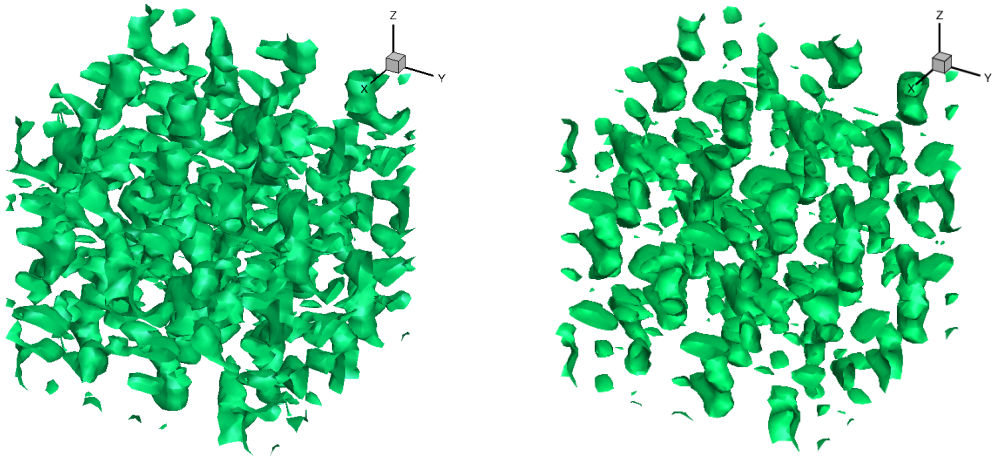

(a) (b)

Figure 6.12: Density iso-contours for O_2 real, (a.), and perfect, (b.), gas simulations at 4000 K

6.5 Summary

Chapter VI presented the Taylor-Green vortex problem in order to discern the effects of thermochemical nonequilibrium flow phenomena on turbulent energy transfer. Mach 1.2 simulations of the Taylor-Green Vortices were performed with pure oxygen and pure nitrogen flows. Each set of simulations were performed utilizing both perfect gas and thermochemical nonequilibrium models. The perfect gas simulations provided a comparison for the simulations utilizing the thermochemical nonequilbrium models. The real gas initial temperatures were set to 4000 K to describe the translational energy and 300 K to describe the vibrational energy. These conditions were chosen to replicate realizable post-shock conditions for an air breathing hypersonic vehicle engaged in intelligence, surveillance, and reconnaissance (ISR) missions.

The kinetic energy decay for all real gas cases experienced an onset of decay in vortical structure that occurred earlier than the onset in the perfect gas cases. This is caused from the energy leaving the eddies due to excited internal modes. The difference in the rate of decay was higher for both real gas flows until approximately 0.03 seconds. The real gas oxygen flow differed from its perfect gas counterpart predomi-

nantly due to the dissociation present in the real gas flow. The real gas nitrogen flow differed from its perfect gas flow counterpart because of the vibrational relaxation present in the real gas flow. The decay of vortical structures like those present in turbulence was enhanced by the inclusion of thermochemical nonequilibrium. In the present study, the decay was enhanced to a greater degree due to the presence of dissociation by the relatively short time scale that is characteristic of the vibrational relaxation. These findings have implications on fully turbulent flows because they show that turbulent energy is reduced in the presence of thermochemical nonequilibrium.

The lower amount of kinetic energy present in the flow at an instant in time manifested as smaller structures being present in all real gas flows when compared to their respective perfect gas counterparts. As such, the smaller kinetic energy associated with the vortical flow has optical implications such as those seen in Chapter IV where the inclusion of thermochemical nonequilibrium in turbulent flows reduced optical distortion.

It should be noted that the study performed here is for a simplistic flow. Further investigation is required to affirm whether the conjectures presented here are present for all turbulent flows that experience similar exchanges of energy.

CHAPTER VII

Conclusion

In each chapter, results were presented and conclusions were deduced. The present chapter summarizes each study and presents the most pertinent conclusions that can be discerned from each. The current chapter also presents the original contributions to the field represented by the studies contained within this thesis. The present chapter concludes by suggesting possible further work that can be pursued in the relatively young field of aero-optics as it pertains to hypersonic flow fields.

7.1 Summary

Chapter I provided the motivation for the present study. Hypersonic vehicles were presented as potential platforms for missions involved in intelligence, surveyance, and reconnaissance missions (ISR). Chapter I then provided general information on the sources of signal distortion which sensors on such vehicles may encounter. Possible types of sensor degradation were presented as radio frequency distortion, concerns derived from the sensor or sensor window being exposed to elevated temperatures, and electro-optical and infrared signal distortion. Hypersonic flowfields with elevated temperatures and strong entropy gradients were presented as particularly detrimental to sensing missions. This provided the motivation for the work presented in Chapters III-VI. Chapter I also presented relevant information regarding two facets of

hypersonic flows that may be particularly detrimental to an electro-optical/infrared sensing mission: hypersonic thermochemistry, and turbulence. Hypersonic thermochemistry were presented as consisting of strong gradients in flow conditions and potential nonequilibrium in the thermal and chemical modes. As a signal traverses a flow field, it will encounter varying indices of refraction, causing local phase shifts in the initially coherent wave structure. These phase shifts experienced by a beam can be greater in nonequilibrium flow fields since these flow fields are often characterized by strong gradients. Turbulence was presented as a chaotic phenomenon that can further induce variations in the flowfield and thus obscure signals. A brief discussion of turbulent theory was also presented to provide insight into modeling this phenomena and to describe the manner in which turbulence and thermochemical nonequilibrium may interact.

Chapter II presented the numerical analysis approaches, of both the flowfield and the optical distortion, that are used in the majority of this dissertation. Chapter II began by presenting the Navier-Stokes equations with particular emphasis placed on the modifications that enable the Navier-Stokes equations to be utilized for flows experiencing thermochemical nonequilibrium. The Landau-Teller model and finite rate chemistry with Park's two temperature correction were presented as the nonequilibrium models utilized in this dissertation. Chapter II then presented the modifications that were made to the hypersonic flow code LeMANS in order to enable the originally laminar solver to solve for turbulent flows. This was accomplished through the utilization of the Reynolds-Averaged Navier-Stokes equations (RANS). This chapter presented the methods used to include the Spalart-Allmaras turbulence closure model to the RANS equations. Chapter II concluded with a presentation of the optical analysis used in Chapters IV-VI. The Gladstone-Dale equation was presented for use in perfect gas and real gas flows. A brief discussion regarding the model's constants for each real gas species was provided for 5 species air.

Chapter III presented a preliminary assessment of various types of sensor degradation that can arise in hypersonic flowfields. This task is accomplished through the utilization of simplistic models and analysis that were also presented in the chapter. The types of sensor depredation that were analyzed in this chapter are radio frequency degradation that is caused by the formation of a plasma sheath, sensor or sensor windows being damaged by exposure to the flowfield, and electro-optical/infrared (EO/IR) signal abberation caused from variable indices of refraction within the flowfield. A Mach 7 flow around a axi-symmetric cone was studied utilizing an 11 species chemistry model. Various paths through the flow were analyzed for the radio frequency and EO/IR analysis. It was discovered that the plasma frequency for the air-breathing vehicle was sufficiently low that only radio signals of frequencies that are more than two orders of magnitude lower than those commonly used in communications would be affected. It was concluded that this type of signal distortion is unlikely to be experienced for these air-breathing vehicles. EO/IR signals were also analyzed using two methods. One method, derived for free shear flows, produced very low levels of distortion. The other method, derived for turbulent flow over a flat plate, provided larger distortions. Both methods were derived for very specific flow types, and it is unclear how they perform when the flow-type in the study deviates from the original flow type. As such, more detailed, rigorous studies of this type of EO/IR distortion are required. The final aspect of the flow that was analysed is the surface temperature. The surface temperature of the vehicle in this study was sufficiently low that the sensors would not experience degradation (from temperature alone) as long as they were not placed on or near the stagnation point.

Chapter IV presented the isolated effects of thermochemical nonequilibrium on optical distortion. The studies were conducted on an axi-symmetric hemisphere-cylinder at Mach 11, 13, and 15. A perfect gas solution was provided for comparison at Mach 11 and 15. At both Mach numbers, the real gas simulations produced greater optical

distortion than those predicted assuming a perfect gas model. At Mach 11, however, the differences were slight and the optical path differences (OPD) varied by less than 0.2%. At the higher Mach number, the root mean squared OPD for the real gas flow was 5% larger than that produced with a perfect gas approximation. Chapter IV also presented a determination of the sensitivity of optical parameters to thermochemical nonequilibrium. In Chapter IV, it was shown that the higher dissociation that occurs at higher freestream Mach numbers caused an increase in the Gladstone-Dale constants and consequently the optical path length (OPL). Furthermore, at all Mach numbers, the real gas OPL increased predominantly due to oxygen dissociation. Dissociated nitrogen had a smaller effect at the higher Mach numbers. Creation of NO had the smallest effect on optical distortion in this portion of the study. Chapter IV presented the conclusion that the species diffusion had almost no effect on optical distortion; the OPD predicted when excluding diffusion was approximately equal to the distortion predicted when including diffusion.

Chapter V presented the role of high speed turbulence on aero-optical assessments. In this chapter, two studies were analyzed in order to discern the effects of turbulence on optical abberations. One study consisted of a Mach 6 flow over a flat plate. For this case, flow conditions were such that thermochemical nonequilibrium did not play a large role in the flow. Instead, these flows were utilized to determine the effects of varying levels of turbulence modeling on optical distortion. In this study it was assumed that the large eddy simulation provides the most accurate solution. It was shown that while solving the Reynolds-Averaged Navier-Stokes (RANS) equations accurately predicts mean flow quantities, this method does not accurately predict optical distortion created by a turbulent flow. The average optical solution predicted by LES was two orders of magnitude larger than optical distortion predicted by RANS. In fact, it was shown that the distortion predicted by RANS was much closer to the level of optical abberations that was predicted by a laminar solution. The second

study presented in Chapter V consisted of a Mach 4 turbulent flow over a flat plate. While this Mach number is not in the traditional hypersonic regime, conditions were such that nonequilibrium flow phenomena were present in the flow. The freestream conditions are representative of the post shock conditions of a 21 degree wedge flying at Mach 20 at 20 km in altitude [17]. This study was performed utilizing a calorically perfect gas model and using thermochemical nonequilibrium models. The perfect gas case provided a comparison to determine the effect of including thermochemical nonequilbrium in a turbulent flow. This study illustrated that the optical path difference was reduced by 89% when real gas flow phenomena were included in the turbulence simulations. It was suggested that energy in the turbulence was reduced by excitation of internal molecular energy modes and thus the turbulent fluctuations were reduced in magnitude.

Chapter VI presented analysis of the Taylor-Green Vortex problem. This problem was utilized to gain insight into the energy exchange phenomena that occur when real gas flow phenomena are introduced into decaying vortices and in order to better explain the findings of Chapter V. The energy exchanging processes in the Taylor-Green problem were numerically similar to the processes that occur in real turbulent flows. Studying the changes in the energy transfer in this problem, therefore, provided insight into the exchanges occurring in real turbulence. The Taylor-Green problem was performed using real and perfect gas models. Each method, both real and perfect were applied to two separate flows. One set consisted of flows containing only N_2, and the other set consisted of simulations utilizing O_2 . Studying the differing molecules enabled one to separately discern the effect of vibrational relaxation and chemical dissociation on vortical energy exchanges. In this chapter, it was shown that inclusion of real gas effects promotes vortical breakdown and damps out density variation. The vortical kinetic energy for all real gas cases begins to decay before the onset in the perfect gas cases. This is caused by the energy being taken from the vortical structures

due to excited internal energy modes. The rate of decay was higher for both species' real gas flows. The real gas oxygen flow differs from its perfect gas counterpart predominantly due to dissociation. The real gas nitrogen flow differs from its perfect gas counterpart because of the vibrational relaxation present in the real gas flow. The chemical dissociation affected the decay of the kinetic energy for a longer period of time than the vibrational relaxation.

7.2 Contributions

The work detailed in this dissertation advances multiple fields, primarily through the assessment of physical features present in hypersonic flow fields. Many of the contributions to our understanding of potential aero-optical distortions pertain to the determination of important physical flow features that are required to successfully predict signal abberation in a hypersonic flowfield. Various advances were also made in the field of modeling turbulent flows by inclusion of thermochemical nonequilbrium models and performing detailed studies on such flows. Specific contributions to physical understanding are as outlined blow:

- Through the work presented in this dissertation, it was determined that the thermochemical nonequilibrium present in hypersonic flows produces larger optical distortion than if the flow did not have nonequilibrium features. The differences in optical distortion are slight (maximum of 5% different for the hemisphere-cylinder simulations considered in this study) and increase with Mach number. It was also determined that the optical parameters are most sensitive to the inclusion of oxygen dissociation, as oxygen most readily dissociates in shock-layers of air-breathing hypersonic vehicles. These findings are for laminar flows.

- Through the physics analyzed in this dissertation, it was also determined that turbulence has the largest effect on optical distortion of any single flow phe-

nomenon analyzed in this thesis (thermochemical nonequilibrium and turbulence), and this distortion cannot be predicted accurately by steady RANS calculations. In this study, inclusion of resolved turbulence using implicit large eddy simulation produced average optical distortion, as measured by optical path difference, that is two orders of magnitude larger than those produced by laminar or RANS solutions.

- This dissertation further provided information regarding the role of thermochemical nonequilibrium in high enthalpy turbulent flows, especially as they affect aero-optical assessments. The thermochemical nonequilibrium flow features dampen turbulent fluctuations and, consequently, there is less variation in index of refraction in these flows. Optical distortion is reduced in the presence of thermochemical nonequilibrium in turbulent flows. The optical distortion was reduced by 75% for the study presented in this dissertation.

- The final physical contribution provided by the work in this dissertation is detailed information regarding the energy exchanges in turbulent flows that experience thermochemical nonequilbrium. This portion of the thesis provided physical reasoning as to why turbulent fluctuations are damped when thermochemical nonequilbrium is introduced to a turbulent flow. Turbulent fluctuations are damped when thermochemical nonequilbrium is present in the flow due to the turbulent kinetic energy being consumed by excited internal energy modes. The phenomenon of dissociation is particularly effective at damping fluctuations. Such a thorough explanation has thus far been lacking in the existing literature.

- Computational advances and contributions were required to perform the simulations presented in this dissertation. LeMANS was modified from a laminar solver to include turbulent effects through the inclusion of the Reynolds-

Averaged Navier Stokes equations and various closure models. The Taylor-Green Vortex problem was performed through contribution to the development of a high-order CFD code which advances the state of the art for high fidelity codes that are used to assess high enthalpy flow physics. This code couples high order finite volume formulations (in all fluxes) with a frame work to introduce resolved vibrational state equations. Many existing finite volume CFD codes use 2nd-order schemes to resolve viscous fluxes [62],[53]. Furthermore, many high enthalpy codes that can also resolve turbulent structures do not have high fidelity thermochemical nonequilibrium models [53].

The physical understanding that is gained from the information within this dissertation provides guidelines as to which phenomena in hypersonic flow are important to assess to accurately predict EO/IR signal distortion. This information will help in discerning if incurring the additional cost of performing resolved turbulence simulations is required for various applications. The approximate computational times for a simplistic flat plate case performed with each simulation type relevant to this study are presented in Table 7.1. While solving the additional equations that are required

Table 7.1: Approximate Computational Time for Simulation Type

Simulation Type	Approximate Time
Laminar Perfect Gas	1.5 hours
RANS Perfect Gas	2.0 hours
ILES Perfect Gas	$1,000,000$ hours
Laminar Real Gas	2 hours
RANS Real Gas	2.5 hours
ILES Real Gas	$1,000,000$ hours

for the modeling of thermochemical nonequilibrium did add computational time to the laminar and RANS test cases, the addition of the nonequilibrium models to the large eddy simulations did not significantly alter total computational time. These similar times are resultant of the differing times required for each flow to transition to fully turbulent and the relatively large time associated with data acquisition.

7.3 Future Work

While this dissertation provides insight into which physical flow phenomena are important to accurately predict the optical distortion created by a vehicle traveling at hypersonic speeds, certain aspects of the optical analysis process can be improved. The suggestions for the improvements are outlined in the following. Ways to pursue the topics presented in this dissertation further are also presented here.

The first set of suggested improvements concerns the nonequilibrium modeling performed in this dissertation. There are many shortcomings present in the models that are employed in this work. It should be noted that Park's two temperature model was developed based on experimental investigations and may not accurately describe flow with rotational nonequilibrium and significant radiation that induces ionization [44]. The Landau-Teller model assumes only weak deviations from equilibrium. It also assumes the molecules behave as a simple harmonic oscillator, and it only allows for single quantum jumps [55]. Millikan and White relaxation times were derived from empirical curve fits that do not accurately represent high temperature nonequilibrium physics [9]. The data for these curve fits are collected from shock tube experiments performed at temperatures ranging from 300 K to 8000 K [38]. Because of the narrow temperature range used to derive the fit, the curve fit only reports relaxation at certain vibrational levels. The implementation of high fidelity (possibly state resolved) thermochemical models may be necessary to obtain a more accurate prediction of the optical distortion in a hypersonic flowfield.

The second set of suggested improvements pertains to the optical calculations performed in this dissertation. In the derivation of the Gladstone-Dale relation which is used extensively in this dissertation, it was assumed that the medium through which the light travels is transparent and that absorption can be neglected [51]. The beam's absorption of radiation emitted by a high energy gas, however, may be important. The current analysis also neglects the molecules in high vibrational states

that could potentially have differing polarizabilities [1] and thus different Gladstone-Dale constants. Another feature that is not considered in this study is chemistry involving the vehicle's surface or sensor window. Furthermore, the use of 11 species chemistry may provide better assessment of aero-optical distortion. Formation of plasma in the shock layer surrounding a hypersonic vehicle may have a profound impact on optical distortion, as free electrons have a negative index of refraction [37]. Unfortunately, at the present, information regarding all species' (in 11 species air) indices of refraction are not readily available [37].

Further research also needs to be conducted regarding the energy exchanges in turbulent hypersonic flows. The study presented in this dissertation was restricted to simplistic flows due to the availability of computational resources. In the future, it would be prudent to investigate more realistic turbulence that would be experienced on typical hypersonic vehicles. Specifically, more complex simulations are required to ensure the energy exchanging patterns witnessed in the Taylor-Green Vortex problem is universal. Due to the time scales involved in the Taylor-Green problem, it was not possible to assess a flow that experiences both significant thermal relaxation and dissociation. Performing such an experiment may provide more insight into all the energy exchanges interacting with one another.

APPENDICES

APPENDIX A

Three-Dimensional Reynolds Averaged Navier-Stokes Equations with Thermochemical Nonequilibrium Modifications

Presented below are the Reynolds-Averaged Navier-Stokes equations for modeling flows that experience thermochemical nonequilibrium (without ionization). Please note that if the turbulent kinetic energy is not provided by the closure model, it is customary to neglect such terms [21]. The nonequilibrium source terms are not modified to include interactions with turbulent fluctuations, as suggested by Ref. [21].

$$\frac{\partial(\rho_s)}{\partial t} + \frac{\partial(\rho_s u_j)}{\partial x_j} = \frac{\partial}{\partial x_j} + [(\rho D_s + \frac{\mu_t M_s}{S_{ct} M})\frac{\partial \chi_s}{\partial x_j}] + \dot{\omega}_s \tag{A.1}$$

$$\frac{\partial(\rho u_i)}{\partial t} + \frac{\partial(\rho u_i u_j)}{\partial x_j} = -\frac{\partial P}{\partial x_i} + \frac{\partial}{\partial x_j}[t_{ij} + \tau_i j] \tag{A.2}$$

$$\frac{\partial}{\partial t}[\rho(e+\frac{u_i u_i}{2}+k)]+\frac{\partial}{\partial x_j}[\rho u_j(h+\frac{u_i u_i}{2})+tke]= \\ \frac{\partial}{\partial x_j}[u_i(t_{ij}+\tau_{ij})]+\frac{\partial}{\partial x_j}[\sum \rho D_s+\frac{\mu_t M_s}{S_{ct}M}h_s\frac{\partial \chi_s}{\partial x_j}]+ \\ \frac{\partial}{\partial x_j}[(k+k_t)\frac{\partial T}{\partial x_j}+(k_v+k_{vt})\frac{\partial T_v}{\partial x_j}]+\frac{\partial}{\partial x_j}[(\mu+\sigma_k\frac{\rho k}{\omega})\frac{\partial tke}{\partial x_j}] \quad \text{(A.3)}$$

where

$$k_t=\frac{k}{k+k_v}\frac{\mu_t}{c_p Pr_t} \qquad k_{vt}=\frac{k_v}{k+k_v}\frac{\mu_t}{c_p Pr_t} \quad \text{(A.4)}$$

$$\frac{\partial \rho e_v}{\partial t}+\frac{\rho u_j e_v}{\partial x_j}=\frac{\partial}{\partial x_j}[\sum(\rho D_s+\frac{\mu_t M_s}{S_{ct}M})h_{v,s}\frac{\partial \chi_s}{\partial x_j}]+ \\ \frac{\partial}{\partial x_j}[(k_v+k_{vt})\frac{\partial T_v}{\partial x_j}]+\rho_s\dot{\omega}_s+\sum(\dot{\omega}_s D_s) \quad \text{(A.5)}$$

BIBLIOGRAPHY

BIBLIOGRAPHY

[1] Alpher, R. A., and D. R. White (1959), Optical Refractivity of High-Temperature Gases . I . Effects Resulting from Dissociation of Diatomic Gases, *The Physics of Fluids*, *2*, 153–161.

[2] Anderson, J. D. (1989), *Hypersonic and High Temperature Gas Dynamics*, 1st ed., McGraw-Hill.

[3] Anderson, J. D. (2003), *Modern Compressible Flow with Historical Perspective*, 3rd ed., McGraw-Hill.

[4] Anderson, J. H. B. (1967), An Experimental Determination of the Gladstone-Dale Constants for Dissociating Oxygen, *Tech. Rep. 105*, University of Toronto.

[5] Baxter, M., C. Truman, , and B. Masson (1988), Predicting the Optical Quality of Supersonic Shear Layers, *AIAA Paper 1988-2771*.

[6] Bird, R., W. Stewart, and E. Lightfoot (1960), *Transport Phenomena*, Wiley, New York.

[7] Blottner, F. G., M. Johnson, and M. Ellis (1971), Chemically Reacting Viscous Flow Program For Multi-Component Gas Mixtures, *Tech. Rep. SC-RR-70-754*, Sandia Laboratories, Albuquerque, NM.

[8] Born, M., and E. Wolfe (1975), *Principles of Optics*, Permagon Press.

[9] Boyd, I. D., and T. E. Schwartentruber (2017), *Nonequilibrium Gas Dynamics and Molecular Simulation*, Cambridge University Press.

[10] Breuer, K. S., and J. H. Haritonidis (1990), The evolution of a localized disturbance in a laminar boundary layer. I - Weak disturbances, *Journal of Fluid Mechanics*, *220*, 569–594.

[11] Brown, D. (2018), Boeing unveils conceptual hypersonic jet design to replace the SR-71 Blackbird, *Business Insider*, (Jan.).

[12] Bull, J., and A. Jameson (2015), Simulation of the taylorgreen vortex using high-order flux reconstruction schemes, *AIAA Journal*, *53*, 2750–2761, doi: 10.2514/1.J053766.

[13] Cartis, S., and B. Aupoix (2000), "Density Corrections for Turbulence Models, *Aerospace Science and Technology*.

[14] Cross, P. (2017), Conjugate Analysis of Two-Dimensional Ablation and Pyrolysis in Rocket Nozzles, Doctoral, University of Michigan.

[15] DeBonis, J. (2013), Solutions of the taylor-green vortex problem using high-resolution explicit finite difference methods, doi:10.2514/6.2013-382.

[16] Drikakis, D., C. Fureby, F. F. Grinstein, and D. Youngs (2007), Simulation of transition and turbulence decay in the taylorgreen vortex, *Journal of Turbulence*, *8*, N20, doi:10.1080/14685240701250289.

[17] Duan, L., and M. P. Martin (2009), Effect of Finite-Rate Chemical Reactions on Turbulence in Hypersonic Turbulent Boundary Layers, *AIAA Paper 2009-588*.

[18] F., M. (1992), Improved Two-Equation k-omega Turbulence Models for Aerodynamic Flow, *NASA STI/Recon Technical Report*.

[19] Gerorgiadis, N. J., D. P. Rizzetta, and C. Fureby (20110), Large-Eddy Simulation: Current Capabilities, Recommended Practices, and Future Research, *AIAA Journal*, pp. 1772–1784.

[20] Gladstone, J.H., and Dale, T.P. (1863), Researches on the Refraction , Dispersion , and Sensitiveness of Liquids, *Philosophical Transactions of the Royal Society of London*, *153*, 317–343.

[21] Gnoffo, P. A., S. A. Berry, and J. W. Van Norman (2011), Uncertainty Assessment of 2D and axisymmetric Hypersonic Shock Wave- Turbulent Boundary Layer Interaction Simulations Compression Corners, *AIAA Paper 2011-3142*.

[22] Gordeyev, S., A. E. Smith, J. A. Cress, and E. J. Jumper (2014), Experimental studies of aero-optical properties of subsonic turbulent boundary layers, *Journal of Fluid Mechanics*, *740*, 214–253.

[23] Gordeyev, S., R. M. Rennie, A. B. Cain, and T. E. Hayden (2015), Aero-Optical Measurements of High-Mach Supersonic Boundary Layers, *AIAA Paper 2015-3246*, (June).

[24] Hinze, J. O. (1976), *Turbulence*, McGraw-Hill.

[25] Jewell, J. S., and R. L. Kimmel (2017), Boundary Layer Stability Analysis for Stetson's Mach 6 Blunt Cone Experiments." Journal of Spacecraft and Rockets, *Journal of Spacecraft and Rockets*, *54*, 258–265.

[26] Josyula, E., and W. F. Bailey (2001), Vibration Dissociation Coupling Using Master Equations in Nonequilibrium Hypersonic Blunt-Body Flow, *Journal of Thermophysics and Heat Transfer*, *15*(2).

[27] Josyula, E., and J. S. Shang (1993), Computation of Nonequilibrium Hypersonic Flowfields Around Hemisphere Cylinders, *Journal of Spacecraft and Rockets*, *7*(4), 668–679.

[28] Josyula, E., B. Gaitonde, and J. Shang (1991), Nonequilibrium Hypersonic Flow Solutions Using the Roe Flux-Difference Split Scheme, *AIAA Paper 91-1700*.

[29] Jumper, E. J., and S. Gordeyev (2017), Physics and measurement of aero-optical effects: Past and present, *Annual Review of Fluid Mechanics*, *49*(1), 419–441.

[30] Karl, S., J. M. Schramm, and K. Hannemann (2003), High Enthalpy Cylinder Flow in HEG: A Basis for CFD Validation, *AIAA Paper 2003-4252*.

[31] Kim, M. (2009), Electromagnetic Manipulation of Plasma Layer for Re-Entry Blackout Mitigation, Doctoral, University of Michigan.

[32] Landau, L., and E. Teller (1936), Zur Theorie der Schalldispersion, *Physikalische Zeitschrift der Sowjetunion*, *10*, 34–43.

[33] Linde, D. R. (1996), *Handbook of Chemistry and Physics*, CRC Press.

[34] Liou, M.-S. (1996), A sequel to ausm: Ausm+, *Journal of Computational Physics*, *129*(2), 364 – 382.

[35] Martin, A., L. Scalabrin, and I. Boyd (2012), High Performance Modeling of Atmospheric Re-entry Vehicles, Journal of Physics: Conference Series , *Journal of Physics: Conference Series*, *34*.

[36] Martin, M. P. (2003), Exploratory Studies of Turbulence / Chemistry Interaction in Hypersonic Flows 36th AIAA Thermophysics Conference Exploratory Studies of Turbulence / Chemistry Interaction in Hypersonic Flows, in *AIAA Paper 03-4055*, Orlando.

[37] Merzkirch, W. (2012), *Flow Visualization*, 2nd ed., Academic Press.

[38] Millikan, R. C., and D. R. White (1963), Systematics of Vibrational Relaxation, *39*(12), 3209–3213.

[39] Neville, A. G., I. Nompelis, K. Pramod, and G. V. Candler (2014), Effect of Thermal Non-equilibrium on Decaying Isotropic Turbulence, in *AIAA Paper 2014-3204*, June, Atlanta.

[40] Nompelis, I., T. W. Drayna, and G. W. Candler (2005), A Parallel Unstructured Implicit Solver for Hypersonic Reacting Flow Simulation, *AIAA Paper 2005-4867*.

[41] Nompelis, I., T. W. Drayna, and G. W. Candler (2014), Development of a Hybrid Unstructured Implicit Solver for the Simulation of Reacting Flows over Complex Geometries, *AIAA Paper 2014-2227*.

[42] Nonaka, S., H. Mizuno, K. Takayama, and C. Park (2000), Measurement of Shock Standoff Distance for Sphere in Ballistic Range Introduction, *Journal*, *14*(April-June 2000), 424–430.

[43] Park, C. (1990), *Nonequilibrium Hypersonic Aerothermodynamics*, John Wiley & Sons.

[44] Park, C. (2010), The Limits of Two-Temperature Model, in *AIAA Paper 2010-911*.

[45] Park, C., and S. Yoon (1992), Calculation of Real-Gas Effects on Blunt-Body Trim Angles, *AIAA Journal*, *30*(4), 999–1007.

[46] Pope, S. B. (2013), *Turbulent Flows*, Cambridge University Press.

[47] Ranjan, R., P. Vedula, K. Vogiatzis, and E. Josyula (2018), Towards Numerical Simulation of Hypersonic Turbulent Flows using High Order Methods, *AIAA Paper 2018-0980*, (January).

[48] Rybak, J. (1970), Causes, Effects and Diagnostic Measurements of the Reentry Plasma Sheath, *Tech. Rep. Defense Technical Report*, Colorado State University, Fort Collins, CO.

[49] Shu, C. (1997), Essentially Non-Oscillatory and Weighted Essentially Non-Oscillatory Schemes for Hyperbolic Conservation Laws, *Tech. Rep. 97-65*, NASA Langley.

[50] Sinha, N., A. Tejada-Martnez, C. Akan, and C. Grosch (2015), Toward a k-profile parameterization of langmuir turbulence in shallow coastal shelves, *Journal of Physical Oceanography*, *45*, 151012111836,003, doi:10.1175/JPO-D-14-0158.1.

[51] Slater, J. C., and N. H. Frank (1947), *Electromagnetism*, 1st ed., McGraw-Hill.

[52] Spalart, P., and S. Allmaras (1992), A One Equation Turbulence Model for Aerodynamic Flows, *AIAA Paper 92-0439*.

[53] Subbareddy, P., and G. Candler (2012), DNS of Transition to Turbulence in a Mach 6 Boundary Layer, in *AIAA Paper 2012-3016*.

[54] Van Driest, E. R. (1956), On turbulent flow near a wall, *Journal of Aeronautical Science*, *23*(11), 1007–1011.

[55] Vincenti, W. G., and C. H. J. Kruger (1967), *Introduction to Physical Gas Dynamics*, Wiley.

[56] Vogiatzis, K., E. Josyula, and P. Vedula (2016), Role of High Fidelity Nonequilibrium Modeling in Laminar and Turbulent Flows for High Speed ISR Missions, *AIAA Paper 2016-4317*.

[57] Weng, M., A. Mani, and S. Gordeyev (2012), Physics and Computation of Aero-Optics, *Annu. Rev. Fluid Mech.*, *44*, 299–321.

[58] Weng, M., A. Mani, and G. Stanislav (2012), Physics and Computation of Aero-Optics, *Annual Review of Fluid Mechanics*, *44*, 299–321.

[59] Wiebenga, J. E. (2014), High-Fidelity Material Response Modeling as Part of an Aerothermoelastic Framework for Hypersonic Flows, Doctoral, University of Michigan.

[60] Wilke, C. R. (1950), A Viscosity Equation for Gas Mixtures, *The Journal of Chemical Physics*, *517*(18).

[61] Wolfe, W. E., and G. J. Zissis (1993), *The Infrared Handbook*, 4th ed., IRIA Series in Infrared and Electro-Optics.

[62] Wright, M. J., G. V. Candler, , and D. Bose (1998), Data-parallel line relaxation method for the Navier-Stokes equations, *AIAA Journal*, *36*, 1603–1609.

[63] Wyckham, C. M., and A. J. Smits (2009), Aero-Optic Distortion in Transonic and Hypersonic Turbulent Boundary Layers, *AIAA*, *47*(9).

[64] Yang, H., A. Przekwas, S. Rani, and J. Dudley (2013), Direct numerical simulation validation study of a fully coupled fluid-structure interaction tool, doi: 10.2514/6.2013-95.